THE GENERALIZED OHM'S LAW IN COLLISIONLESS MAGNETIC RECONNECTION

A

THESIS

Presented to the Faculty of the University of Alaska
in Partial Fulfillment of the Requirements
for the Degree of

DOCTOR OF PHILOSOPHY

By
Heng-Jin Cai, B.S., M.S.

Fairbanks, Alaska

December 1995

THE GENERALIZED OHM'S LAW

IN COLLISIONLESS MAGNETIC RECONNECTION

By

HENG-JIN CAI

RECOMMENDED:

T. M. Jiang

J. L. Morack

D. D. Sentman

D. W. Swift

L. C. Lee, Chairman, Advisory Committee

J. L. Morack, Head, Physics Department

APPROVED:

P. B. Reichardt, Dean, College of Natural Sciences

I. R. Kan, Dean, Graduate School

Nov 27, 1995

Date

ABSTRACT

Magnetic reconnection is an important process in space environments. As a result of magnetic reconnection, the magnetic field topology changes, which requires the breakdown of the frozen-in condition in ideal magnetofluids. In a collisional plasma, the resistivity associated with Coulomb collisions of charged particles is responsible for the breakdown of frozen-in condition. In a collisionless plasma, however, the cause of the breakdown of frozen-in condition remains unanswered. We address this problem by investigating the generalized Ohm's law and the force balance near magnetic neutral lines based on two-dimensional particle simulations.

In a particle simulation with one active species, it is found that a weakly anisotropic and skewed velocity distribution is formed near the magnetic X line, leading to the presence of off-diagonal elements of plasma pressure tensor. The gradients of the off-diagonal pressure terms transport plasma momentum away from the X line to balance the reconnection electric field. The presence of the reconnection electric field results in the breakdown of frozen-in condition. The importance of both electron and ion off-diagonal pressure tensor terms in the generalized Ohm's law near neutral lines is further confirmed in full particle simulations. The generation of the off-diagonal pressure terms can be explained in terms of the thermal dispersion of particle motions and the response of particle distribution function in the electric and magnetic fields near the neutral lines.

In the particle simulations, we also find the presence of a new dynamo process, in which a large amount of new magnetic flux near the magnetic O line is generated. This dynamo process is not allowed in resistive magnetofluids. However, in a collisionless plasma, the plasma inertia and momentum transport due to the off-diagonal plasma pressure terms can lead to $\mathbf{E} \cdot \mathbf{J} < 0$ near the magnetic O line and make the dynamo process possible.

TABLE OF CONTENTS

LIST OF FIGURES

ACKNOWLEDGMENTS

I would like to thank Professor L. C. Lee, my thesis advisor, for his constant encouragement, advice, and help during my thesis study. I have been extremely fortunate to have this opportunity to study space physics under his guidance.

My sincere appreciation also goes to the other members of my graduate advisory committee, Professors T. M. Jiang, J. L. Morack, D. D. Sentman, and D. W. Swift. Their concerns and helpful suggestions improved the quality of my thesis. The particle simulation codes used in my thesis study are first written by Professor D. W. Swift and developed by Dr. D. Q. Ding. I would like to express my deep appreciation to them.

I would like to thank Professor S. -I. Akasofu for his helpful information on geomagnetic substorms and his encouragement. Special thanks are also due to Professor J. G. Roederer for his lectures on magnetospheric physics. I would like to thank Drs. J. Johnson, Y. Lin, Z. W. Ma, and A. Otto for their helpful discussions. Other fellow students at the Geophysical Institute also offered me their generous help. I am grateful to them.

It is a great pleasure to thank Professor J. W. Dungey. His interests and comments on my work are a great encouragement to me.

I am greatly indebted to my wife Ms. X. Y. Fan, whose love, support and expectation encouraged me to finish this thesis with my greatest effort.

This work was supported by grants from the Department of Energy, the National Aeronautics and Space Administration, and the National Science Foundation to the University of Alaska. The computing work was supported by the San Diego Supercomputer Center, the Arctic Region Supercomputing Center and the Pittsburgh Supercomputing center.

CHAPTER 1

Introduction

Magnetic reconnection, first proposed by Giovanelli [1947] to explain solar activities, is believed to be an important process in space environments [Dungey, 1961; Vasyliunas, 1975; Galeev, 1984; Lee, 1990] and fusion devices [Furth et al., 1963; Drake and Lee, 1977; Yamada et al., 1991]. As a result of magnetic reconnection, the magnetic field topology changes and the magnetic field energy converts into plasma kinetic energy. The change of field topology leads to the concept of open magnetosphere [Dungey, 1961], which provides a framework in the study of solar wind-magnetospheric coupling and explains the presence of polar cap and magnetotail lobes.

The change of magnetic field topology requires the breakdown of the "frozen-in" condition in ideal magnetohydrodynamics (MHD) equations. Most studies of magnetic reconnection [Sweet 1958; Parker, 1957; Petschek, 1964; Sonnerup, 1970; Yeh and Axford, 1970; Priest and Forbes, 1986; Priest and Lee, 1991; and Lee, 1995] are based on resistive MHD equations in which the resistivity is responsible for the breakdown of "frozen-in" condition. In the resistive MHD equations, the resistivity is associated with Coulomb collisions of charged particles. However, magnetic reconnection can also occur in collisionless space plasmas, in which Coulomb collisions of particles can be neglected. The breakdown of "frozen-in" condition in a collisionless plasma can be due to the inertia effect of thermal particles, which is described in the generalized Ohm's law in terms of the off-diagonal elements of plasma pressure tensor [Vasyliunas, 1975; Sonnerup, 1988; Dungey, 1988; Lyons and Pridmore-Brown, 1990; Cai et al., 1994]. The purpose of the thesis is to study the momentum transport associated with the

off-diagonal pressure terms and to examine the generalized Ohm's law in collisionless magnetic reconnection.

1.1 Breakdown of frozen-in condition in magnetic reconnection

1.1.1 The concept of "frozen-in" condition

The "frozen-in" condition states that any two fluid elements which are at one time connected by a common magnetic field line remain so thereafter. Starting from the Faraday's law

$$\frac{\partial \mathbf{B}}{\partial t} = -\nabla \times \mathbf{E}, \tag{1.1}$$

and the Ohm's law for a fluid with infinite conductivity

$$\mathbf{E} + \mathbf{v} \times \mathbf{B} = 0, \tag{1.2}$$

we have

$$\frac{\partial \mathbf{B}}{\partial t} = \nabla \times (\mathbf{v} \times \mathbf{B}). \tag{1.3}$$

where $\mathbf{B}$ is the magnetic field, $\mathbf{E}$ is the electric field, and $\mathbf{v}$ is the fluid velocity.

It can be shown from (1.3) [e.g., Siscoe, 1983] that the magnetic flux through a closed loop moving with the fluid is conserved. Mathematically, this statement can be expressed as

$$\frac{d\Phi_B}{dt} = 0, \tag{1.4}$$

where the magnetic flux through a closed loop, C, is defined as $\Phi_B \equiv \int_C \mathbf{B} \cdot d\mathbf{a}$, and $d\mathbf{a}$ is an element of area on any surface which has C as its perimeter. The total time

derivative in (1.4) is used to indicate that Φ_B is to be evaluated in reference to the loop of fluid elements, C, that move with the fluid.

Equation (1.4) indicates that we can regard the magnetic flux are frozen in the fluid. From this frozen-in condition, it is easy to see [e.g., Stern, 1966] that the elements of fluid which are connected by a magnetic field line at one time remain connected at subsequent times.

However, the frozen-in condition is violated during magnetic field line reconnection as demonstrated below.

1.1.2 The concept of magnetic reconnection

Fig. 1.1 shows the magnetic reconnection process in a localized region. Two regions with different magnetic field orientation are initially separated by a one-dimensional current sheet indicated by the dashed line as shown in Fig. 1.1a. The labels a, a', b and b' represent four fluid elements. At $t = 0$, the elements a and a' are located on side A, and the elements b and b' are located on side B. After the magnetic field line defined by fluid elements a and a' and the oppositely-directed field line defined by fluid elements b and b' approach each other and pass through the shaded area (diffusion region), as shown in Fig. 1.1b, the new reconnected field lines defined by fluid elements a and b and by fluid elements a' and b' convect away from the diffusion region. Due to the magnetic field tension force the outflow plasmas are accelerated to high speed V_{out}.

After magnetic reconnection, four different topological regions are formed. The boundaries of these four regions are called separatrices, which are shown by the heavy lines in Figure 1.1b. The intersection point of the separatrices is located at the center of

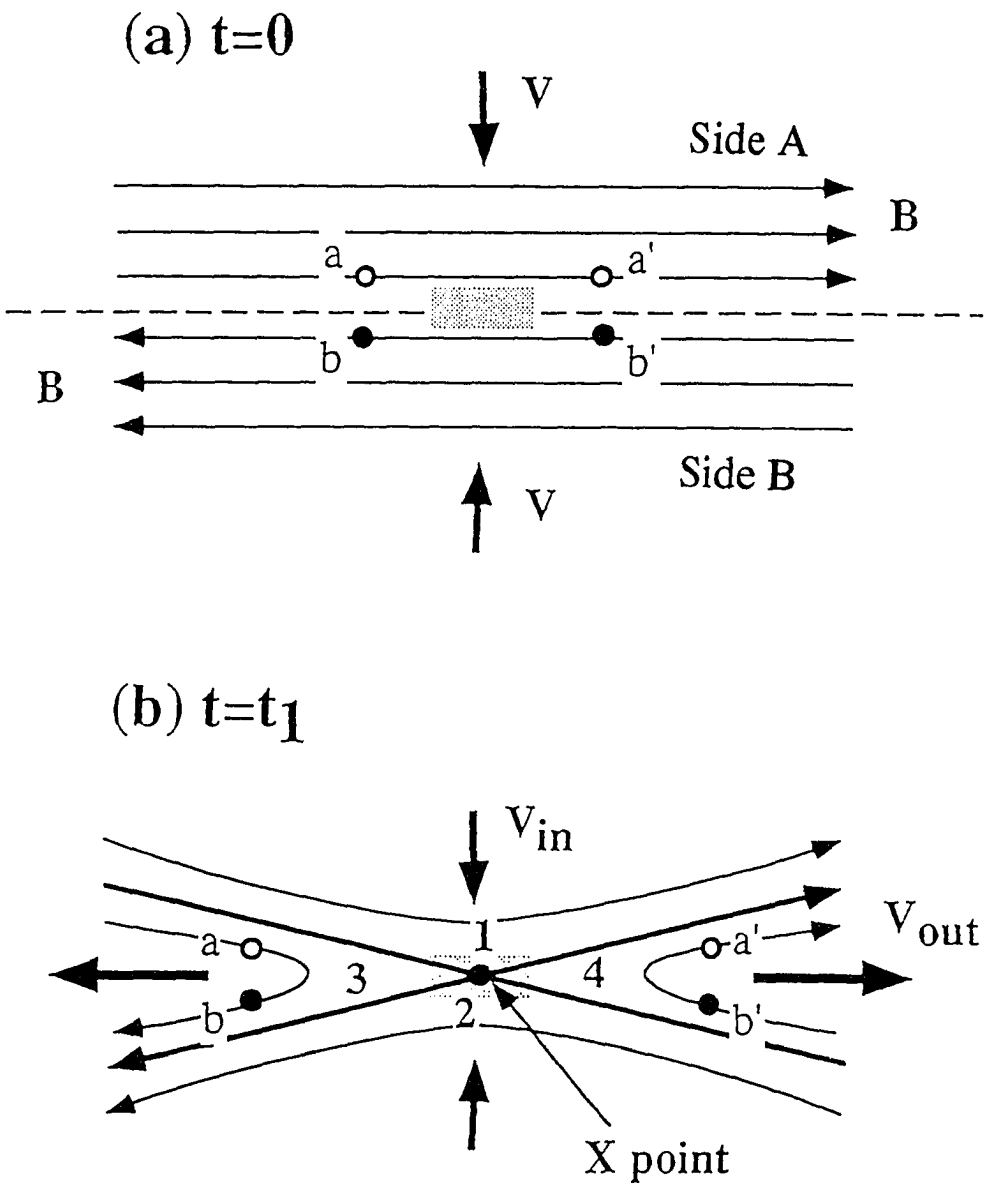

Figure 1.1 Schematic illustration of magnetic reconnection process in a current sheet. The separatrices are shown by the heavy lines.

the figure and is called X point. In three-dimensional space, the separatrices are surfaces and the intersection of the separatrix surfaces is defined as a magnetic X line.

The frozen-in condition is violated since the connections between a and a' and between b and b' are broken as a result of magnetic reconnection.

1.1.3 Breakdown of frozen-in condition in a resistive plasma

For a collisional plasma, the resistivity η is finite and the breakdown of frozen-in condition is due to binary collisions. The Ohm's law (1.2) is modified in a collisional plasma as

$$\mathbf{E} + \mathbf{v} \times \mathbf{B} = \eta \mathbf{J}, \tag{1.5}$$

where $\mathbf{J}$ is the electric current density. From Amperes law $\nabla \times \mathbf{B} = \mu_0 \mathbf{J}$, the flux transport equation is modified as

$$\frac{\partial \mathbf{B}}{\partial t} = \nabla \times (\mathbf{v} \times \mathbf{B}) + \frac{\eta}{\mu_0} \nabla^2 \mathbf{B}, \tag{1.6}$$

where μ_0 is the permeability in free space and the resistivity η is assumed constant for convenience. The first term and the second term on the right hand side of Eq.(1.6) describe the magnetic convection and magnetic diffusion, respectively. In the region outside the current sheet, the magnetic field convection is dominant, implying that magnetic field lines diffuse slowly relative to the fluid and the frozen-in condition approximately holds. However, in the shaded region as shown in Figure 1.1, the magnetic field diffusion term becomes comparable to the magnetic convection term so that the frozen-in condition is violated in this local region.

As will be shown in the next section, the plasma inertia effect described by the bulk flow inertial terms and off-diagonal pressure terms can also lead to the breakdown of frozen-in condition near magnetic neutral lines.

1.2 The generalized Ohm's law and force balance equations near neutral lines

1.2.1 The generalized Ohm's law in collisionless reconnection

In the fluid description, the generalized Ohm's law can be written as [Rossi and Olbert, 1970]

$$\mathbf{E}+\mathbf{v}\times\mathbf{B}=\eta\mathbf{J}+\frac{1}{ne}\mathbf{J}\times\mathbf{B}+\frac{m_e}{ne^2}\left[\frac{\partial\mathbf{J}}{\partial t}+\nabla\cdot(\mathbf{vJ}+\mathbf{Jv})\right]-\frac{1}{ne}\nabla\cdot\mathbf{P}^{(e)} \quad (1.7)$$

where m_e and e are the electron mass and charge, respectively; n, $\mathbf{v}$ and $\mathbf{P}^{(e)}$ are the plasma density, flow velocity and electron pressure tensor, respectively. In obtaining (1.7), terms with a factor of m_e/m_i have been neglected, where m_i is the ion mass.

In resistive MHD theory, the generalized Ohm's law is simplified as (1.5). However, the resistivity due to binary collisions is negligible ($\eta \simeq 0$) in collisionless plasmas. Therefore, in order to understand magnetic reconnection in collisionless plasmas, one has to search for dissipation mechanism other than binary collisions. An effective or anomalous resistivity may be generated near a magnetic X line in collisionless plasmas due to wave-particle interactions or nonlinear particle dynamics [e.g., Coroniti and Eviatar, 1977; Huba et al., 1980; Lee, 1982; Horton and Tajima, 1990]. An alternative approach is to include the inertial terms and off-diagonal electron pressure terms in the generalized Ohm's law.

Speiser [1970] proposed that when the characteristic system length is smaller than a collisional mean-free-path, the finite transit time of particles across the system may provide an effective collisional time, leading to an effective resistivity. Vasyliunas [1975] pointed out that during a steady state magnetic reconnection the anisotropic electron pressure terms in the generalized Ohm's law should balance the reconnection

electric field in the neighborhood of a magnetic X line. Sonnerup [1988] emphasized that ion and electron inertial effects and/or gyroviscous effects are responsible for the unfreezing of the magnetic field. Dungey [1988] proposed that a skewed velocity distribution of electrons should be developed near a magnetic X line, leading to the presence of "electron gyroviscosity" associated with off-diagonal elements of the electron pressure tensor. Dungey [1988] also pointed out that the skewed velocity distribution corresponds to the transport of y momentum when the reconnection electric field is in the y direction. The skewed distributions and force balance in the y direction proposed by Dungey [1988] were later confirmed by Lyons and Pridmore-Brown [1990, 1992] based on test particle calculations. In a recent simulation by Hesse and Winske, the electrons are treated as a fluid; the effect of the off-diagonal pressure terms is obtained by truncating the hierachy of velocity moment equations.

1.2.2 Force balance equations near neutral lines

Since the generalized Ohm's law is derived from the ion and the electron momentum equations [Rossi and Olbert, 1970], the generalized Ohm's law can be studied through a separate examination of the ion momentum equation and electron momentum equation.

The momentum equation for ions and electrons in a collisionless plasma can be written as

$$m_\alpha n_\alpha (\frac{\partial}{\partial t} + \mathbf{v}^{(\alpha)} \cdot \nabla)\mathbf{v}^{(\alpha)} + \nabla \cdot \mathbf{P}^{(\alpha)} = e_\alpha n_\alpha \left(\mathbf{E} + \mathbf{v}^{(\alpha)} \times \mathbf{B}\right), \qquad (1.8)$$

in which the number density is defined as $n_\alpha = \int f_\alpha(\mathbf{v})d\mathbf{v}$ and the bulk velocity is defined as $\mathbf{v}^{(\alpha)} = \int \mathbf{v} f_\alpha(\mathbf{v})d\mathbf{v}/n_\alpha$, where $f_\alpha(\mathbf{v})$ is the ion or electron

velocity distribution function. The plasma pressure tensor is defined as $\mathbf{P}^{(\alpha)} = m_\alpha \int (\mathbf{v} - \mathbf{v}^{(\alpha)})(\mathbf{v} - \mathbf{v}^{(\alpha)}) f_\alpha(\mathbf{v}) d\mathbf{v}$. Here α $(= i, e)$ denotes ions or electrons.

In this thesis we assume that (1) the collisionless magnetic reconnection is a two-dimensional process taking place in the x-z plane, (2) the reconnection electric field is in the y direction, and (3) all physical quantities are independent of y (i.e., $\partial/\partial y = 0$). Under these assumptions, the y component of (1.8) for electrons is

$$E_y = -\frac{m_e}{e}\left[\frac{\partial v_y^{(e)}}{\partial t} + \mathbf{v}^{(e)} \cdot \nabla v_y^{(e)}\right] - \frac{1}{n_e e}\left[\frac{\partial P_{xy}^{(e)}}{\partial x} + \frac{\partial P_{zy}^{(e)}}{\partial z}\right] - (\mathbf{v}^{(e)} \times \mathbf{B})_y \quad (1.9)$$

where the subscript y denotes the y component of a physical quantity, and $P_{xy}^{(e)}$ and $P_{zy}^{(e)}$ are the off-diagonal elements of the electron pressure tensor $\mathbf{P}^{(e)}$. During collisionless magnetic reconnection, the pressure gradient terms, $\partial P_{xy}^{(e)}/\partial x$ and $\partial P_{zy}^{(e)}/\partial z$, contribute to the force balance in the y direction near a reconnection X line [Vasyliunas, 1975; Sonnerup, 1988; Dungey, 1988; Lyons and Pridmore-Brown, 1990].

To simplify (1.9) in the neighborhood of the neutral lines (both the X and O lines), we further assume that the plasma bulk flow velocities $v_x^{(e)}$ and $v_z^{(e)}$ are relatively small at the neutral lines and the bulk flow speed $v_y^{(e)}$ is an even function of both x and z. These assumptions are found applicable to our simulations so that the convection term associated with $\mathbf{v}^{(e)} \cdot \nabla v_y^{(e)}$ can be neglected. Note that in the general case the convection term associated with $\mathbf{v}^{(e)} \cdot \nabla v_y^{(e)}$ may be important to the force balance. Because the Lorentz force is also negligible near the neutral lines, (1.9) can be simplified as

$$E_y = -\frac{m_e}{e}\frac{\partial v_y^{(e)}}{\partial t} - \frac{1}{n_e e}\frac{\partial P_{xy}^{(e)}}{\partial x} - \frac{1}{n_e e}\frac{\partial P_{zy}^{(e)}}{\partial z} \quad (1.10)$$

Similarily, the force balance equation for ions near the neutral lines can be simplified as

$$E_y = \frac{m_i}{e}\frac{\partial v_y^{(i)}}{\partial t} + \frac{1}{n_i e}\frac{\partial P_{xy}^{(i)}}{\partial x} + \frac{1}{n_i e}\frac{\partial P_{zy}^{(i)}}{\partial z} \quad (1.11)$$

The first term on the right-hand side of (1.10) or (1.11) represents the inertia

effect of the bulk flow. The second and third terms originate from the skewed velocity distribution and represent the transport of y momentum in the x and z directions, respectively.

1.2.3 The generalized Ohm's law near neutral lines

The generalized Ohm's law at neutral lines can be obtained from (1.10) and (1.11) as

$$(1+\frac{m_e}{m_i})E_y = \frac{m_e}{e^2}\frac{\partial(J_y/n)}{\partial t} - \frac{1}{ne}\left(\frac{\partial P_{xy}^{(e)}}{\partial x}+\frac{\partial P_{zy}^{(e)}}{\partial z}\right)+\frac{m_e}{m_i}\frac{1}{ne}\left(\frac{\partial P_{xy}^{(i)}}{\partial x}+\frac{\partial P_{zy}^{(i)}}{\partial z}\right) \tag{1.12}$$

where $n = n_e = n_i$ for quasi-neutrality and the current density is defined as $J_y = ne(v_y^{(i)} - v_y^{(e)})$. If the ion pressure tensor terms in (1.12) are ignored due to the small factor of m_e/m_i, equation (1.12) can also be obtained directly from (1.7).

Without the pressure tensor terms, (1.12) is reduced to $\partial(J_y/n)/\partial t = (e^2/m_e)E_y$ and J_y/n will increase to infinity in the presence of a constant inductive electric field. We will examine the importance of ion and electron off-diagonal pressure terms in (1.12) in Chapter 3.

1.3 Dungey's model

We use the coordinate system in which a magnetic X line lies along the y axis and is parallel to the current. The $x-y$ plane is the midplane of the current sheet, and the z direction is normal to the current sheet.

In a two-dimensional model, we take $\partial/\partial y = 0$. For simplicity, we consider only cases in which the guide field $B_y = 0$. The reconnection electric field is assumed to be

uniform and in the y direction, $E_y = const.$ By neglecting the electrostatic field in the $x - z$ plane, we obtain the motion equations for a particle with mass m_α and charge q_α.

$$m_\alpha \frac{dv_x}{dt} = q_\alpha v_y B_z \tag{1.12a}$$

$$m_\alpha \frac{dv_y}{dt} = q_\alpha (E_y + v_z B_x - v_x B_z) \tag{1.12b}$$

$$m_\alpha \frac{dv_z}{dt} = -q_\alpha v_y B_x \tag{1.12c}$$

Following Dungey [1988], we consider the Speiser [1965] type particle motion near the $x - y$ plane and assume $v_z \simeq 0$. The equations can be further simplified by assuming $B_z = \beta x$ with β to be a constant. Equation (1.12) becomes

$$m_\alpha \frac{dv_x}{dt} = \beta q_\alpha v_y x \tag{1.13a}$$

$$m_\alpha \frac{dv_y}{dt} = q_\alpha E_y - \beta q_\alpha v_x x \tag{1.13b}$$

Renormalize (1.13) by introducing Dungey's space scale

$$L_D = (\frac{m_\alpha E_y}{\beta^2 q_\alpha})^{\frac{1}{3}} \tag{1.14a}$$

and time scale

$$T_D = (\frac{m_\alpha^2}{\beta E_y q_\alpha^2})^{\frac{1}{3}}, \tag{1.14b}$$

we have in the dimensionless form

$$\frac{dv_x}{dt} = v_y x, \tag{1.15a}$$

$$v_y = v_{y*} + t - \frac{1}{2}x^2, \tag{1.15b}$$

where v_{y*} is the dimensionless integration constant.

According to the Liouville theorem, the particle distribution function f remains constant along a trajectory in the phase space $(\mathbf{x}, \mathbf{v})$. The distribution function f is now considered as a function of (x, v_x, v_y). The starting positions are assumed to be at small x and the initial value of f is taken to be independent of x. It is then sufficient to allow for a spread in the input values of v_x and take all trajectories to start with the initial velocity $v_{y0} = 0$, knowing that v_y will become positive due to the driving of the electric field. The assumed spatial symmetry also requires that at $x = 0$, f should be an even function of v_x. Together with the constraint that $\partial f/\partial x = 0$ for small x when $v_y = 0$, f must be an even function of v_x when $v_y = 0$.

Figure 1.2 is constructed by computing particle trajectories starting with $v_x = \pm 0.1$, $v_y = 0$ and a range of small x values (say $|x| \leq 0.1$). Each time a trajectory passes through a certain position, e.g., $x = 0.05$, the velocity components provide a point on the plot. In Figure 1.2, the two separate curves belong to positive and negative initial values of v_x: some of those electrons starting with negative v_x have turned round, while all of those starting with positive v_x still have positive v_x. Note that $f = const.$ along these two curves. The contours show a positive mean value of v_x, corresponding to a bulk flow away from the X line. The skewed distribution in Figure 1.2 corresponds to a nonzero off-diagonal pressure term P_{xy}, which can lead to the transport of y-momentum in the x direction.

Dungey's model [1988] has been further studied using numerical particle trajectory calculations by Lyons and Pridmore-Brown [1990, 1992]. In the calculations, the skewed velocity distributions in the $v_x - v_y$ space are obtained in the vicinity of an X line. The resulting momentum transport due to the off-diagonal pressure terms can indeed balance the reconnection electric field.

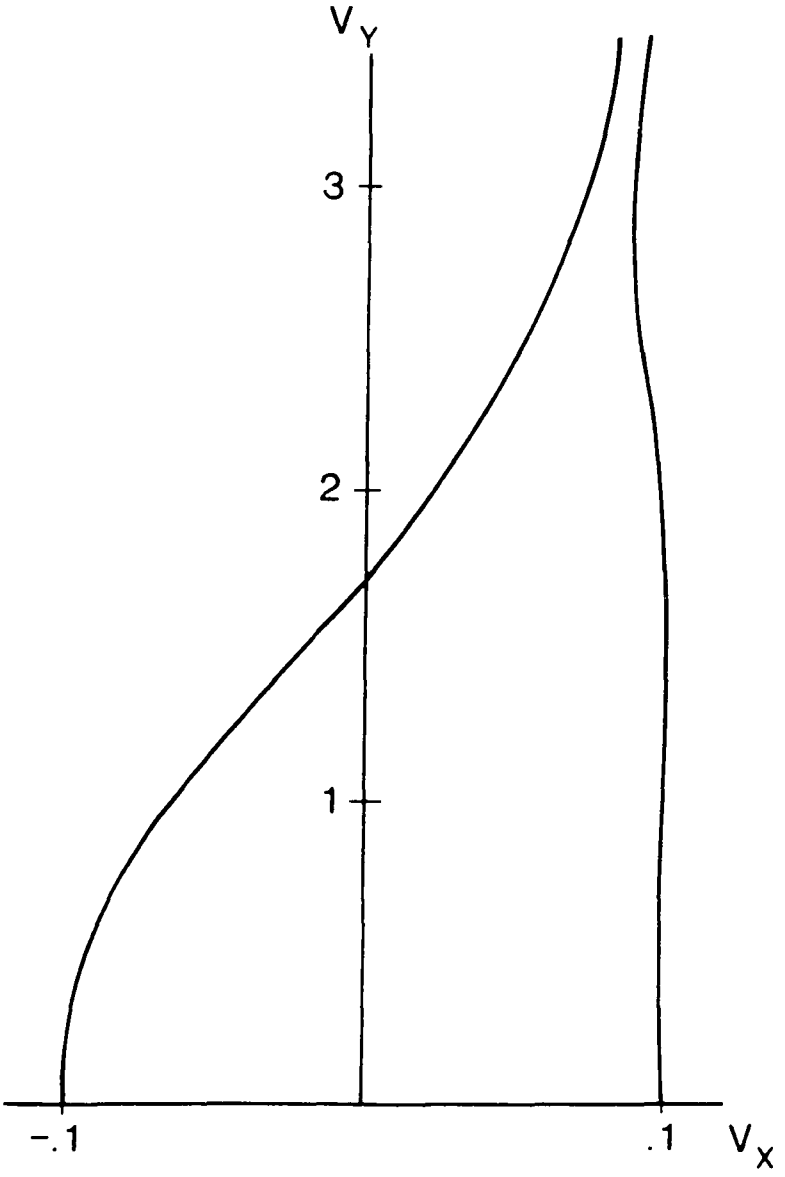

Figure 1.2 Contours of particle distribution function in the $v_x - v_y$ space at $x = 0.05$, $z = 0$. All physical quantities are normalized based on (1.14) (Dungey, 1988).

1.4 Outline of the thesis

In the test particle calculations, the reconnection electric fields and magnetic fields are not computed self-consistently from the particle motions. On the other hand, particle motions and electromagnetic fields are determined self-consistently in the particle simulations of magnetic reconnection [e.g., Terasawa, 1981; Swift, 1986; Hewett et al., 1988; Allen and Swift, 1989; Pritchett et al., 1991; Ding et al., 1992].

In this thesis we use two-dimensional particle simulations to investigate the plasma dynamics and momentum transport near neutral lines during the evolution of collisionless magnetic reconnection. The origin and spatial scale of the off-diagonal pressure terms are studied.

In Chapter 2, we present the first particle simulation study of the off-diagonal elements of plasma pressure tensor using a two-dimensional magnetoinductive particle code, in which only ions are treated as active particles while electrons are assumed to provide a charge-neutral background. It is found that a weakly skewed velocity distribution is formed near a magnetic X line, leading to the presence of off-diagonal elements of plasma pressure tensor. The gradients of off-diagonal pressure terms transport particle momentum away from the X line and make an important contribution to balance the reconnection electric field.

In Chapter 3, we extend our study on the force balance near magnetic neutral lines to full particle simulations, in which both ions and electrons are treated as particles. It is found that the off-diagonal electron pressure terms play a dominant role near a magnetic X line while the reconnection electric field plays a dominant role near an O line in the force balance for electrons. On the other hand, the deceleration or acceleration of ion bulk velocity in the direction along the X or O line results from the momentum transport

due to the off-diagonal elements of ion pressure tensor. The reconnection electric field plays an insignificant role in the force balance for ions.

In Chapter 4, an explanation for the origin of the off-diagonal pressure terms is given. We then discuss the scale length of P_{xy} based on the simulation data from Chapters 2 and 3. The off-diagonal pressure term for electrons, $P_{xy}^{(e)}$, is also calculated from the perturbed distribution function in the collisionless tearing instability.

A new dynamo process, in which magnetic flux emerges outward from an O line in the magnetic island formed by reconnection, is reported in Chapter 5. A power-law dependence of characteristic reconnection time scales on the ion-electron mass ratio is also presented in this chapter.

In the last chapter, we briefly summarize the results and suggest possible topics for future studies.

CHAPTER 2

Momentum transport near a magnetic X line in collisionless reconnection

In this chapter we use two-dimensional particle simulations to investigate plasma dynamics and momentum transport near an X line during the evolution of collisionless magnetic reconnection. It is found that the off-diagonal elements of plasma pressure tensor play an important role in the transport of the y momentum near the X line. Section 2.1 describes the two-dimensional particle simulation model, in which ions are treated as active particles and electrons are assumed to provide a charge-neutral background. Magnetic reconnection and reverse magnetic reconnection is presented in section 2.2. The momentum transport near a magnetic X line due to the off-diagonal elements of pressure tensor is discussed in section 2.3. The force balance at the X line is presented in section 2.4 and a summary is given in section 2.5.

2.1 Simulation model

The present simulation study is carried out using a two-dimensional, magnetoinductive particle code which has been described in previous papers [Ambrosiano et al., 1983; Ding et al., 1986; Lee and Ding, 1987]. In this code ions are treated as active particles while electrons are assumed to provide a charge-neutral background [Terasawa,

1981; Pritchett et al., 1991]. The field equations used in the simulations are

$$\nabla^2 \mathbf{A} = -\mu_0 \mathbf{J} \tag{2.1}$$

and

$$\mathbf{B} = \nabla \times \mathbf{A}, \tag{2.2}$$

where $\mathbf{A}$ is the vector potential. The equations for particle motion are

$$\frac{d\mathbf{p}_k}{dt} = \frac{e}{m_i} \nabla \mathbf{A} \cdot [\mathbf{p}_k - e\mathbf{A}] \tag{2.3}$$

and

$$\frac{d\mathbf{x}_k}{dt} = \frac{1}{m_i} [\mathbf{p}_k - e\mathbf{A}] = \mathbf{v}_k, \tag{2.4}$$

where $\mathbf{x}_k$, $\mathbf{v}_k$ and $\mathbf{p}_k$ are, respectively, the position, velocity, and canonical momentum of the kth particle. The current density is calculated from

$$\mathbf{J}(\mathbf{x}, t) = \sum_k e\mathbf{v}_k S[\mathbf{x} - \mathbf{x}_k(t)] \tag{2.5}$$

where $S[\mathbf{x} - \mathbf{x}_k(t)]$ is the weighting factor based on the first-order particle-in-cell bilinear interpolation method [Birdsall and Langdon, 1985]. At the position of a particle, the magnetic field is calculated by the same interpolation method. A second-order, leap-frog time-stepping algorithm is used in the simulation.

The simulation is performed in the x-z plane. We consider only the y component of the vector potential, $\mathbf{A} = A_y \mathbf{e}_y$. The reconnection electric field E_y is associated with the variation of A_y and can be calculated from $E_y = -\partial A_y / \partial t$. The initial particle number density and magnetic field profiles are given by $n(x, z, 0) = N_c sech^2(z/\lambda) + N_b$ and $\mathbf{B}(x, z, 0) = B_0 \tanh(z/\lambda)\mathbf{e}_x$, where B_0 is the magnetic field far away from the current sheet, λ is the half-thickness of the current sheet, N_b and N_c are, respectively, the

background particle number density and the current sheet particle number density. The initial particle velocity distribution is a drift-Maxwellian, with a drift speed in the y direction determined from the specified ion number density and magnetic field profiles.

The boundary conditions used in the simulation are as follows. In the x direction, periodic conditions are imposed for both particle motions and the vector potential. In the z direction, particle buffer zones are set up to handle the particles which move across the boundaries [Ding et al., 1992]. The vector potential A_y at the boundaries $z = \pm L_z$ is set to the initial constant value. Therefore the electric field E_y along these boundaries is zero. The net particle flux into and out of the boundaries is very small. We have simulated several cases with different parameters and obtained similar results. The simulation results of a typical case with $N_b/N_c = 0.25$ are presented in next sections.

The simulation is run on 128×128 grids. The grid size is $\Delta = 0.125\rho_i$, where $\rho_i = v_{thi}/\Omega_i$ is the ion gyroradius, v_{thi} is the initial thermal speed of ions, and $\Omega_i = eB_0/m_i$ is the ion gyrofrequency. We choose the half-thickness of the initial current sheet as $\lambda = 1.0\rho_i$ and set the ratio of background density to current sheet density $N_b/N_c = 0.25$. Nearly 110,000 particles are loaded in our simulation. The simulation is run from $t = 0$ to $t = 100\Omega_i^{-1}$, with a time-step of $\Delta t = 0.2\Omega_i^{-1}$.

2.2 Reconnection and reverse reconnection

Plotted in Figure 2.1 are the magnetic field lines, which are the contours of A_y, at different simulation times. We plot the magnetic field lines by fixing the increment of A_y between two neighboring contours. As mentioned in section 2, A_y at the boundaries $z = \pm 8\rho_i$ is set to the initial constant value. Notice that only the central part ($|x| \leq 8\rho_i$, $|z| \leq 4\rho_i$) of our simulation domain is presented to save space in these plots. Figure

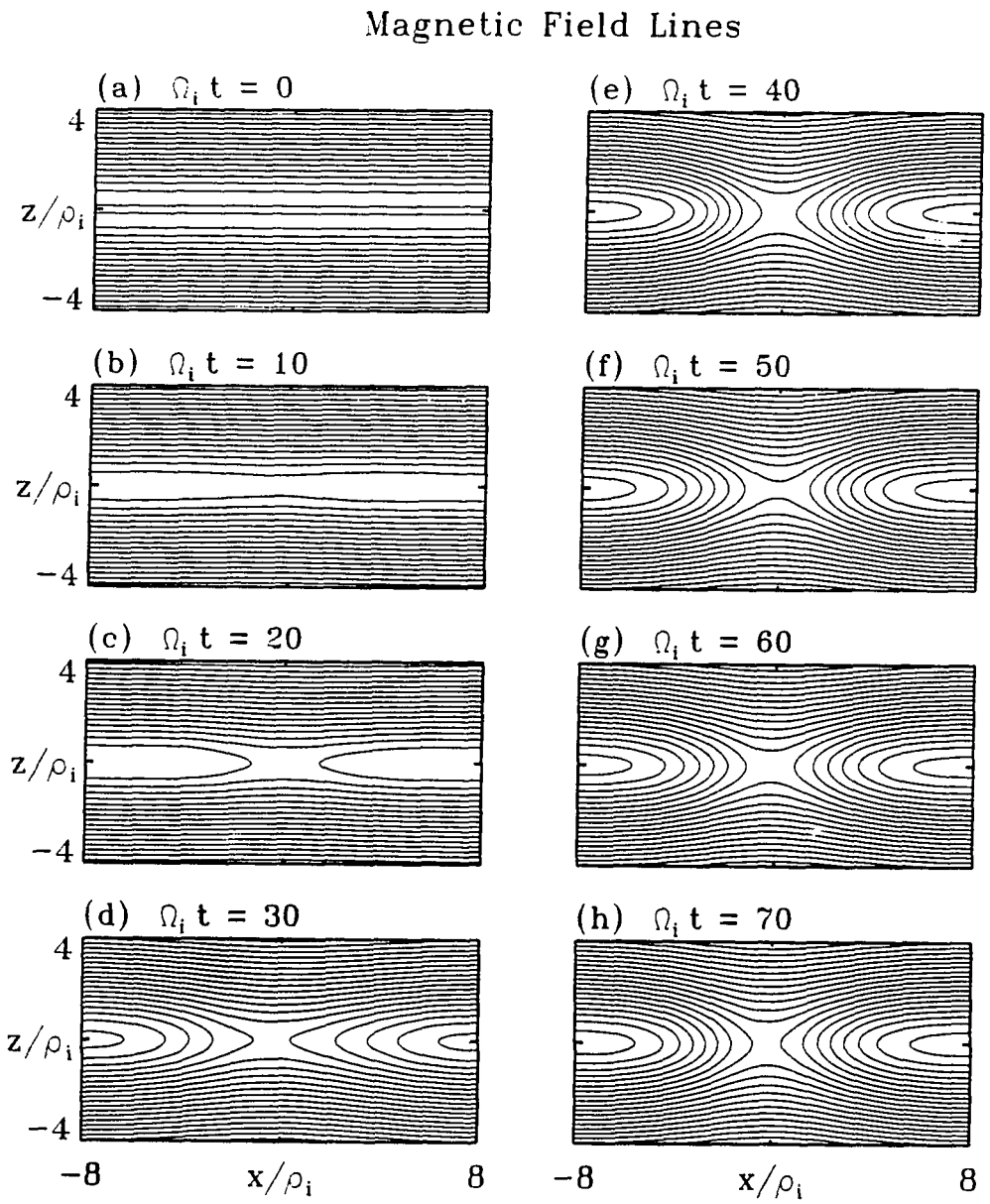

Figure 2.1 Magnetic field lines at various simulation times. A magnetic X line is present near the center of the simulation domain ($x = 0, z = 0$) in (c)-(h). Our simulation domain is $-8\rho_i \leq x \leq 8\rho_i$ and $-8\rho_i \leq z \leq 8\rho_i$. Only half of the simulation domain ($|x| \leq 8\rho_i$, $|z| \leq 4\rho_i$) is plotted.

2.1a shows the initial magnetic field configuration at $t = 0$. Figures 2.1b-2.1h show the magnetic field lines at the subsequent times. We choose the length in the x direction in such a way that only one X line is formed. We shift the X line to the center ($x = 0$, $z = 0$) by taking the advantage of the periodic boundary conditions in the x direction. Figures 2.1e, 2.1g, and 2.1h show that there are eight reconnected magnetic field lines at $t = 40\Omega_i^{-1}$, seven reconnected field lines at $t = 60\Omega_i^{-1}$, and eight reconnected field lines again at $t = 70\Omega_i^{-1}$. The number of the reconnected field lines provides a measure of the reconnected magnetic flux. The variation of the number of field lines is related to the reconnection electric field at the X line.

Figures 2.2 and 2.3 show contours of the reconnection electric field E_y and the current density J_y in the $x - z$ plane, respectively. In Figure 2.2, the electric field is normalized by $E_0 = B_0 v_{thi}$. The solid contours correspond to positive values, and the dotted lines correspond to negative values. The increment of E_y between two neighboring contour lines is 0.004 E_0. Note that the electric field is zero at the boundaries, $z = \pm 8\rho_i$, because we fixed the value of the vector potential A_y at these boundaries in our simulations. The contours in Figure 2.2 show that the electric field near the X line is positive and increases from $t = 10\Omega_i^{-1}$ to $t = 35\Omega_i^{-1}$, and it becomes negative at $t = 45\Omega_i^{-1}$ and $t = 50\Omega_i^{-1}$. At $t = 60\Omega_i^{-1}$ the electric field is positive again. In Figure 2.3, the current density is normalized by $J_0 = N_e e v_{thi} = B_0/(\mu_0 \rho_i)$. The increment of J_y between two neighboring contours is 0.1 J_0, and the value corresponding to the outermost contour line in each plot is 0.05 J_0. Note that the position of maximum particle number density is located near the center of the magnetic island ($z = 0$ and $x = \pm 8\rho_i$), while the locations of the maxima of J_y, as shown in Figure 2.3, are mainly determined by the maxima of the bulk drift velocity in the y direction. The contours in Figure 2.3 show that the current density near the X line decreases during $t = 10 - 45\Omega_i^{-1}$

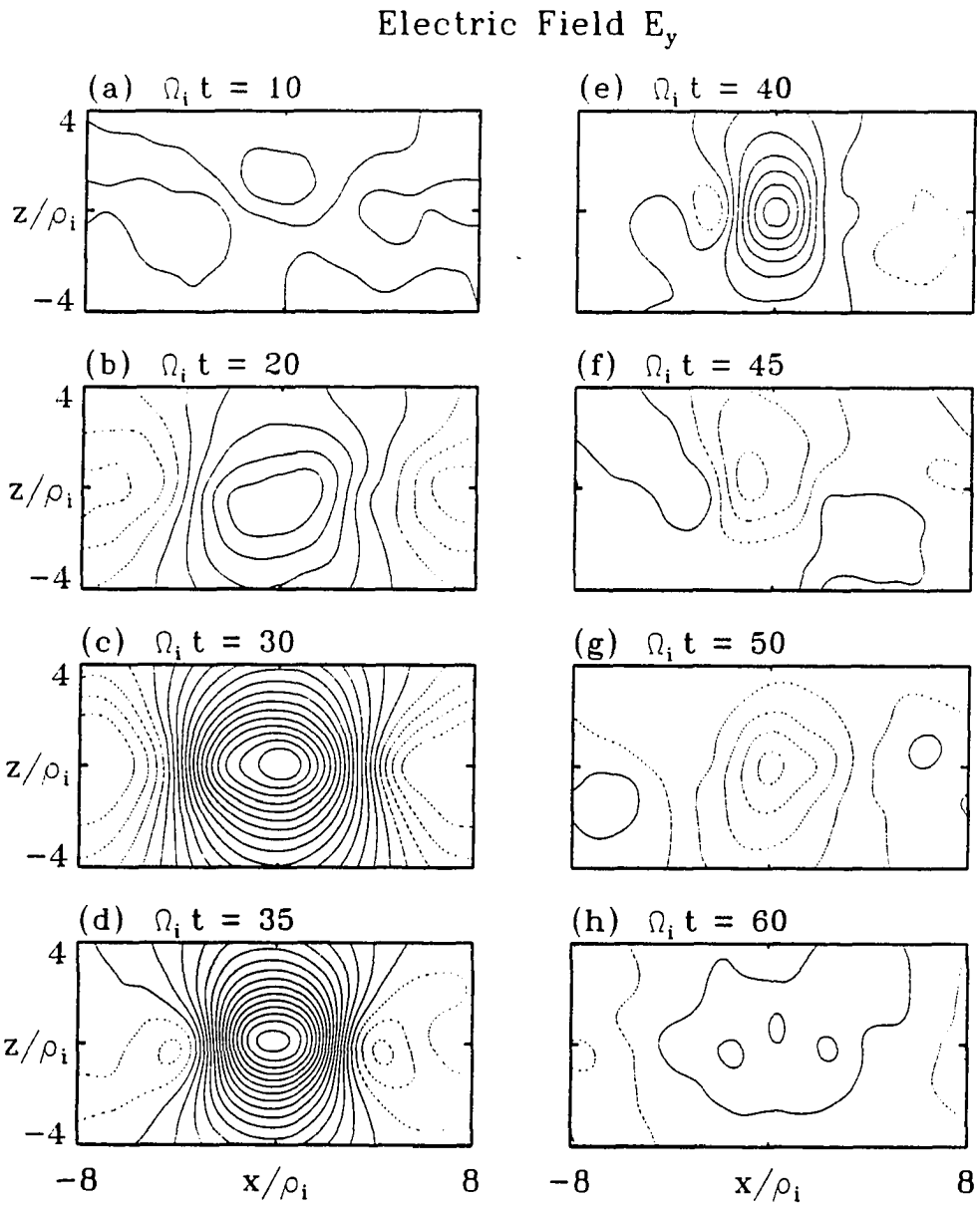

Figure 2.2 Contours of the reconnection electric field E_y in the $x - z$ plane. The electric field is normalized by $E_0 = B_0 v_{thi}$, and the increment of E_y between two neighboring contour lines is 0.004 E_0.

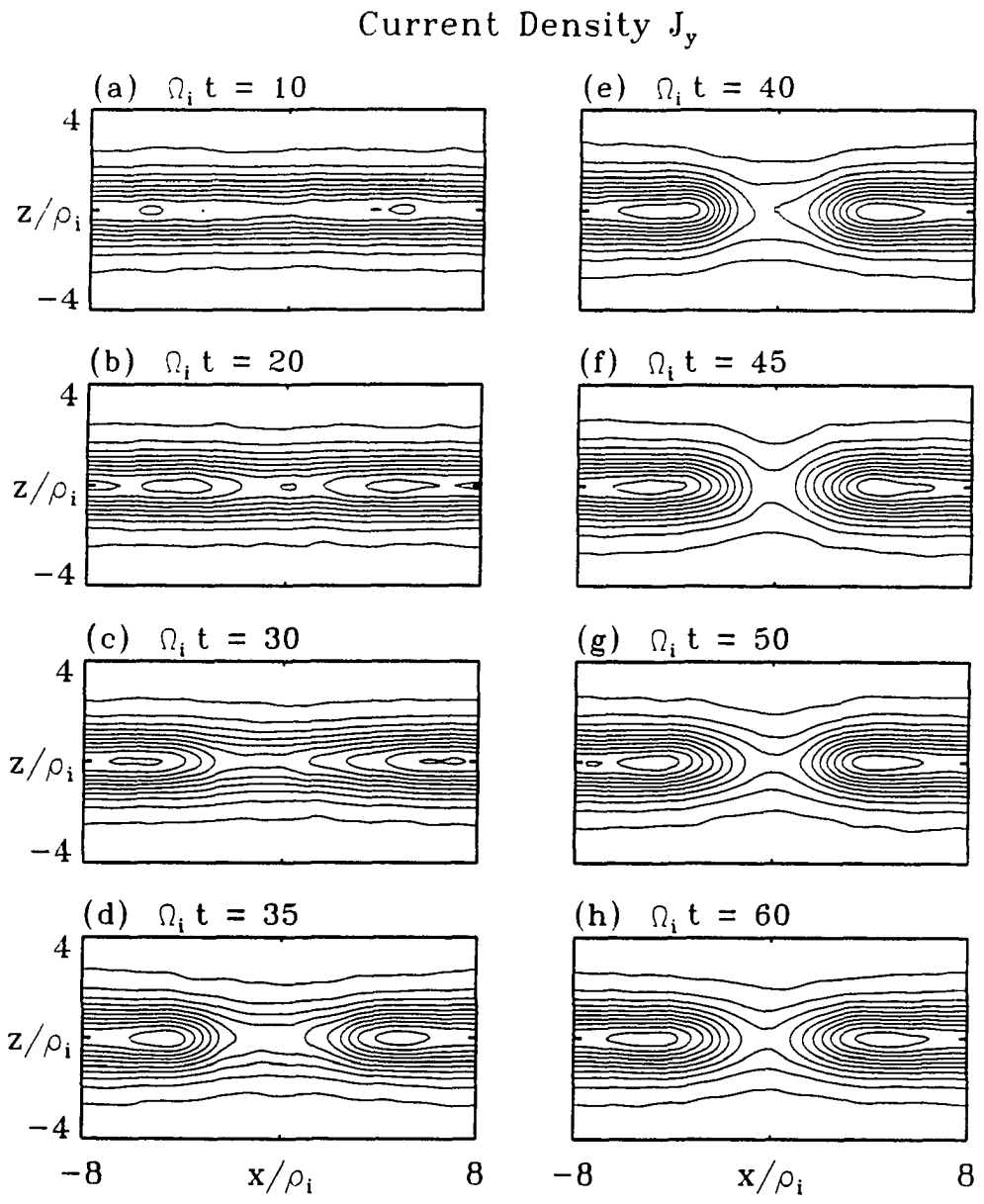

Figure 2.3 Contours of the current density J_y in the $x - z$ plane. The current density is normalized by $J_0 = N_e e v_{thi}$, and the increment of J_y between two neighboring contours is 0.1 J_0. The outermost contour lines in each plot correspond to 0.05 J_0.

and slightly increases during $t = 45 - 50\Omega_i^{-1}$. The current density in the whole domain remains positive throughout the process in our simulation.

The magnetic field energy equation can be written as

$$\frac{\partial}{\partial t}(\frac{B^2}{2\mu_0}) = -\nabla \cdot \mathbf{S} - \mathbf{E} \cdot \mathbf{J}, \tag{2.6}$$

where $\mathbf{S} = \mathbf{E} \times \mathbf{B}/\mu_0$ is the Poynting vector, and $\mathbf{E} \cdot \mathbf{J}$ denotes the energy conversion from the magnetic field to particles. Near the X line the magnetic field is very weak and the term $\partial/\partial t(B^2/2\mu_0)$ in the energy equation can be neglected. At $t = 30\Omega_i^{-1}$, $E_y > 0$, $J_y > 0$ and hence $\mathbf{E} \cdot \mathbf{J} > 0$ near the X line. The magnetic field energy is converted to particles and a normal reconnection proceeds at this moment. We also find from the simulation data that $\nabla \cdot \mathbf{S} < 0$ near the X line. In contrast, at $t = 50\Omega_i^{-1}$, $E_y < 0$, $J_y > 0$, $\mathbf{E} \cdot \mathbf{J} < 0$, and $\nabla \cdot \mathbf{S} > 0$. The energy is converted from the particles to the magnetic field.

Following Lyons et al. [1989] and Lyons and Pridmore-Brown [1992], we denote the process with $\mathbf{E} \cdot \mathbf{J} < 0$ near the X line by the term "reverse magnetic reconnection." From the time evolution of the reconnection electric field at the X line, as shown in Figure 2.9*b*, we find that the reverse reconnection process occurs at $t \simeq 43\Omega_i^{-1}$ and the normal reconnection process takes place again at $t \simeq 58\Omega_i^{-1}$. It appears that the overcompressed plasma near the O line, due to the imposed periodic boundary conditions, causes the reversal of reconnection in our simulation. A complete understanding of the reverse reconnection process is not the focus of this present work and would require a substantial amount of further investigation. However, reconnection processes with $\mathbf{E} \cdot \mathbf{J} < 0$ near X lines have been previously presented by Hewett et al. [1988], who conducted particle simulations with large ion to electron mass ratio. Observational results suggest that the

reverse reconnection may be possible in the nightside magnetosphere [de la Beaujardiere et al., 1991].

2.3 Momentum transport due to the off-diagonal pressure elements

Figure 2.4 shows the particle scatterplots in the v_x-v_y plane at $z = 0$ and $x = -2$, 0 and $2\rho_i$, respectively. The particles are sampled from $t = 29\Omega_i^{-1}$ to $t = 31\Omega_i^{-1}$ with an area of $5\Delta \times 5\Delta$ in the $x - z$ plane. The constant f contours are also shown in the scatter plots. Figures 2.4*a* and 2.4*c* indicate that the velocity distributions of particles are weakly skewed. However, these weakly skewed distributions can generate the off-diagonal elements of the pressure tensor with a gradient large enough to balance the reconnection electric field as discussed below.

Because the velocity distributions are only weakly skewed in our simulation, the off-diagonal terms of the pressure tensor is very small compared with the diagonal terms. One should be very careful in extracting the off-diagonal terms under the condition of limited number of simulation particles. In our simulation, the zeroth-order, the first-order and the second-order moments of velocity distribution are evaluated from particles sampled in five time steps on each grid. We then obtain the plasma density n, momentum density $nm_i\mathbf{v}$, and kinetic pressure tensor $\mathbf{K}$ by averaging these quantities both in space and in time. The thermal pressure tensor $\mathbf{P}$ is calculated from the equation $\mathbf{P} = \mathbf{K} - nm_i\mathbf{vv}$. This evaluation procedure implies that we calculate, for example, the nonlinear term $v_z(\partial v_y/\partial z)$ by $<v_z>(\partial<v_y>/\partial z)$ rather than $<v_z(\partial v_y/\partial z)>$, where $<...>$ denotes the averages, which ensures the term $v_z(\partial v_y/\partial z)$ to be zero at an X line as expected theoretically.

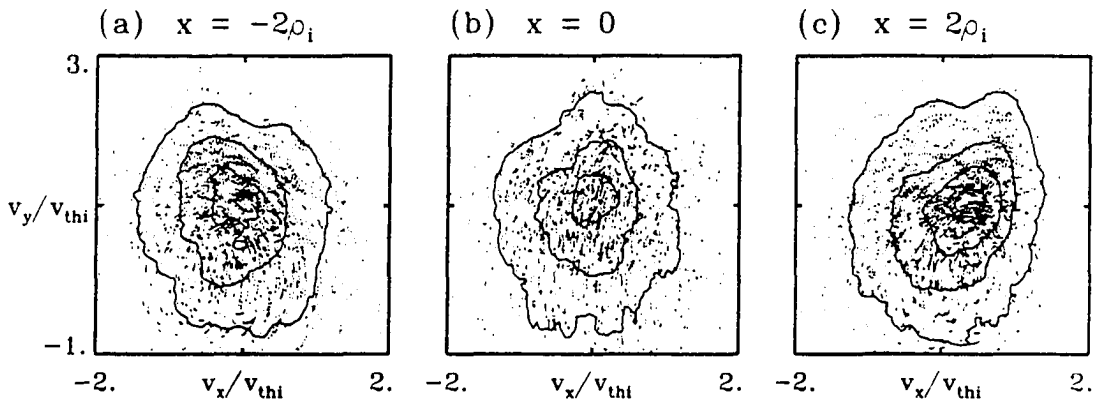

Figure 2.4 Particle scatterplots in the v_x-v_y plane at $z = 0$ and (a) $x = -2\rho_i$, (b) $x = 0$ and (c) $x = 2\rho_i$. The particles are sampled from $t = 29\Omega_i^{-1}$ to $t = 31\Omega_i^{-1}$ with an area of $5\Delta \times 5\Delta$ in the $x - z$ plane. The contour lines of constant f are also shown.

Figures 2.5 and 2.6 show the evolution of the off-diagonal elements of pressure tensor, P_{xy} and P_{zy}, in the $x - z$ plane. The pressure tensor terms are normalized by $P_0 = B_0^2/2\mu_0$. The solid lines correspond to positive values, and the dotted lines correspond to negative values. The increment between neighboring contours is $0.01P_0$. It is shown in Figure 2.5 that a clear pattern of P_{xy} emerges from $t = 20\Omega_i^{-1}$ to $t = 30\Omega_i^{-1}$ and the pattern becomes complicated after $t = 30\Omega_i^{-1}$. P_{zy} is much weaker than P_{xy}. However, coherent patterns of P_{zy} near the X line can still be seen in Figures 2.6*c* and 2.6*d*.

In order to study the contribution of the off-diagonal pressure elements to the momentum transport near the X line, we plot the profiles of the pressure tensor elements at $t = 30\Omega_i^{-1}$ and $t = 50\Omega_i^{-1}$ in Figure 2.7. Profiles of $P_{xy}(x, z = 0)$, the distribution of P_{xy} along x axis, are shown on the left column, while profiles of $P_{zy}(x = 0, z)$, the distribution of P_{zy} along z axis, are on the right column. Notice the different scales for $P_{xy}(x, z = 0)$ and $P_{zy}(x = 0, z)$. The off-diagonal elements of the pressure tensor, which are also normalized by $P_0 = B_0^2/2\mu_0 = N_c m_i v_{thi}^2$, are usually less than 0.1 as shown in Figure 2.7. For comparison, the initial diagonal elements of the pressure tensor in the central current sheet are $(1 + N_b/N_c)P_0 = 1.25P_0$. These results also indicate that the plasma velocity distributions are only weakly skewed.

As shown in Figures 2.7*a* and 2.7*b*, in the neighborhood of the X line ($x = 0, z = 0$), $P_{xy}(x, z = 0)$ is an odd function of x and $P_{zy}(x = 0, z)$ is an odd function of z. This asymmetric feature bears resemblance to the profile of P_{xy} by Vasyliunas [1975, Figure 5]. The profiles of $P_{xy}(x, z = 0)$ and $P_{zy}(x = 0, z)$ at $t = 30\Omega_i^{-1}$ show that during the periods of normal reconnection the gradients of the off-diagonal elements of the plasma pressure tensor at the X line are positive, indicating that the y momentum of the plasma is transferred from the region near the X line to regions outside the X line. Figures

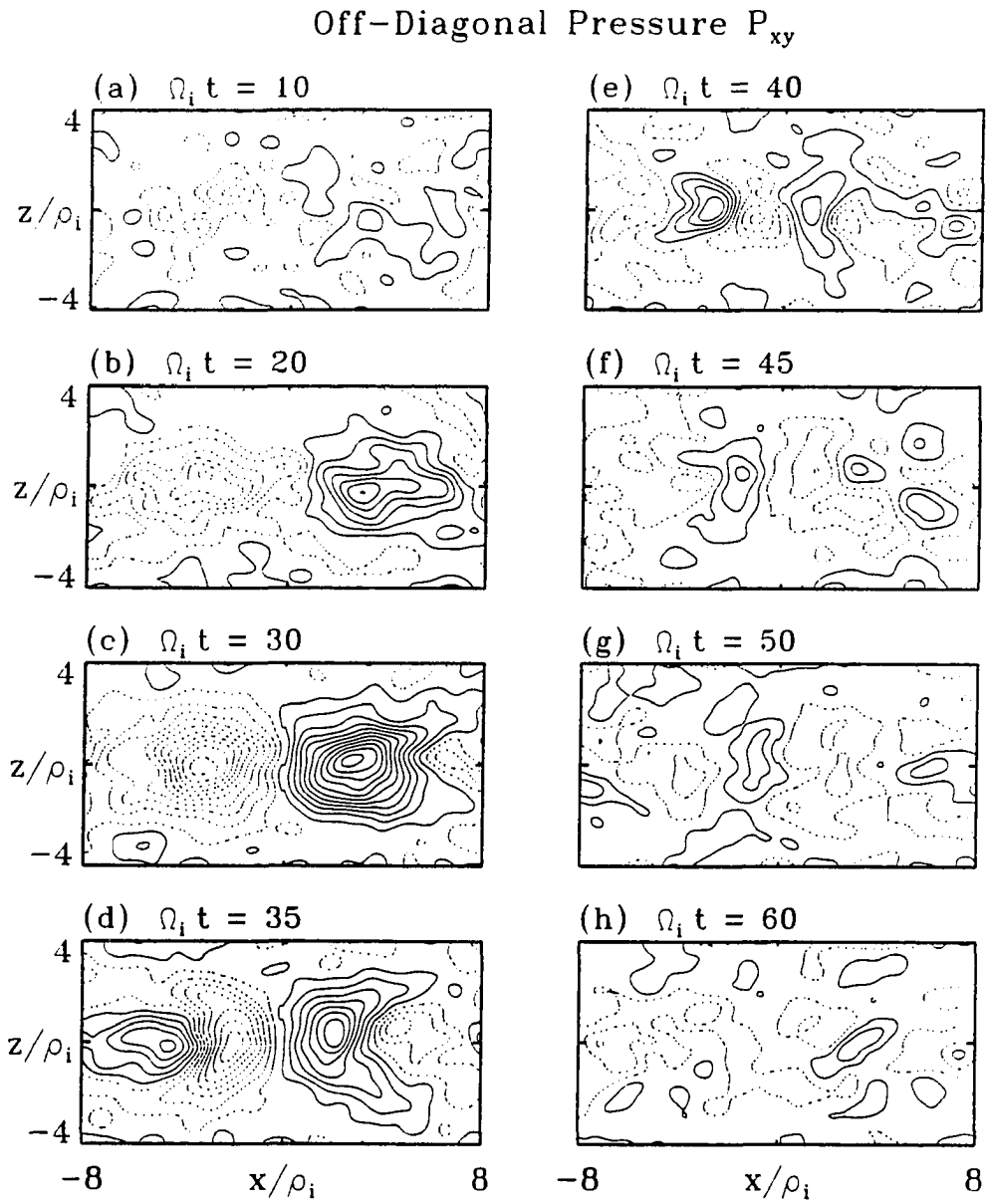

Figure 2.5 The contour lines of P_{xy} are plotted in the $x - z$ plane at various times. The increment between neighboring contours is $0.01P_0$, where $P_0 = B_0^2/2\mu_0$.

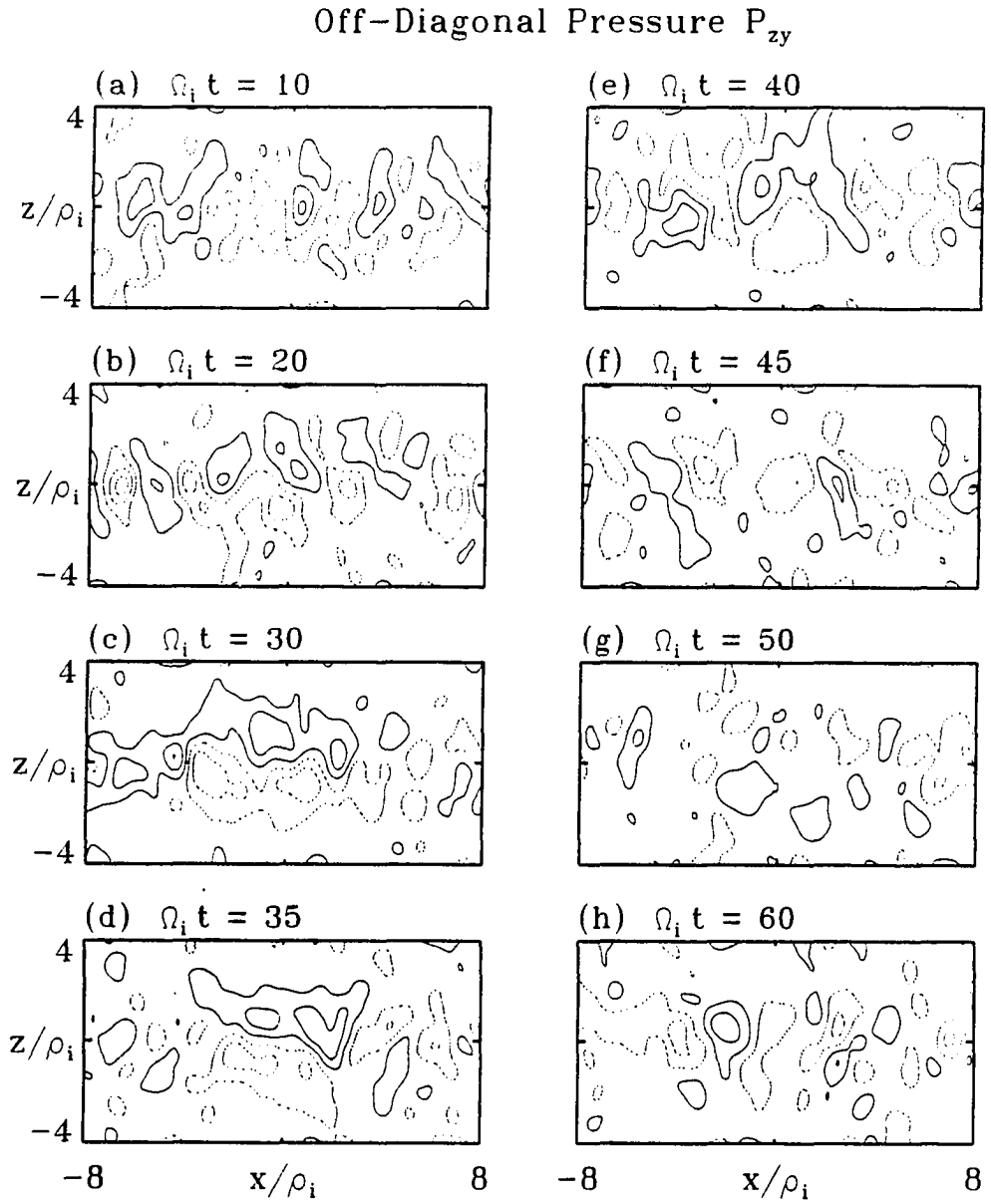

Figure 2.6 Same as Figure 2.5 except for P_{zy}.

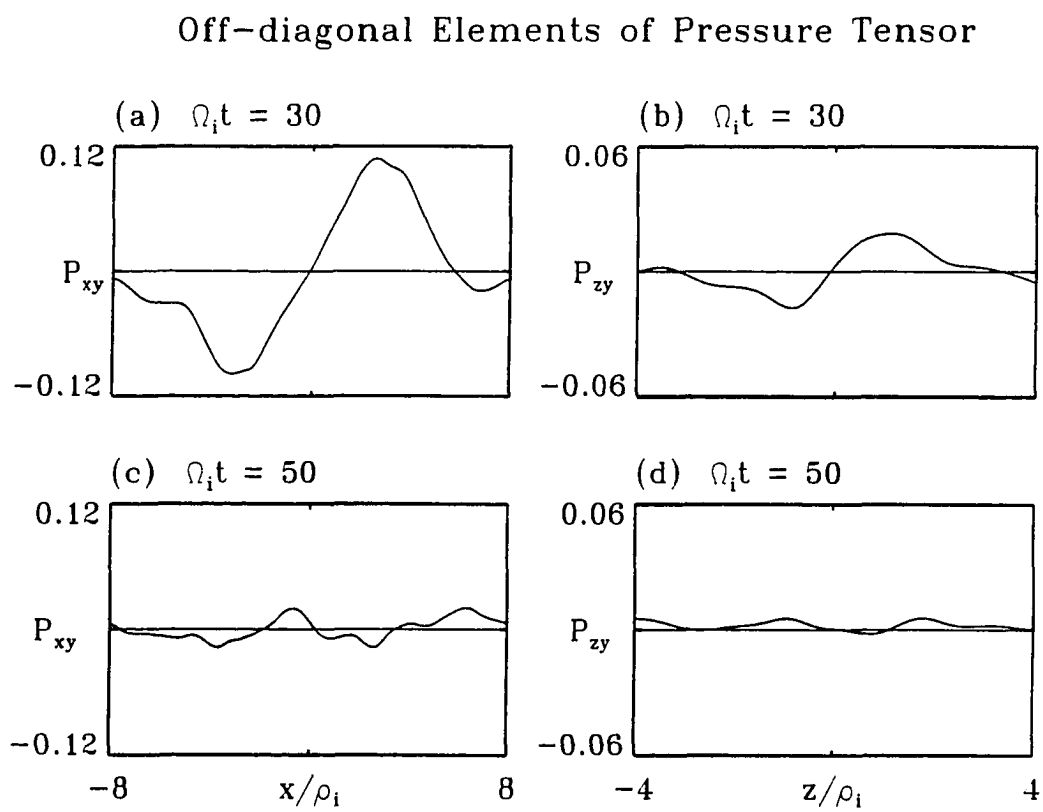

Figure 2.7 Profiles of the off-diagonal elements of the plasma pressure tensor, $P_{xy}(x, z = 0)$ and $P_{zy}(x = 0, z)$, at $t = 30\Omega_i^{-1}$ and $t = 50\Omega_i^{-1}$. The pressure tensor is normalized by $P_0 = B_0^2/2\mu_0$.

2.7*c* and 2.7*d* show that during the reverse reconnection the sum of the gradients of the off-diagonal pressure terms are negative, which indicates that the y momentum is transferred into the X line (also see the later discussion associated with Figure 2.9).

To obtain a visualized picture of the y momentum transport in the x-z plane, schematic diagrams for the y momentum flux during the normal magnetic reconnection ($E_y > 0$) period, $t < 43\Omega_i^{-1}$, are shown in Figure 2.8. Figure 2.8*a* is a schematic diagram for the y momentum flux in the x-z plane associated with the off-diagonal elements of the plasma pressure tensor, P_{xy} and P_{zy}, in the neighborhood of the X line. The divergence of the flux near the X line is positive, which indicates a net transport of the y momentum. For comparison, the transport of y momentum in the x-z plane associated with the plasma bulk motion, $nm_iv_xv_y$ and $nm_iv_zv_y$, near the X line is plotted in Figure 2.8*b*. As mentioned in section 3, the transport of the y momentum associated with the plasma bulk motion, $\nabla \cdot (nm_iv_y\mathbf{v})$, near the X line can be reduced to $-m_iv_y\partial n/\partial t$. Therefore there is no net transport of the y momentum due to the plasma bulk motion in the steady state reconnection.

2.4 Force balance at the X line

We plot in Figure 2.9 the time-evolution of each term at the X line ($x = 0, z = 0$) in the force balance equation (1.11), which is rewritten in currently used notations as

$$E_y = \frac{m_i}{e}\frac{\partial v_y}{\partial t} + \frac{1}{ne}\frac{\partial P_{xy}}{\partial x} + \frac{1}{ne}\frac{\partial P_{zy}}{\partial z} \qquad (2.7)$$

All terms in (2.7) are normalized by $E_0 = B_0v_{thi}$. In Figure 2.9*a*, the dotted line corresponds to the y momentum transport in the x direction, $(1/ne)\partial P_{xy}/\partial x$, the dashed line corresponds to the y momentum transport in the z direction, $(1/ne)\partial P_{zy}/\partial z$,

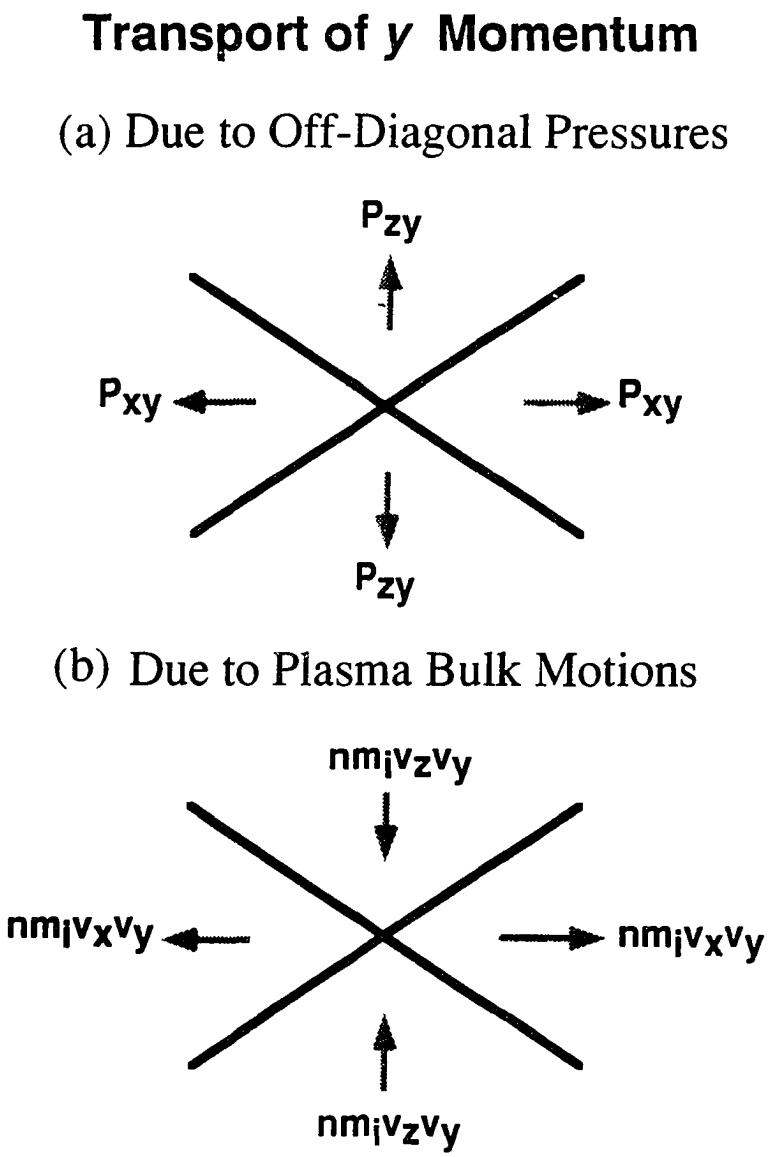

Figure 2.8 A schematic diagram for the transport of the y momentum near the X line in the $x-z$ plane during collisionless magnetic reconnection : (a) the transport due to the off-diagonal elements of the plasma pressure tensor, P_{xy} and P_{zy}, and (b) the transport due to the plasma bulk motion, $nm_iv_xv_y$ and $nm_iv_zv_y$.

and the solid line is the inertial term, $(m_i/e)\partial v_y/\partial t$. The solid line in Figure 2.9*b* shows the sum of the above three terms, which is the right-hand side of (2.7), whereas the dashed line in Figure 2.9*b* shows the evolution of the reconnection electric field E_y. It can be clearly seen that the reconnection electric field is approximately balanced by the sum of the three terms in Figure 2.9*a*.

Figure 2.9*b* also shows that the evolution of the reconnection electric field undergoes a transition from positive to negative at $t \simeq 43\Omega_i^{-1}$ and another transition from negative to positive at $t \simeq 58\Omega_i^{-1}$. As shown in Figure 2.9*a*, similar transitions also occur for the momentum transport terms, $(1/ne)\partial P_{xy}/\partial x$ and $(1/ne)\partial P_{zy}/\partial z$. As mentioned earlier, the current density near the X line, J_y, is positive throughout the simulation. Therefore, before $t \simeq 43\Omega_i^{-1}$, $\mathbf{E} \cdot \mathbf{J} > 0$ and the magnetic energy is converted into the plasma kinetic energy near the X line by magnetic reconnection. During the reverse reconnection between $t \simeq 43\Omega_i^{-1}$ and $t \simeq 58\Omega_i^{-1}$, $\mathbf{E} \cdot \mathbf{J} < 0$ and the plasma kinetic energy is converted back into magnetic energy near the X line. The transitions from the normal magnetic reconnection ($E_y > 0$) to the reverse reconnection ($E_y < 0$) and then from the reverse reconnection to the normal reconnection shown in Figure 2.9*b* are consistent with the magnetic field line patterns plotted in Figures 2.1*e*-2.1*h*. For $t > 80\Omega_i^{-1}$, E_y still oscillates but with a damped amplitude. It is expected that E_y would approach 0 as $t \rightarrow \infty$.

Notice that the inertial term, $m_i\partial v_y/\partial t$, varies approximately out of the phase with the momentum transport terms after $t \simeq 33\Omega_i^{-1}$ as shown in Figure 2.9*a*. In addition, the acceleration of the bulk velocity (v_y) at the X line can be out of phase with the reconnection electric field E_y in some periods of time. For example, the velocity v_y decreases during $t \simeq 33 - 43\Omega_i^{-1}$ ($\partial v_y/\partial t < 0$ as shown in Figure 2.9*a*) when E_y is still positive, and v_y increases during $t \simeq 45 - 51\Omega_i^{-1}$ when the electric field is

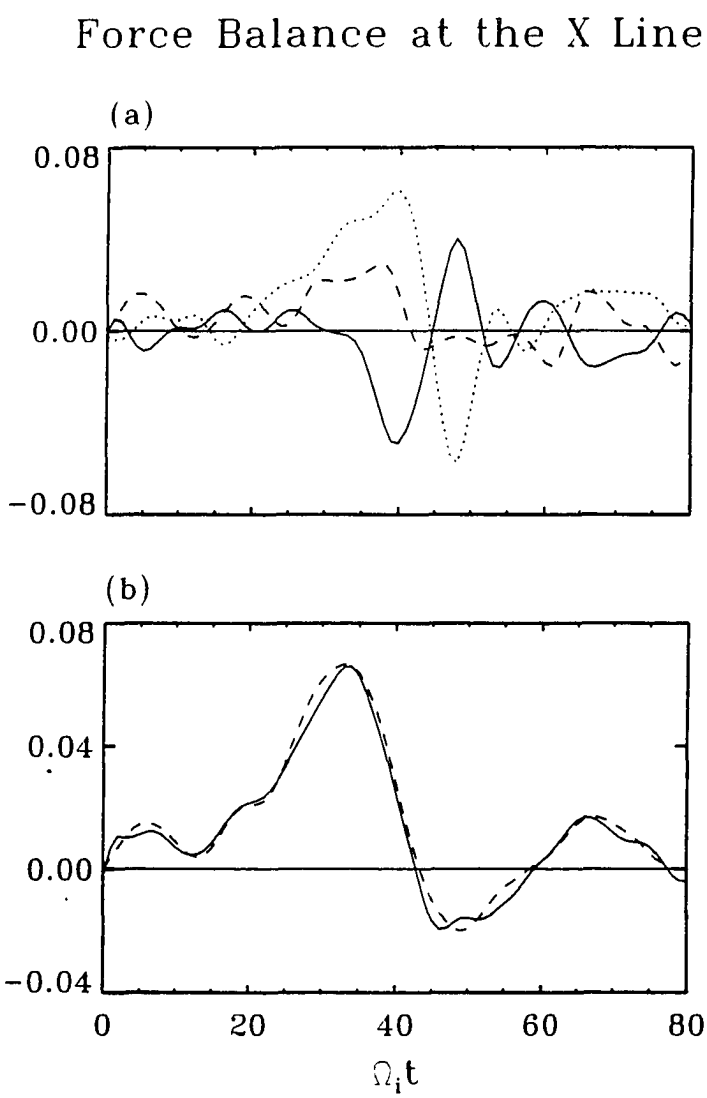

Figure 2.9 (a) Time evolution of the three terms during reconnection: the term $(1/ne)\partial P_{xy}/\partial x$ is drawn with the dotted line, $(1/ne)\partial P_{zy}/\partial z$ with dashed line, and $(m_i/e)\partial v_y/\partial t$ with solid line. (b) Time history of the force balance at the X line: The sum of the three terms in Figure 2.9a is plotted with solid line, and the reconnection electric field E_y is plotted with dashed line. All these terms are normalized by $E_0 = B_0 v_{thi}$.

negative. Therefore the momentum transport due to the off-diagonal elements of the pressure tensor can sometimes give rise to a greater force than the reconnection electric field and dominate the dynamics along the X line.

2.5 Summary

We have investigated the momentum transport near a magnetic X line during time-dependent collisionless reconnection. It is found that the momentum transport associated with the off-diagonal elements of plasma pressure tensor plays a dominant role in the force balance near the X line. The main results of our simulation study are the following:

(1) A weakly skewed velocity distribution is formed near the magnetic X line, resulting in the presence of off-diagonal elements of plasma pressure tensor, P_{xy} and P_{zy}.

(2) During the normal magnetic reconnection, the gradients of the off-diagonal pressure tensor terms, $\partial P_{xy}/\partial x$ and $\partial P_{zy}/\partial z$, lead to a transfer of y momentum from the region near the X line to regions outside the X line.

(3) During the reverse magnetic reconnection with $\mathbf{E} \cdot \mathbf{J} < 0$ near the X line, the momentum transport associated with the off-diagonal pressure terms can transfer the y momentum into the X line.

(4) The momentum transport due to the off-diagonal pressures can sometimes provide a greater force than the reconnection electric field and dominate the dynamics near the X line.

(5) The inertial term, $nm_i\partial v_y/\partial t$, also plays a significant role in the force balance near the X line.

CHAPTER 3

Force balance at neutral lines in a full particle simulation

In this chapter, we extend our study on momentum transport near magnetic neutral lines to full particle simulations, in which both ions and electrons are treated as particles. The full particle simulation model is briefly described in Section 1. Magnetic reconnection and the accompanying electrostatic field are presented in Section 2. Force balance at neutral lines for electrons and for ions is discussed in Section 3 and Section 4, respectively. A summary is given in Section 5.

3.1 Simulation model

The present simulation study employs a two-dimensional, magnetoinductive particle code [Swift, 1986; Ding et al., 1992], in which particle motion is advanced by a second-order, leap-frog algorithm based on the following equations

$$\frac{d\mathbf{p}_{\alpha k}}{dt} = \frac{q_\alpha}{m_\alpha}(\nabla \mathbf{A}) \cdot (\mathbf{p}_{\alpha k} - q_\alpha \mathbf{A}) - q_\alpha \nabla \phi, \tag{3.1}$$

$$\frac{d\mathbf{x}_{\alpha k}}{dt} = \frac{1}{m_\alpha}(\mathbf{p}_{\alpha k} - q_\alpha \mathbf{A}) \tag{3.2}$$

where α $(= i, e)$ denotes ions or electrons, m_α and q_α are the mass and electric charge for ions or electrons, and $\mathbf{x}_{\alpha k}$ and $\mathbf{p}_{\alpha k}$ are, respectively, the position and canonical momentum of k-th particle of species α. The electrostatic potential ϕ is obtained by

solving the Poisson equation

$$\nabla^2\phi = -\alpha_e\rho \tag{3.3}$$

and the vector potential $\mathbf{A}$ is solved together with χ, the time derivative of ϕ ($\chi = \partial\phi/\partial t$), by iteration based on the following equations

$$\nabla^2\mathbf{A} = -\alpha_m\mathbf{J} + \frac{\alpha_m}{\alpha_e}\nabla\chi, \tag{3.4}$$

$$\nabla^2\chi = \alpha_e\nabla\cdot\mathbf{J}, \tag{3.5}$$

where α_e and α_m are electric and magnetic coupling constants, respectively, which can be chosen artificially in particle simulations.

The charge density ρ and current density $\mathbf{J}$ are calculated from the following equations.

$$\rho = \sum_\alpha q_\alpha n_\alpha \tag{3.6}$$

and

$$\mathbf{J} = \sum_\alpha \frac{q_\alpha}{m_\alpha}\mathbf{W}_\alpha - (\sum_\alpha \frac{q_\alpha^2 n_\alpha}{m_\alpha})\mathbf{A}. \tag{3.7}$$

The moments are evaluated from

$$n_\alpha = \sum_k S\left[\mathbf{x} - \mathbf{x}_{\alpha k}(t)\right] \tag{3.8}$$

and

$$\mathbf{W}_\alpha = \sum_k \mathbf{p}_{\alpha k} S\left[\mathbf{x} - \mathbf{x}_{\alpha k}(t)\right], \tag{3.9}$$

where $S\left[\mathbf{x} - \mathbf{x}_{\alpha k}(t)\right]$ is the first order particle-in-cell bilinear weighting factor. Note that in the above formulation the Coulomb gauge, $\nabla\cdot\mathbf{A} = 0$, is used. The electromagnetic fields can be obtained from $\mathbf{E} = -\nabla o - \partial\mathbf{A}/\partial t$ and $\mathbf{B} = \nabla\times\mathbf{A}$.

The simulation is performed in the x-z plane. The initial particle (both ion and electron) number density and magnetic field profiles are given by $n(x, z, t = 0) = N_c sech^2(z/a) + N_b$ and $\mathbf{B}(x, z, t = 0) = B_0 \tanh(z/a)\mathbf{e}_x$, where B_0 is the magnetic field far away from the current sheet, a is the half-thickness of the current sheet, and N_b and N_c are, respectively, the background particle number density and the current sheet particle density. The initial particle velocity distribution is a drift-Maxwellian, with a drift speed in the y direction determined from the initial local particle number density and current density associated with the initial magnetic field.

The boundary conditions used in the simulation are described as follows. The simulation length in the x direction is L_x and periodic conditions are imposed for both particle motions and electromagnetic fields at $x = \pm L_x/2$. In the z direction, particle buffer zones are set up to handle the particles which move across the boundaries [Ding et al., 1992]. The electrostatic potential ϕ and the vector potential A_x at the boundaries $z = \pm L_z/2$ are fixed, while the Coloumb gauge condition $\nabla \cdot \mathbf{A} = 0$ requires that $\partial A_z/\partial z = 0$ at $z = \pm L_z/2$. The vector potential A_y at the boundaries $z = \pm L_z/2$ is set to the initial constant value. Therefore the inductive electric field E_y, which is calculated from $E_y = -\partial A_y/\partial t$, along these boundaries is zero. The net particle flux into or out of the boundaries is very small.

We run a case with an ion-electron mass ratio of $m_i/m_e = 1836$. The ion-electron temperature ratio is set to $T_i/T_e = 0.2$. The simulation is run on 64×64 grids. The simulation lengths are $L_x = 8\rho_e$ and $L_z = 8\rho_e$, and the grid size is $\Delta = 0.125\rho_e$. Here $\rho_e = v_{the}/\Omega_e$ is the electron gyroradius, v_{the} is the thermal speed of electrons, and $\Omega_e = eB_0/m_e$ is the electron gyrofrequency. Note that ions are unmagnetized in the whole simulation domain because the ion gyroradius, $\rho_i \simeq 20\rho_e$, is larger than the simulation lengths.

We choose the half-thickness of the initial current sheet as $a = 0.25\rho_e$ and set the density ratio as $N_b/N_c = 0.1$. The length in the x direction has been chosen such that the most unstable tearing mode has a wavelength $\lambda \sim L_x$. Nearly 50,000 particles for each species are loaded in our simulation. The time-step is $\Delta t = 0.1\Omega_e^{-1}$. Simulation results from $t = 0$ to $t = 120\Omega_e^{-1}$ are presented below.

3.2 Magnetic reconnection and the electrostatic field

Plotted in Figure 3.1 are the magnetic field lines, which are the contours of constant A_y, at different simulation times. Only the central portion ($|z| \leq 2\rho_e$) of our simulation domain is presented to save space in these plots. During the simulation, a magnetic island is formed with the presence of a reconnection X line at $x \simeq -0.9\rho_e$, $z = 0$ and an O line at $x \simeq 3.1\rho_e$, $z = 0$. We plot the magnetic field lines by fixing the increment of A_y between two neighboring contours. The solid lines in these plots denote the newly generated magnetic flux, which will be studied in detail in Chapter 5.

We plot in Figure 3.2 contours of the reconnection electric field, $E_y = -\partial A_y/\partial t$, in the $x - z$ plane at different times. The solid contours denote positive values and the dotted contours denote negative values. The increment of E_y between two neighboring contours is $0.0025E_0$, where $E_0 = B_0 v_{the}$. Because the current density (not shown) is positive in the y direction, the negative reconnection electric field near the O line indicates that there exists a dynamo process in which $\mathbf{E} \cdot \mathbf{J} < 0$. The time history of E_y at the X line and at the O line will be presented later.

Figure 3.3 shows contours of the electrostatic potential Φ in the $x - z$ plane at different times. The solid lines correspond to positive values, and the dotted lines correspond to negative values. Note that we set the electric potential to be zero at

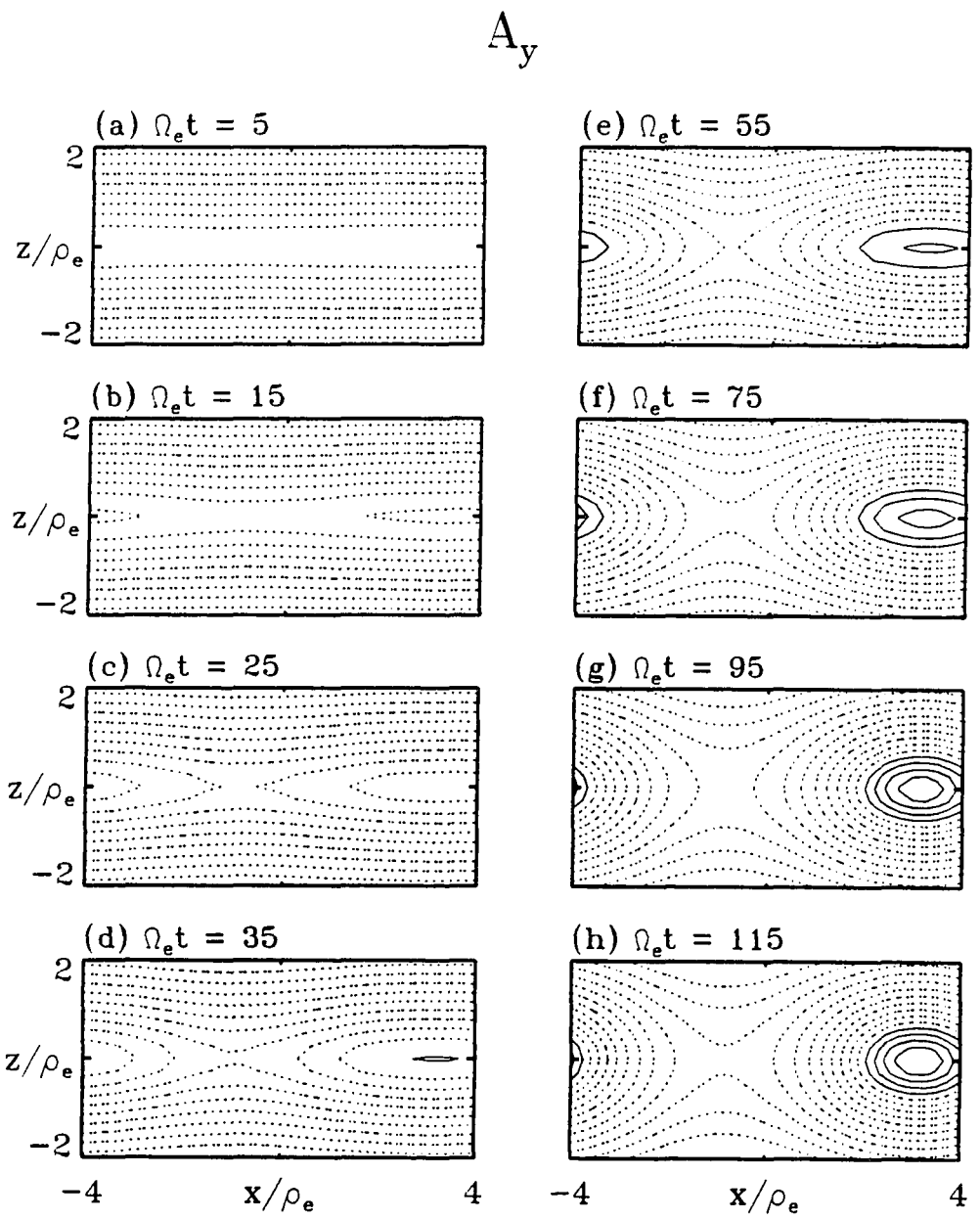

Figure 3.1 Magnetic field lines at various simulation times. A magnetic island is formed with the presence of a reconnection X line and an O line. Our simulation domain is $-4\rho_e \leq x \leq 4\rho_e$ and $-4\rho_e \leq z \leq 4\rho_e$. Only half of the simulation domain ($|x| \leq 4\rho_e$, $|z| \leq 2\rho_e$) is plotted.

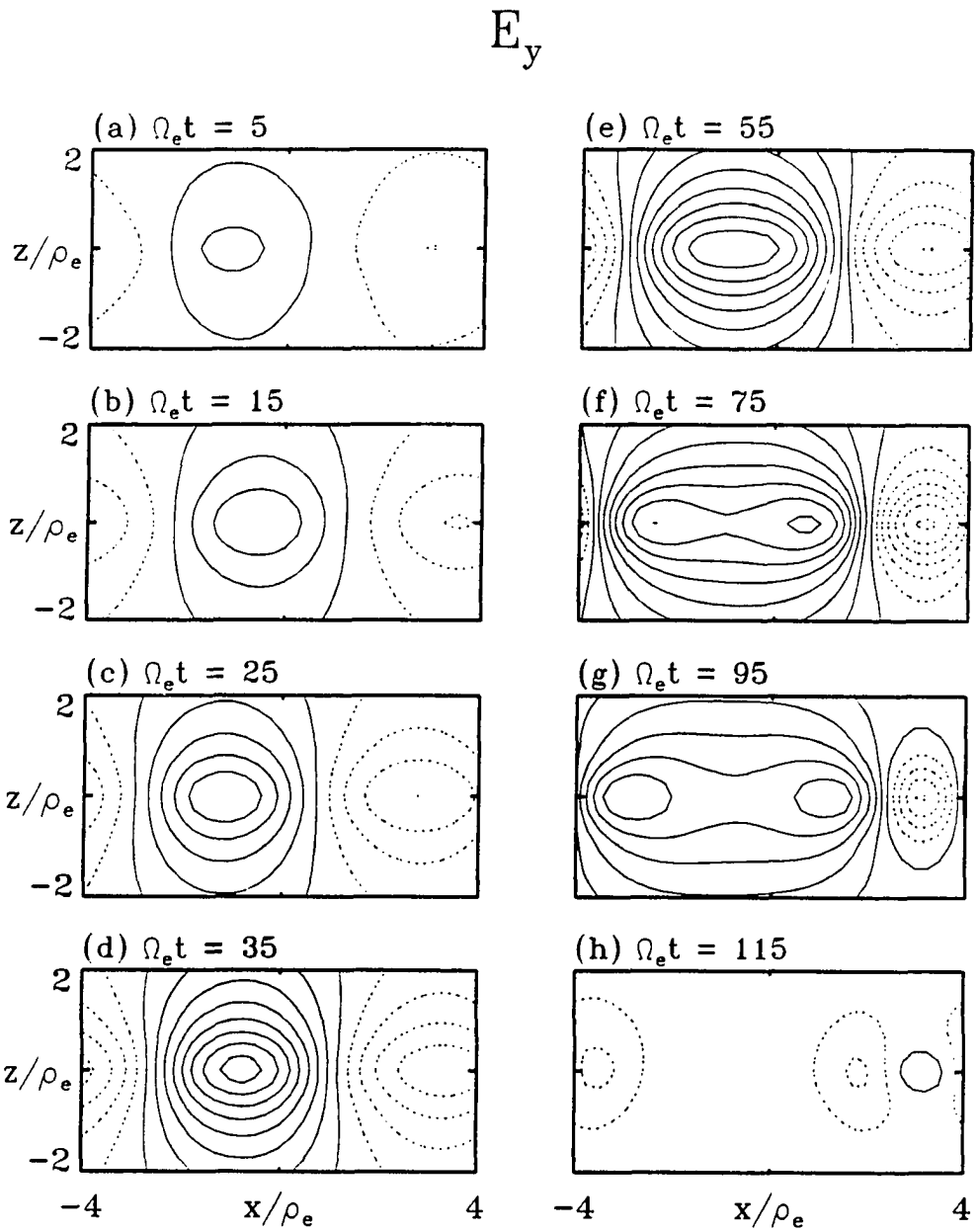

Figure 3.2 Contours of the reconnection electric field E_y in the $x - z$ plane. The increment of E_y between two neighboring contour lines is 0.0025 E_0, where $E_0 = B_0 v_{the}$.

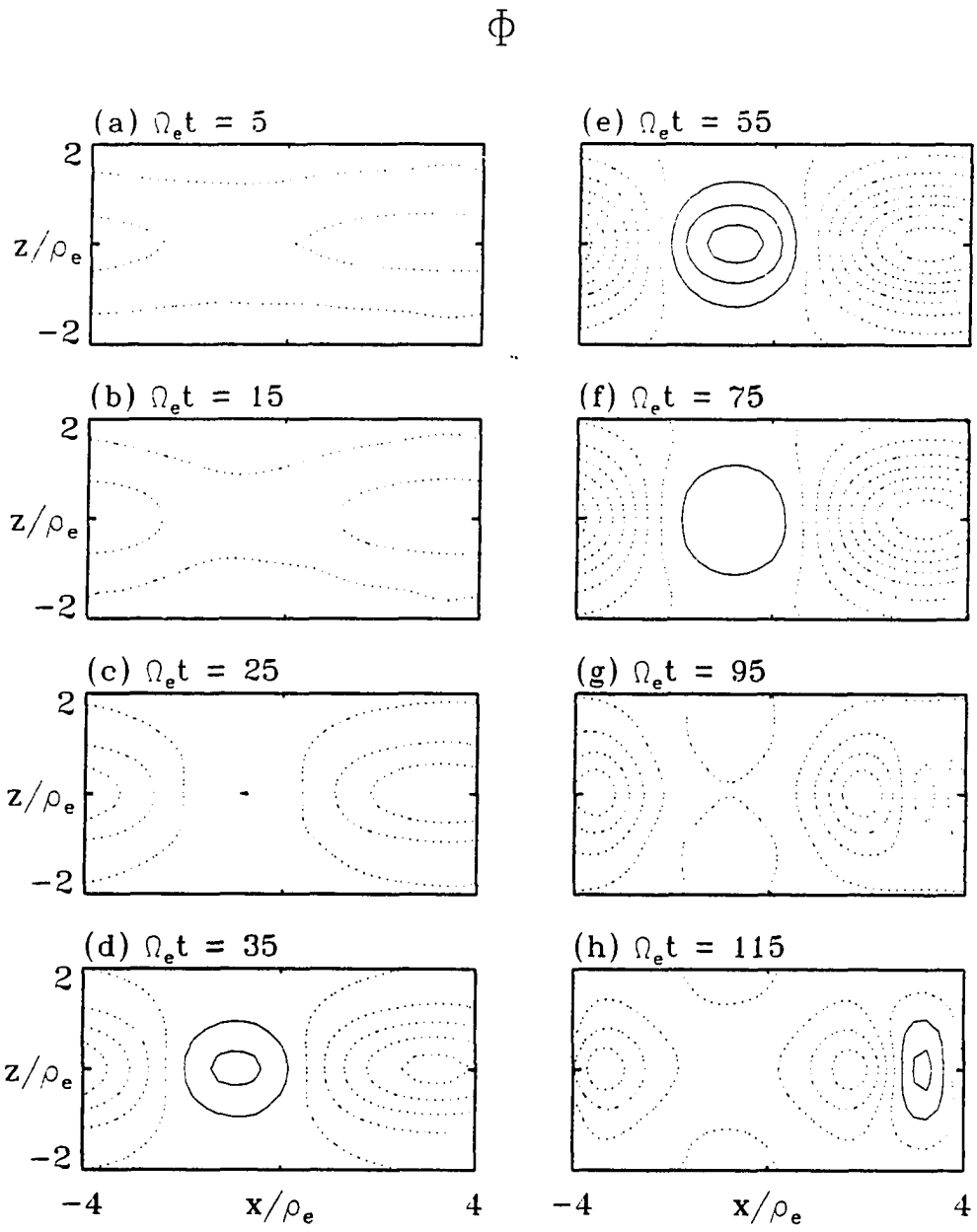

Figure 3.3 Contours of the electrostatic potential in the $x - z$ plane at different times. The increment between neighboring contours is $0.2\Phi_0$, where $\Phi_0 = B_0 v_{the} \rho_e$. Note that the electric field in the $x - z$ plane can be as large as $E_0 = B_0 v_{the}$, which is almost two orders larger than the reconnection electric field E_y.

boundaries $z = \pm 4\rho_e$. The increment of Φ between two neighboring contours is $0.2\Phi_0$ with $\Phi_0 = B_0 v_{the}\rho_e$. It is seen from Figure 3.3 that the electric potential is positive at the magnetic X line and negative at the O line from $t = 25\Omega_e^{-1}$ to $t = 75\Omega_e^{-1}$. As the magnetic reconnection proceeds, the magnetized electrons move faster than ions toward the O line and the ions are then pulled toward the O line by the electrostatic field. At $t = 115\Omega_e^{-1}$, the electrostatic potential is positive at the O line and negative at the X line. Simulation data show that at this time electron flow and ion flow are moving outward from the O line and the electron flow is faster than the ion flow. The tendency that electron bulk flow is faster than ion flow leads to the presence of current in the $x - z$ plane and is consistent with the generation of B_y shown in Figure 3.4. The electric field in the $x - z$ plane can be as large as $1.0E_0$, which is almost two orders larger than the reconnection electric field E_y. The interaction between ions and electrons is mainly through the electrostatic field in this case.

Figure 3.4 shows contours of constant B_y, where B_y is the generated magnetic field in the y direction due to the magnetic reconnection. Quadrupole patterns about the X line or the O line are clearly seen, indicating the difference between ion flows and electron flows into or out of the O line. The increment between the neighboring contours is 0.002. The generated B_y in this case is rather weak with $|B_y| < 0.01B_0$. It is expected that the generated B_y does not affect the particle dynamics in the electron diffusion region, where electrons are not completely magnetized. On the other hand, a large B_y field is observed in the hybrid simulation of magnetic reconnection [Mandt et al., 1994], in which electrons are treated as a magnetized fluid. It is interesting to note that the generation of B_y is also observed in the external shock region, as demonstrated in hybrid simulations of rotational discontinuity [Swift and Lee, 1983] and Riemann

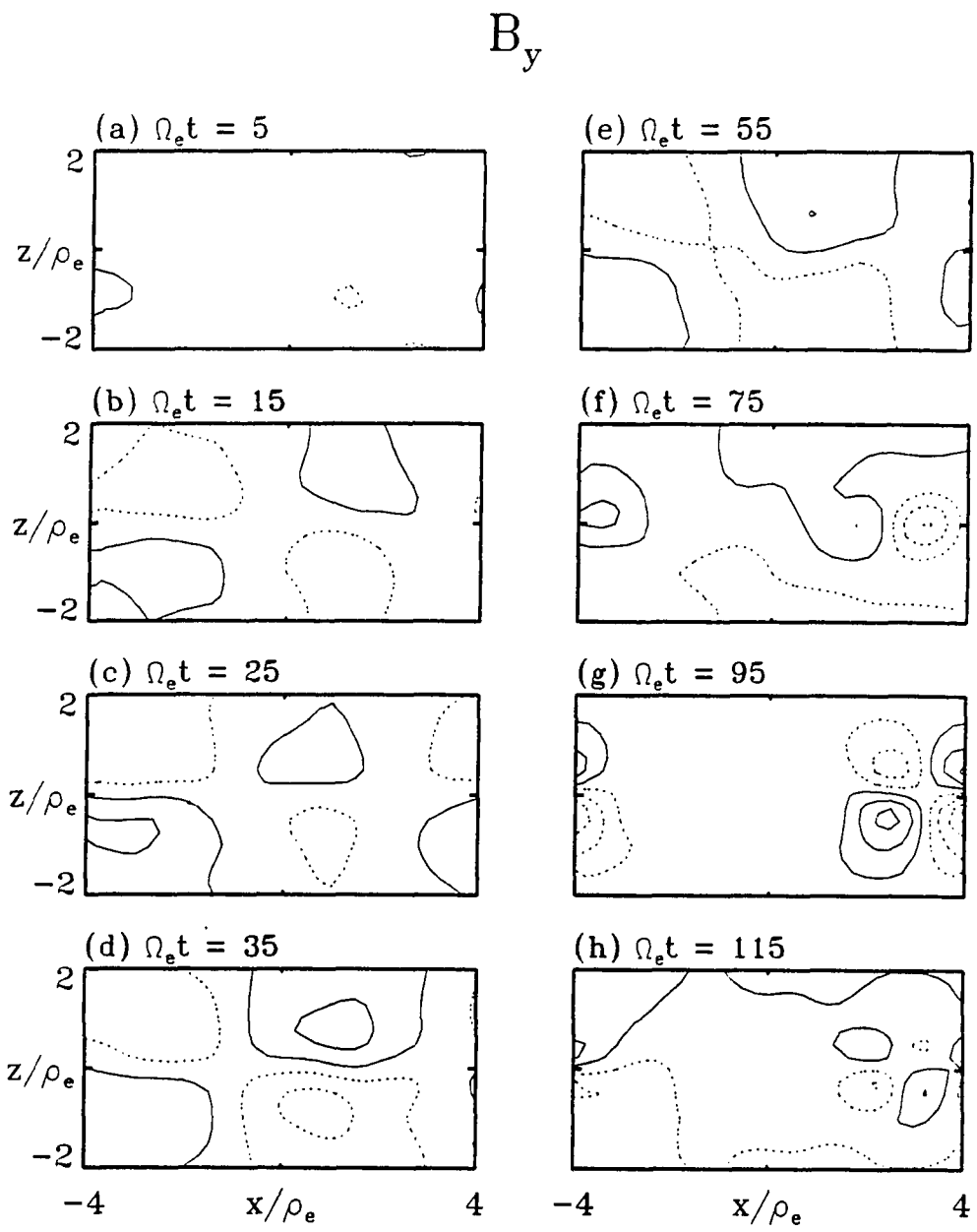

Figure 3.4 Contour plots of constant B_y. The increment between neighboring contours is $0.002B_0$. The generated B_y is very weak.

problems [Lin and Lee, 1993]. In all cases, the Hall effect due to the decoupled motion of magnetized electrons and unmagnetized ions leads to the generation of B_y.

3.3 Force balance at neutral lines for electrons

As mentioned in Chapter 2, one should be very careful in extracting the off-diagonal terms because they are very small compared with the diagonal terms. In our simulation, the zeroth-order, the first-order and the second-order moments of velocity distribution are evaluated from particles sampled five times in every 20 time steps on each grid. We then obtain the plasma density n_α, momentum density $n_\alpha m_\alpha \mathbf{v}^{(\alpha)}$, and kinetic pressure tensor $\mathbf{K}^{(\alpha)}$ by averaging these quantities both in space and in time. The thermal pressure tensor $\mathbf{P}^{(\alpha)}$ is calculated from the equation $\mathbf{P}^{(\alpha)} = \mathbf{K}^{(\alpha)} - n_\alpha m_\alpha \mathbf{v}^{(\alpha)}\mathbf{v}^{(\alpha)}$ for both electrons and ions.

Figures 3.5 and 3.6 show respectively the evolution of the off-diagonal elements of pressure tensor, $P_{xy}^{(e)}$ and $P_{zy}^{(e)}$, in the $x-z$ plane. The pressure tensor terms are normalized by $P_0 = B_0^2/2\mu_0$. The solid lines correspond to positive values, and the dotted lines correspond to negative values. The increment between neighboring contours is $0.0032P_0$. Figure 3.5 shows that a clear pattern of $P_{xy}^{(e)}$ emerges from $t = 15\Omega_e^{-1}$ and the pattern becomes complicated after $t = 75\Omega_e^{-1}$. The maximum $P_{xy}^{(e)}$ is less than $0.03P_0$, indicating that the electron distribution is only weakly skewed in the $v_x - v_y$ velocity space. The $P_{zy}^{(e)}$ contours in Figure 3.6 also show coherent patterns near the neutral lines. Note that a relative strong $P_{zy}^{(e)}$ at $t = 5\Omega_e^{-1}$ results from initial particle loading.

We plot in Figure 3.7 and Figure 3.8 the time-evolution of each term in the force balance equation (1.10) at the X line ($x \simeq -0.9\rho_e$, $z = 0$) and at the O line ($x \simeq 3.1\rho_e$,

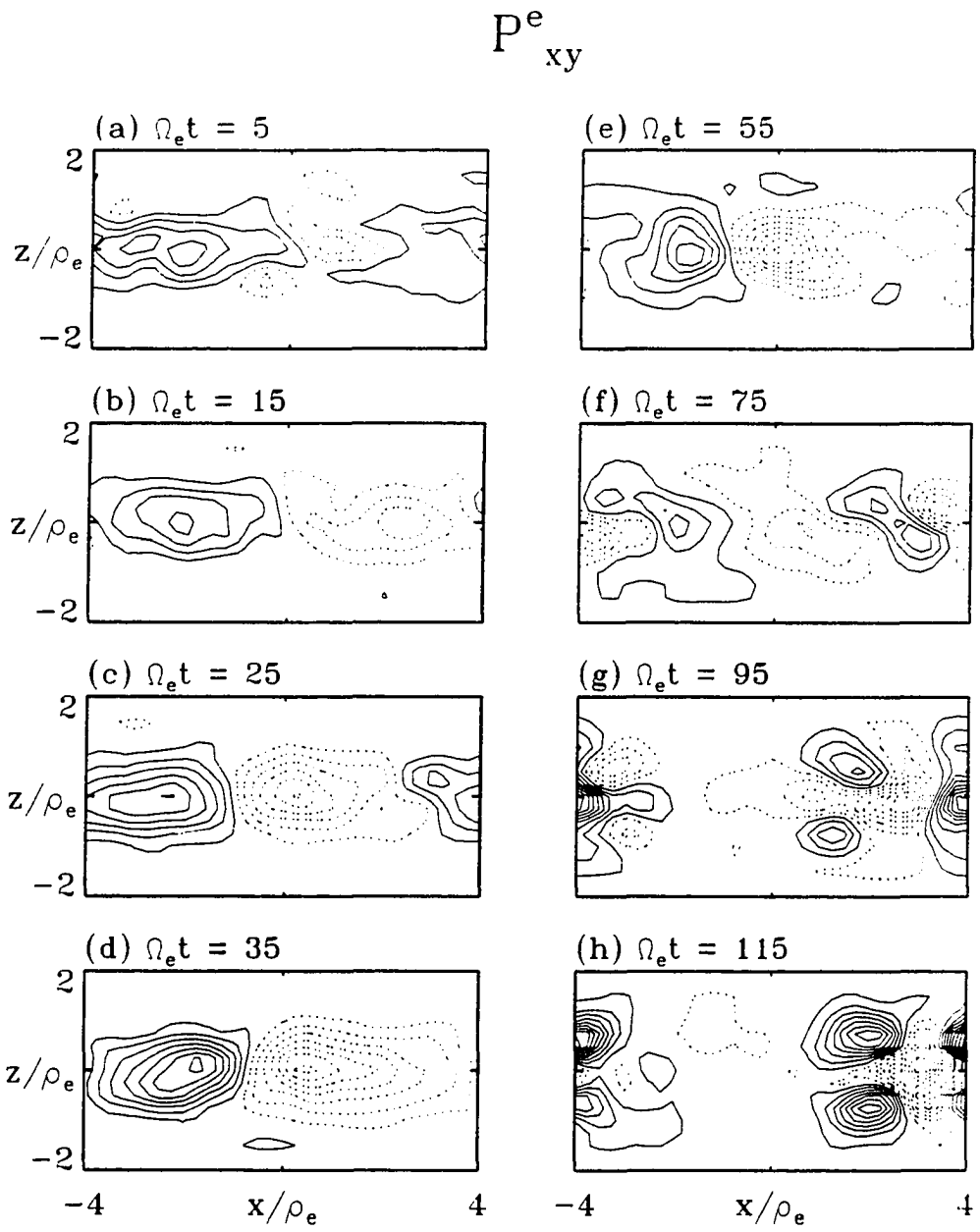

Figure 3.5 The contour lines of $P_{xy}^{(e)}$ are plotted in the $x - z$ plane at various times. The increment between neighboring contours is $0.0032P_0$, where $P_0 = B_0^2/2\mu_0$.

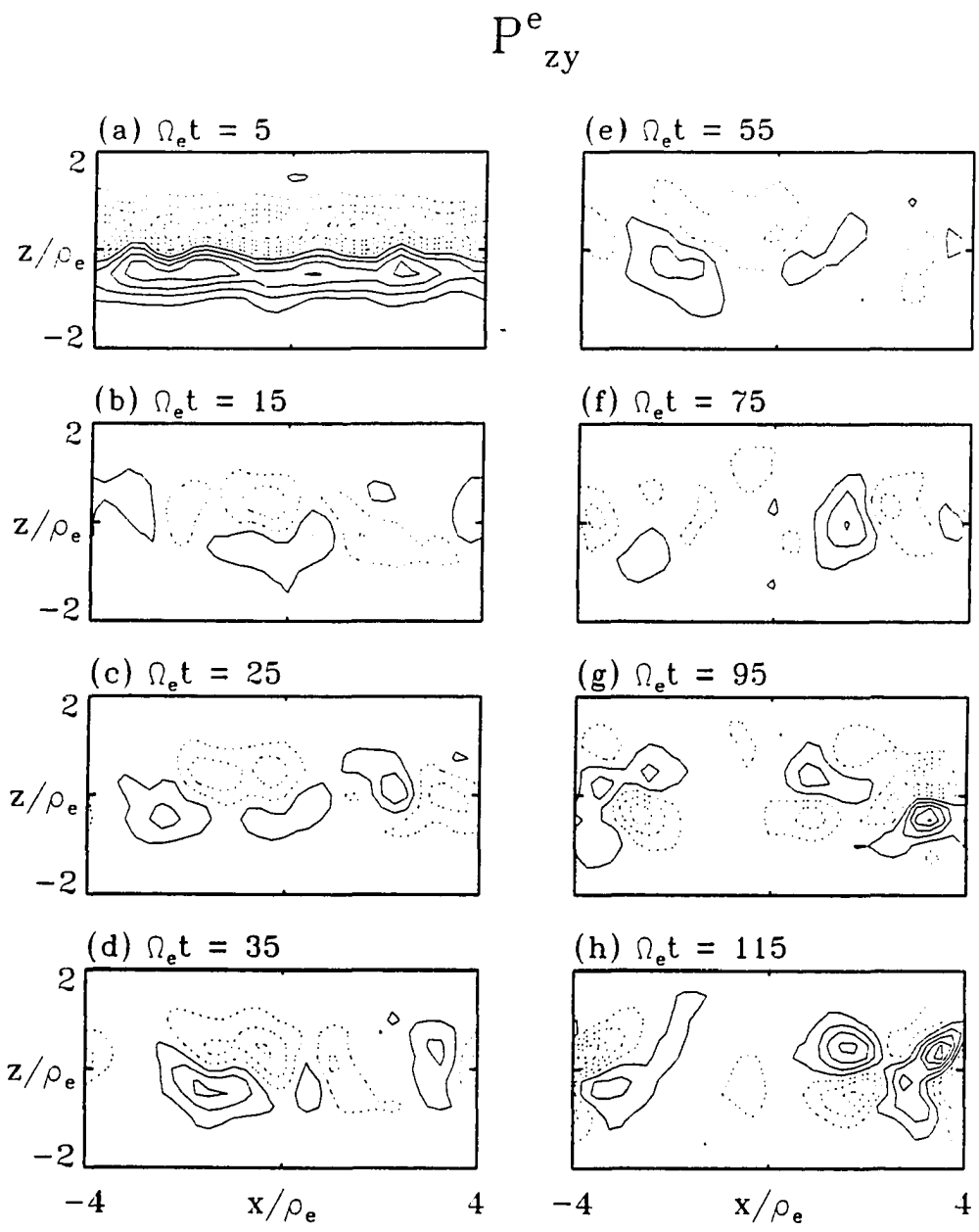

Figure 3.6 Same as Figure 3.5 except for $P^{(e)}_{zy}$.

$z = 0$), respectively. For convenience equation (1.10) is rewritten as

$$-\frac{m_e}{e}\frac{\partial v_y^{(e)}}{\partial t} = E_y + \frac{1}{n_e e}\frac{\partial P_{xy}^{(e)}}{\partial x} + \frac{1}{n_e e}\frac{\partial P_{zy}^{(e)}}{\partial z} \tag{3.10}$$

All terms in (3.10) are normalized by $E_0 = B_0 v_{the}$ in Figures 3.7 and 3.8.

In Figure 3.7*a*, the dotted line corresponds to the y momentum transport in the x direction, $(1/n_e e)\partial P_{xy}^{(e)}/\partial x$, the dashed line corresponds to the y momentum transport in the z direction, $(1/n_e e)\partial P_{zy}^{(e)}/\partial z$, and the dotted-dash line is the reconnection electric field, E_y. The solid line in Figure 3.7*b* shows the sum of the above three terms, which is the right-hand side of (3.10), whereas the broken line in Figure 3.7*b* shows the inertial term, $-(m_e/e)\partial v_y^{(e)}/\partial t$, corresponding to the acceleration of electrons in the $-y$ direction. Note that the initial drift velocity of electrons is in the $-y$ direction.

It can be clearly seen from Figure 3.7*b* that the inertial term is approximately balanced by the sum of the three terms in Figure 3.7*a*. However, the electron bulk velocity in the $-y$ direction is decelerated although the reconnection electric field tends to accelerate it, indicating that the momentum transport due to the off-diagonal elements of electron pressure tensor gives rise to a greater force than the reconnection electric field and dominate the dynamics along the X line.

Figure 3.8 is the same as Figure 3.7 except for the electron force balance at the O line. It is seen that the momentum transport due to the off-diagonal pressure terms still plays a significant role but not a dominant one.

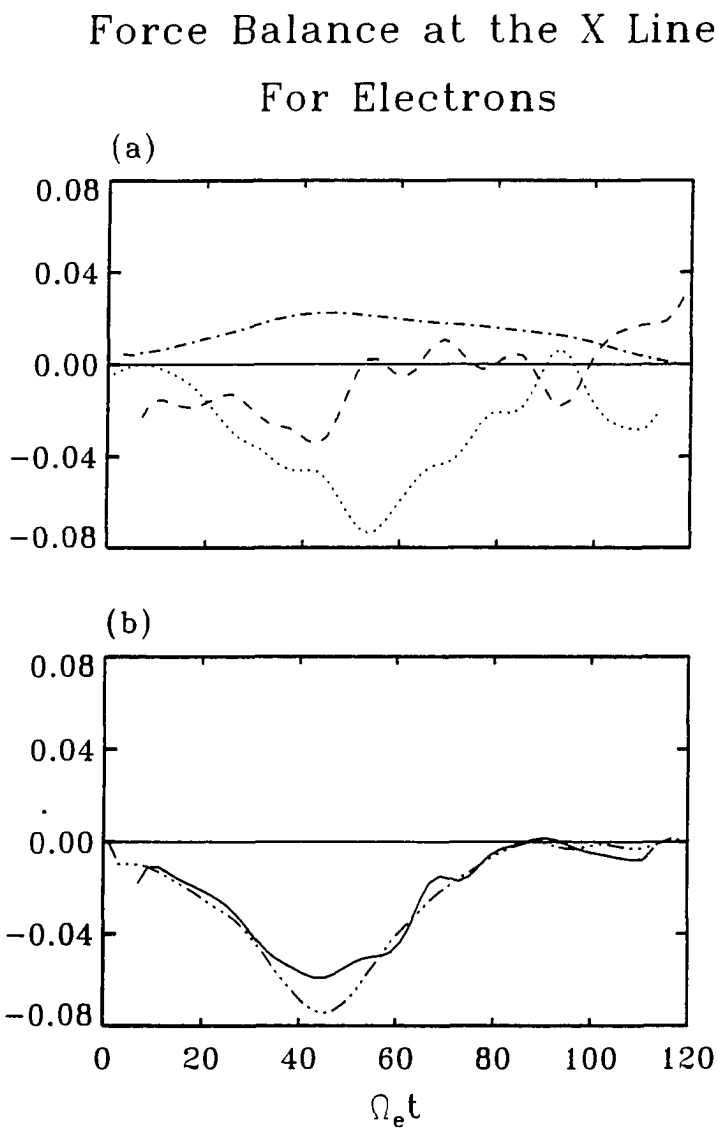

Figure 3.7 Force balance at the X line for electrons. (a) Time evolution of the three terms during reconnection: the term $(1/n_e e)\partial P_{xy}^{(e)}/\partial x$ is drawn with the dotted line, $(1/n_e e)\partial P_{zy}^{(e)}/\partial z$ with dashed line, and the reconnection electric field, E_y, the dotted-dash line. (b) The sum of the three terms in Figure 3.7a is plotted with solid line, and the inertial term, $-(m_e/e)\partial v_y^{(e)}/\partial t$, is plotted with broken line. All these terms are normalized by $E_0 = B_0 v_{the}$.

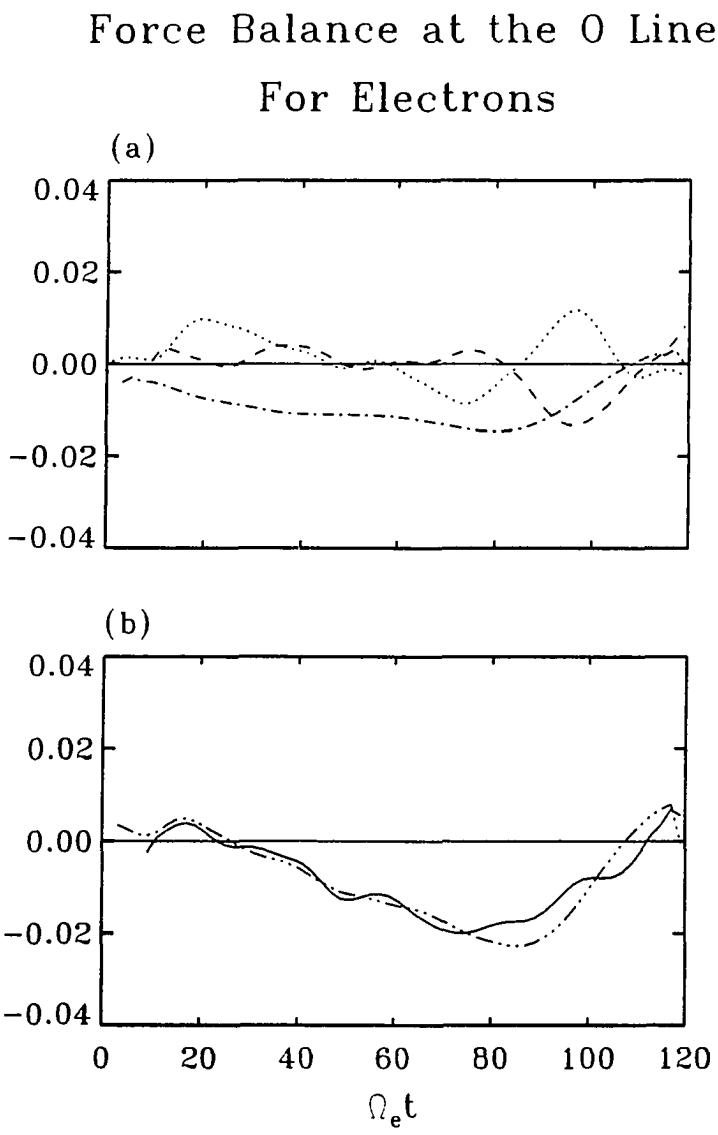

Figure 3.8 Same as Figure 3.7 except for the force balance at the O line.

3.4 Force balance at neutral lines for ions

Figures 3.9 and 3.10 show the evolution of the off-diagonal elements of pressure tensor, $P_{xy}^{(i)}$ and $P_{zy}^{(i)}$, in the $x-z$ plane. The pressure tensor terms are normalized by $P_0 = B_0^2/2\mu_0$. The solid lines correspond to positive values, and the dotted lines correspond to negative values. The increment between neighboring contours is $0.32P_0$. Figure 3.9 shows that a clear pattern of $P_{xy}^{(i)}$ emerges from $t = 35\Omega_e^{-1}$ and the pattern becomes complicated after $t = 115\Omega_e^{-1}$. The off-diagonal term $P_{xy}^{(i)}$ can be as large as $4.5P_0$, indicating that the ion velocity distribution is strongly anisotropic. The $P_{zy}^{(i)}$ contours in Figure 3.10 also show coherent patterns near the neutral lines. Note that the off-diagonal term $P_{zy}^{(i)}$ at early times ($t < 75\Omega_e^{-1}$) results mainly from the initial particle loading.

We rewrite the force balance equation for ions (1.11) as the following.

$$\frac{m_i}{e}\frac{\partial v_y^{(i)}}{\partial t} = E_y - \frac{1}{n_i e}\frac{\partial P_{xy}^{(i)}}{\partial x} - \frac{1}{n_i e}\frac{\partial P_{zy}^{(i)}}{\partial z} \tag{3.11}$$

Force balance for ions at the X line and the O line is presented in Figure 3.11 and Figure 3.12, respectively. In these figures all terms in (3.11) are normalized by $E_0 = B_0 v_{the}$.

In Figure 3.11*a*, the dotted line corresponds to the y momentum transport in the x direction, $-(1/n_i e)\partial P_{xy}^{(i)}/\partial x$, the dashed line corresponds to the y momentum transport in the z direction, $-(1/n_i e)\partial P_{zy}^{(i)}/\partial z$, and the dotted-dash line is the reconnection electric field, E_y, which can hardly be seen because it is about two orders smaller than the off-diagonal ion pressure terms. The solid line in Figure 3.11*b* shows the sum of the above three terms, whereas the broken line in Figure 3.11*b* shows the inertial term,

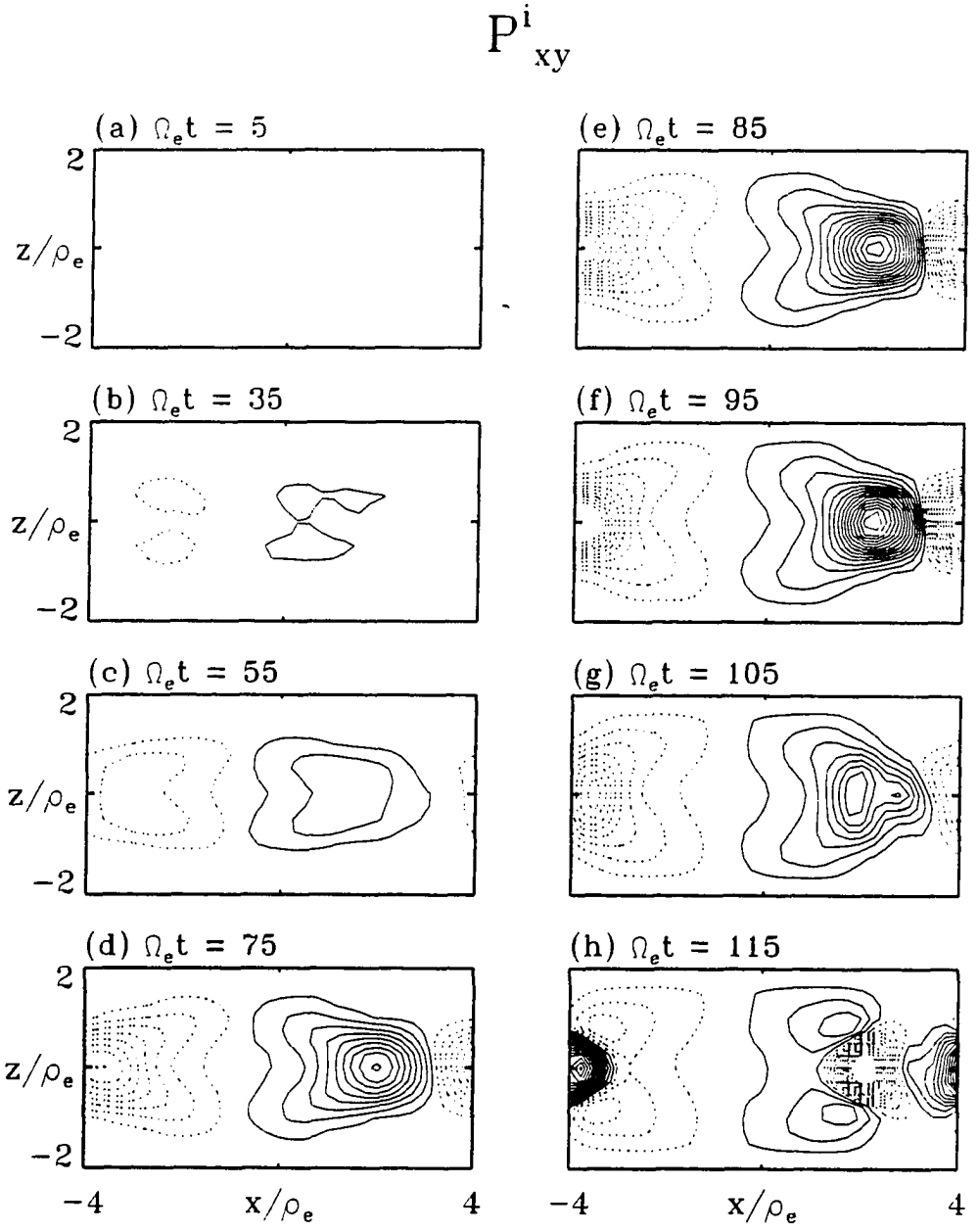

Figure 3.9 The contour lines of $P_{xy}^{(i)}$ are plotted in the $x - z$ plane at various times. The increment between neighboring contours is $0.32P_0$, where $P_0 = B_0^2/2\mu_0$.

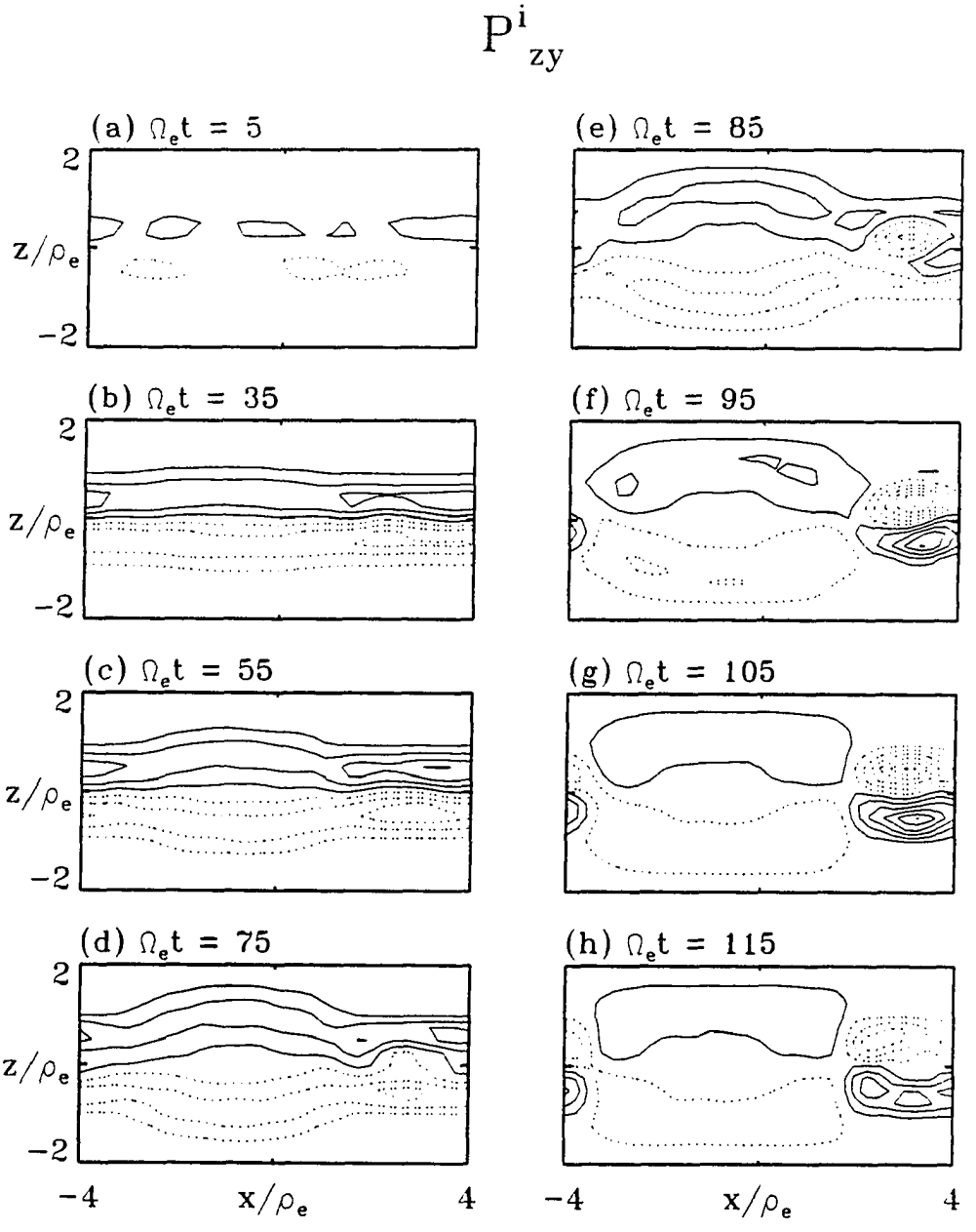

Figure 3.10 Same as Figure 3.9 except for $P_{zy}^{(i)}$.

$(m_i/e)\partial v_y^{(i)}/\partial t$, corresponding to the acceleration of ions in the y direction. The initial ion drift velocity is in the y direction.

It is seen from Figure 3.11b that the inertial term is approximately balanced by the off-diagonal ion pressure terms in Figure 3.11a. The reconnection electric field plays an insignificant role in the force balance at the X line for ions.

Figure 3.12 is the same as Figure 3.11 except for the ion force balance at the O line. It is seen that only the the off-diagonal ion pressure terms contributes to the deceleration or acceleration of ion drift velocity in the y direction. The reconnection electric field plays an insignificant role in the force balance at the O line for ions.

3.5 The generalized Ohm's near neutral lines

For convenience, we rewrite the generalized Ohm's law at neutral lines (1.12) as

$$E_y = \frac{m_e}{e^2}\frac{\partial(J_y/n)}{\partial t} + \frac{m_e}{m_i}\frac{1}{ne}\left(\frac{\partial P_{xy}^{(i)}}{\partial x} + \frac{\partial P_{zy}^{(i)}}{\partial z}\right) - \frac{1}{ne}\left(\frac{\partial P_{xy}^{(e)}}{\partial x} + \frac{\partial P_{zy}^{(e)}}{\partial z}\right) \quad (3.12)$$

by setting $1 + m_e/m_i \simeq 1$.

As shown in Figures 3.7-3.8 and 3.11-3.12, the E_y terms are about $0.02E_0$. The electron off-diagonal pressure terms can be as large as $0.08E_0$. The ion off-diagonal pressure terms are on the order of $4.0E_0$. The contribution of the ion tensor terms to (3.12) is on the order of $4.0(m_e/m_i)E_0 \simeq 0.002E_0$, which is one order smaller than the reconnection electric field. Therefore, the electron off-diagonal pressure terms play a more important role than the ion terms in the generalized Ohm's law for the case with the temperature ratio $T_i/T_e = 0.2$.

However, in the case with a larger ion-electron temperature ratio, the result can be different. We run another case with $T_i/T_e = 5$ while other parameters are the same as

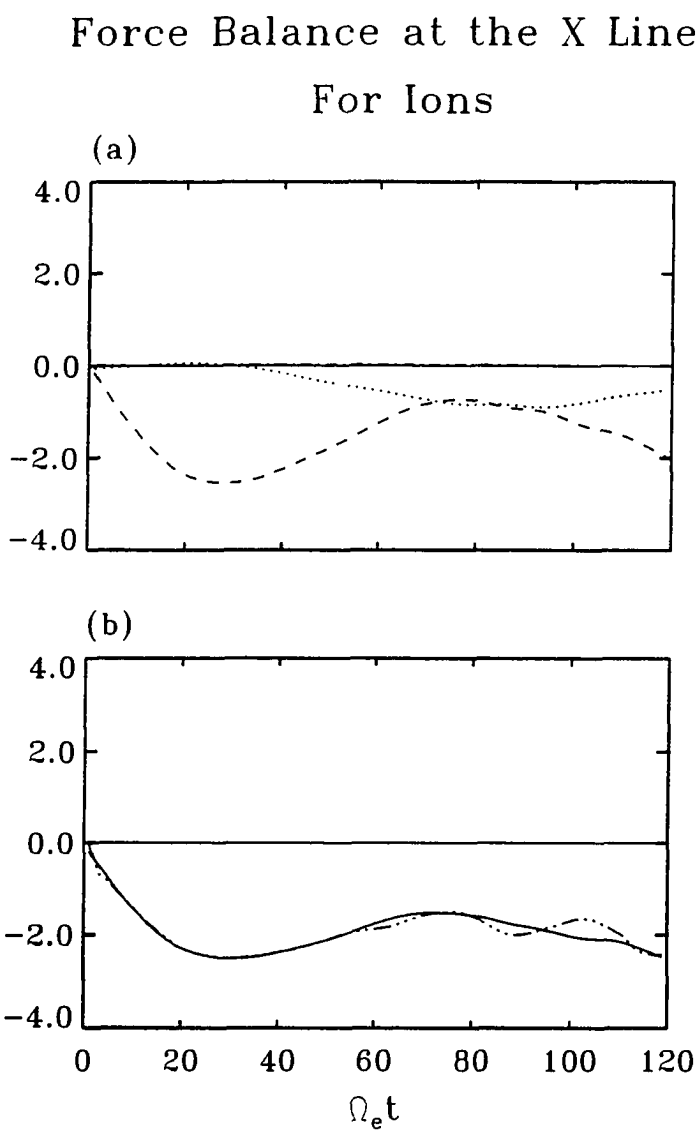

Figure 3.11 Force balance at the X line for ions. (a) Time evolution of the three terms during reconnection: the term $-(1/n_i e)\partial P_{xy}^{(i)}/\partial x$ is drawn with the dotted line, $-(1/n_i e)\partial P_{zy}^{(i)}/\partial z$ with dashed line, and the reconnection electric field, $E_y \simeq 0$, the dotted-dash line. (b) The sum of the three terms in Figure 3.11a is plotted with solid line, and the inertial term, $(m_i/e)\partial v_y^{(i)}/\partial t$, is plotted with broken line. All these terms are normalized by $E_0 = B_0 v_{the}$.

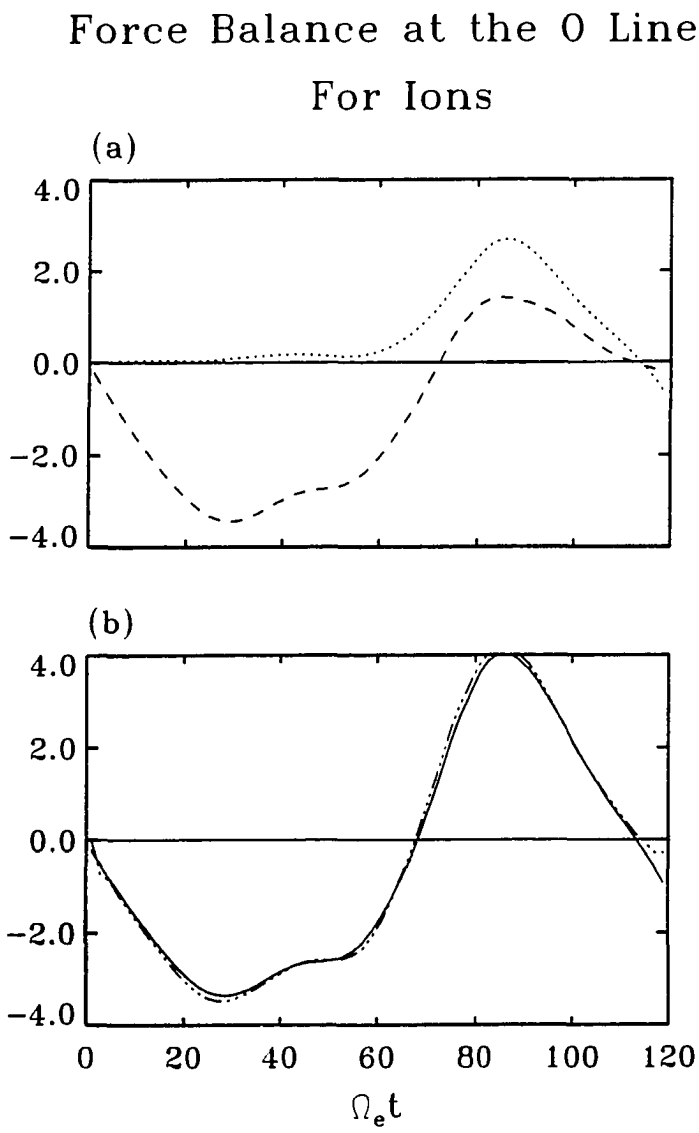

Figure 3.12 Same as Figure 3.11 except for the force balance at the O line.

those in the above case. It is found that the ion off-diagonal pressure terms are on the order of $400E_0$. The contribution of ion terms in (3.12) is $\sim 0.2E_0$, while $E_y \sim 0.02E_0$ and the electron pressure tensor terms $\sim 0.08E_0$. Therefore, the neglect of ion pressure terms in (1.7) is not justified for cases with $T_i/T_e > 1$.

3.6 Summary

Based on two-dimensional full particle simulations in which the ion-electron mass ratio is set to be 1836, we found that the off-diagonal plasma (both ion and electron) pressure terms play a very important role in the force balance equations or in the generalized Ohm's law near neutral lines (both X and O lines). The main results in our simulation study are:

(1) The off-diagonal electron pressure terms play a dominant role in the force balance for electrons at both the magnetic X line and O line.

(2) The deceleration or acceleration of ion bulk velocities in the direction of reconnection electric field (E_y) results mainly from the momentum transport due to the off-diagonal elements of ion pressure tensor; the reconnection electric field plays an insignificant role in the force balance for ions.

(3) Both the ion and electron off-diagonal pressure terms can be dominant terms in the generalized Ohm's law near neutral lines. The neglect of ion pressure terms in the conventional generalized Ohm's law (1.7) is not justified for cases with $T_i/T_e > 1$.

(4) The electrostatic fields in the $x - z$ plane are two orders larger than the reconnection electric field E_y.

CHAPTER 4

Origin of the off-diagonal pressure terms

As shown in Chapters 2 and 3, the off-diagonal pressure tensor terms play a dominant role in the generalized Ohm's law near neutral lines in collisionless magnetic reconnection. Therefore, an understanding of the origin of the off-diagonal pressure terms is of great importance.

In principle, the evolution of the pressure tensor is related to the third moments of particle velocity distribution, and the evolution of the third moments is related to the fourth moments and so on. it is not clear at present if there is a suitable closure scheme to truncate the hierarchical equations.

It is expected that the presence of the off-diagonal pressure terms is related to particle demagnetization. In the region far from the neutral sheet, particles are strongly magnetized and their velocity distribution is gyrotropic or isotropic. Therefore, the off-diagonal elements of pressure tensor vanish in the coordinates we have chosen in this thesis. In the region close to the neutral sheet, however, particle motions are rather complicated and can give rise to non-zero off-diagonal pressures.

In this chapter, we study the origin of the off-diagonal pressure terms by examining the particle motions and the response of particle distribution function in the presence of a reconnection electric field and magnetic field near the neutral lines. We also examine the spatial scale for P_{xy} based on our simulation data.

4.1 Generation of the off-diagonal pressure terms

As mentioned in Section 1.3, Dungey [1988] suggested that the presence of $P_{xy}^{(e)}$ is associated with a strong anisotropy of velocity distribution from the calculation of electron trajectories. However, in our simulation shown in Chapter 2, only weakly anisotropic distributions are present (see Figure 2.4). The weakly skewed distributions are sufficient in balancing the reconnection electric field.

In our case the generation of both P_{xy} and P_{zy} can also be explained in terms of the thermal dispersion of particle motions in the electric and magnetic fields near neutral lines.

4.1.1 Generation of P_{xy}

In order to provide a simple demonstration for the generation of P_{xy}, we consider the trajectories in the $v_x - v_y$ plane of four typical ions near the X line during the normal reconnection with $E_y > 0$. In Figure 4.1*a*, the electric field E_y and the magnetic field B_z in the $x - y$ plane ($z = 0$) are marked. The X line is located along the y axis. The positions of $x = \pm x_1$ are also marked, where x_1 is much smaller than the ion gyroradius. In Figure 4.1*b*, we plot the locations of these four particles on the $v_x - v_y$ plane when their positions are at $x = -x_1$, $x = 0$ and $x = x_1$, respectively. Particles a and b move from $x = -x_1$ to $x = 0$ and then to $x = x_1$, and particles c and d move from $x = x_1$ to $x = 0$ and to $x = -x_1$. As shown in Figure 4.1*b*, the average velocity of these particles in the y direction is positive.

Let $\hat{P}_{xy}$ denote the contribution of these four particles to P_{xy}. The positions of the four particles in the $v_x - v_y$ plane are chosen such that $\hat{P}_{xy}$ is zero along the X line ($x = 0$), which is consistent with the symmetry property of P_{xy} [Vasyliunas, 1975].

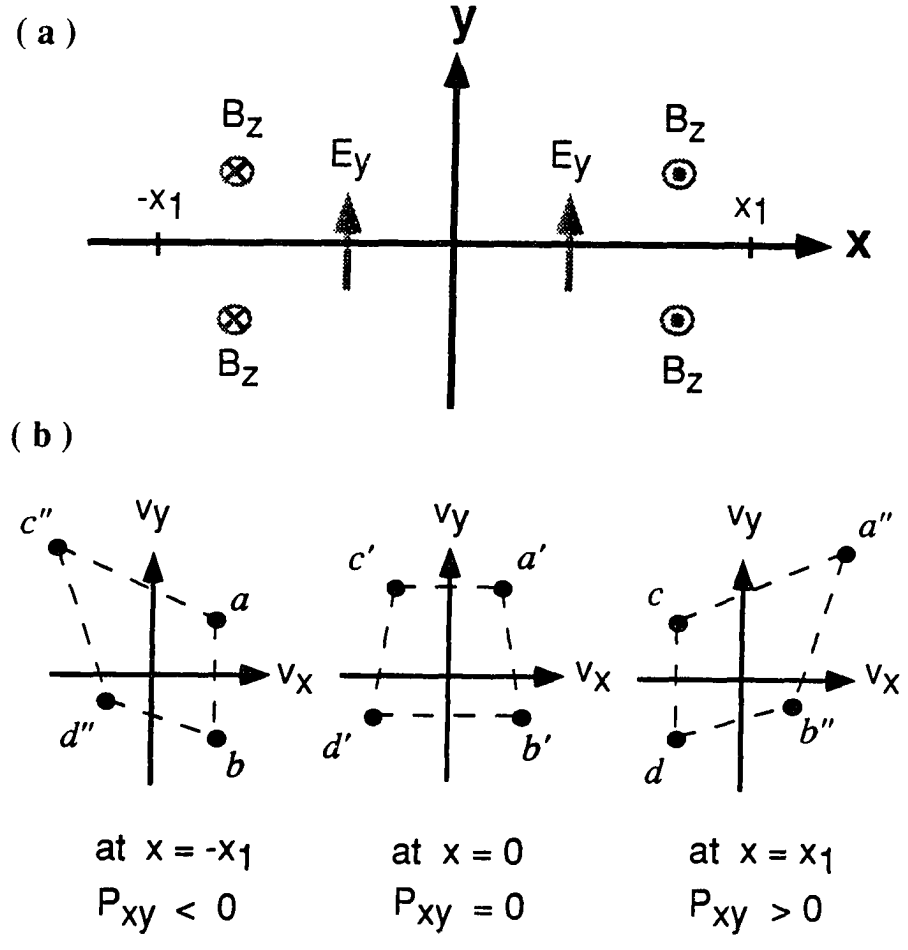

Figure 4.1 A schematic diagram for the generation of the off-diagonal pressure P_{xy} for $E_y > 0$. (a) The magnetic field B_z and the electric field E_y in the $x - y$ plane. (b) Four typical particles in the $v_x - v_y$ plane when they are at $x = -x_1$, $x = 0$ and $x = x_1$, respectively. Particles a and b move from $x = -x_1$ to $x = 0$ and then to $x = x_1$, and particles c and d move from $x = x_1$ to $x = 0$ and to $x = -x_1$. The independent motions of these particles in the electric and magnetic fields lead to deformations of velocity distribution and hence generate the off-diagonal pressure term P_{xy}.

The average velocity in the x direction at $x = 0$ is also set to zero by symmetry. The velocities of these particles at $x = 0$ are on the order of the thermal speed.

We consider the trajectories of particles a and b which move in the positive x direction. They are accelerated in the y direction by the electric field E_y as they move from $x = -x_1$ to $x = 0$ and from $x = 0$ to $x = x_1$. In addition, they are slightly rotated on the $v_x - v_y$ plane with respect to the origin of the $v_x - v_y$ plane due to the weak magnetic field B_z. As particle a moves from $x = -x_1$ to $x = 0$, its v_y increases while v_x decreases. As particle a moves from $x = 0$ to $x = x_1$, v_y increases and so does v_x. Therefore v_x and v_y of particle a are relatively large at $x = x_1$. For particle b, as it moves from $x = -x_1$ to $x = 0$, both v_y and v_x increase. As particle b moves from $x = 0$ to $x = x_1$, v_y increases but v_x decreases.

The same arguments can be applied to particles c and d, which move in the negative x direction. The final distributions of these particles in the $v_x - v_y$ plane at $x = -x_1$ and $x = x_1$ are shown in Figure 4.1*b*. These distributions lead to $\hat{P}_{xy} < 0$ at $x = -x_1$ and $\hat{P}_{xy} > 0$ at $x = x_1$.

Note that our argument does not contradict with the chaotic feature of a particle's orbit [Martin, 1986]. The chaotic feature refers to the long time behavior of the orbit. In our discussion, however, only a segment of the orbit is concerned. In addition, the velocity change of any particle obeys the same rules deduced from Newton's law when it moves, for example, from a to a' regardless the history of the particle's orbit.

It should be emphasized that both the acceleration due to E_y and the rotation due to B_z reinforce each other in generating the skewing of velocity distribution function.

4.1.2 Generation of P_{zy}

Similar explanation is also applicable to the generation of P_{zy} near the X line. Now, we consider the trajectories in the $v_y - v_z$ plane of four typical ions. The magnetic field B_x in the $y - z$ plane ($x = 0$) and the reconnection electric field $E_y > 0$ are marked in Figure 4.2*a*. The positions of $z = \pm z_1$ on the z-axis are also marked. The X line is along the y axis. In Figure 4.2*b*, we plot the locations of these four particles on the $v_y - v_z$ plane when their positions are at $z = -z_1$, $z = 0$ and $z = z_1$, respectively. Particles a and b move from $z = -z_1$ to $z = 0$ and then to $z = z_1$, and particles c and d move from $z = z_1$ to $z = 0$ and to $z = -z_1$.

Particles a and b are accelerated in the y direction by the electric field E_y as they move from $z = -z_1$ to $z = z_1$. In addition, they are slightly rotated on the $v_y - v_z$ plane with respect to the origin of the $v_y - v_z$ plane due to magnetic field B_x. As particle a moves from $z = -z_1$ to $z = 0$, its v_y increases and so does v_z. As particle a moves from $z = 0$ to $z = z_1$, v_y increases but v_z decreases. Therefore, for particle a, its v_y increases but its v_y does not change much as it moves from $z = -z_1$ to $z = z_1$. For particle b, as it moves from $z = -z_1$ to $z = 0$, v_y increases but v_z decreases. As particle b moves from $z = 0$ to $z = z_1$, both v_y and v_z increases. The same arguments can be applied to particles c and d, which move in the negative z direction. The final distributions of these particles in the $v_y - v_z$ plane at $z = -z_1$ and $z = z_1$ are shown in Figure 4.2*b*. These distributions lead to $\hat{P}_{zy} < 0$ at $z = -z_1$ and $\hat{P}_{zy} > 0$ at $z = z_1$, where $\hat{P}_{zy}$ denotes the contribution of these four particles to P_{zy}.

It is noticed that the rotation due to B_x tends to reduce the skewing of distribution function in the $v_y - v_z$ space generated by the acceleration due to E_y. This is consistent

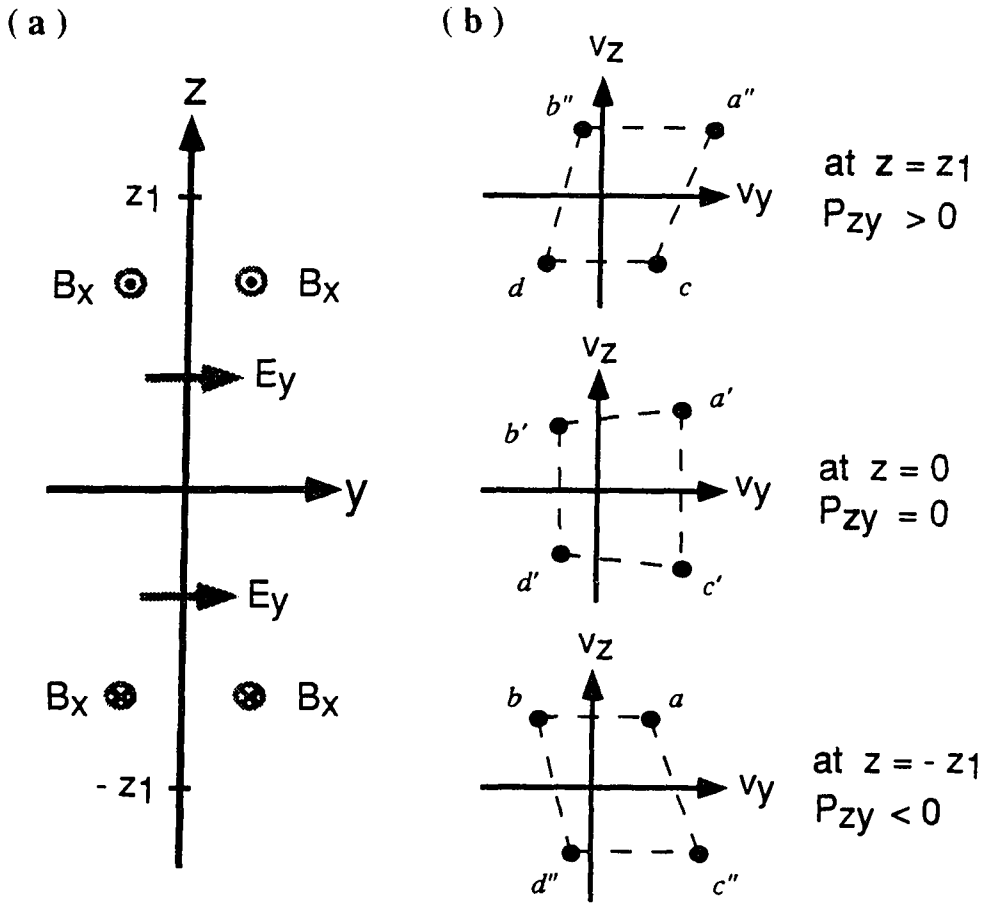

Figure 4.2 A schematic diagram for the generation of the off-diagonal pressure P_{zy} for $E_y > 0$. (a) The magnetic field B_x and the electric field E_y in the $y - z$ plane. (b) Four typical particles in the $v_y - v_z$ plane when they are at $z = -z_1$, $z = 0$ and $z = z_1$, respectively. Particles a and b move from $z = -z_1$ to $z = 0$ and then to $z = z_1$, and particles c and d move from $z = z_1$ to $z = 0$ and to $z = -z_1$. The independent motions of these particles in the electric and magnetic fields lead to deformations of particle distribution in the $v_y - v_z$ space and hence generate the off-diagonal pressure term P_{zy}.

with the result shown in Chapters 2 and 3 that the magnitude of P_{zy} is usually smaller than that of P_{xy}.

4.2 Scale length for P_{xy}

In this section, we determine the scale length of P_{xy} from our simulation data and compare the result with the scale length in (1.14a) given by Dungey [1988].

4.2.1 Scale length of P_{xy} for the case with one active species

In Chapter 2, we have presented a particle simulation case in which only ions are treated as active particles while electrons are assumed to provide a neutralized background. In this case, the off-diagonal pressure tensor term P_{xy} shown in Figure 2.5 has a coherent pattern from $t = 20\Omega_i$ to $t = 50\Omega_i$. The distance between the X line ($x = 0$ in this case) and the minimum or the maximum of P_{xy} can be measured during that time period. We regard the distance as a typical spatial scale for P_{xy}, which is denoted by L_{Pxy}.

In Figure 4.3a, the spatial scale L_{Pxy} at different times are shown with diamonds which are connected with solid lines. The negative values of L_{Pxy} correspond to the P_{xy} patterns obtained during the period of reverse magnetic reconnection with $E_y < 0$.

From our simulation data, we can also calculate the Dungey's scale length in (1.14a), which is rewritten for ions as

$$L_D = (\frac{m_i E_y}{e\beta^2})^{\frac{1}{3}}, \tag{4.1}$$

where E_y is the reconnection electric field and $\beta = \partial B_z/\partial x$ is the gradient of magnetic field B_z along the x axis.

We use values of E_y and β at the X line to evaluate the Dungey's scale length L_D at each time. The results are shown in Figure 4.3a with triangles which are connected with dashed line. Note that the negative L_D comes from the negative E_y in (4.1). It is seen that the magnitudes of L_{Pxy} are larger than those of L_D except at $t = 20\Omega_i$. We plot L_D versus L_{Pxy} in Figure 4.3b with crosses. The scale length L_{Pxy} at $t = 20\Omega_i$ is limited by the system size and hence the data point at $t = 20\Omega_i$ is not plotted in Figure 4.3b. As shown in Figure 4.3b, all data points are almost on the dotted straight line, which is their regression line and can be expressed as

$$L_{Pxy} = 1.8L_D - 0.39\rho_i. \tag{4.2}$$

The result shown in Figure 4.3 indicates that the Dungey's scale length can be used to determine the spatial scale of the off-diagonal pressure term P_{xy} for the case with one active species.

4.2.2 Scale length of $P_{xy}^{(e)}$ for the case in a full particle simulation

In Chapter 3, we presented details of the off-diagonal pressure tensor terms for the case in a full particle simulation. In this case, the off-diagonal electron pressure term $P_{xy}^{(e)}$ shown in Figure 3.5 has a coherent pattern from $t = 15\Omega_i$ to $t = 65\Omega_i$. The distance between the X line ($x \simeq -0.9\rho_e$ in this case as shown in Figure 3.1) and the minimum or the maximum of P_{xy} can be measured during that time period. We regard the distance as a typical spatial scale for $P_{xy}^{(e)}$, which is denoted as L_{Pxy}.

In Figure 4.4a, the spatial scale L_{Pxy} at different times are shown with diamonds which are connected with solid lines. From our simulation data, we can also calculate

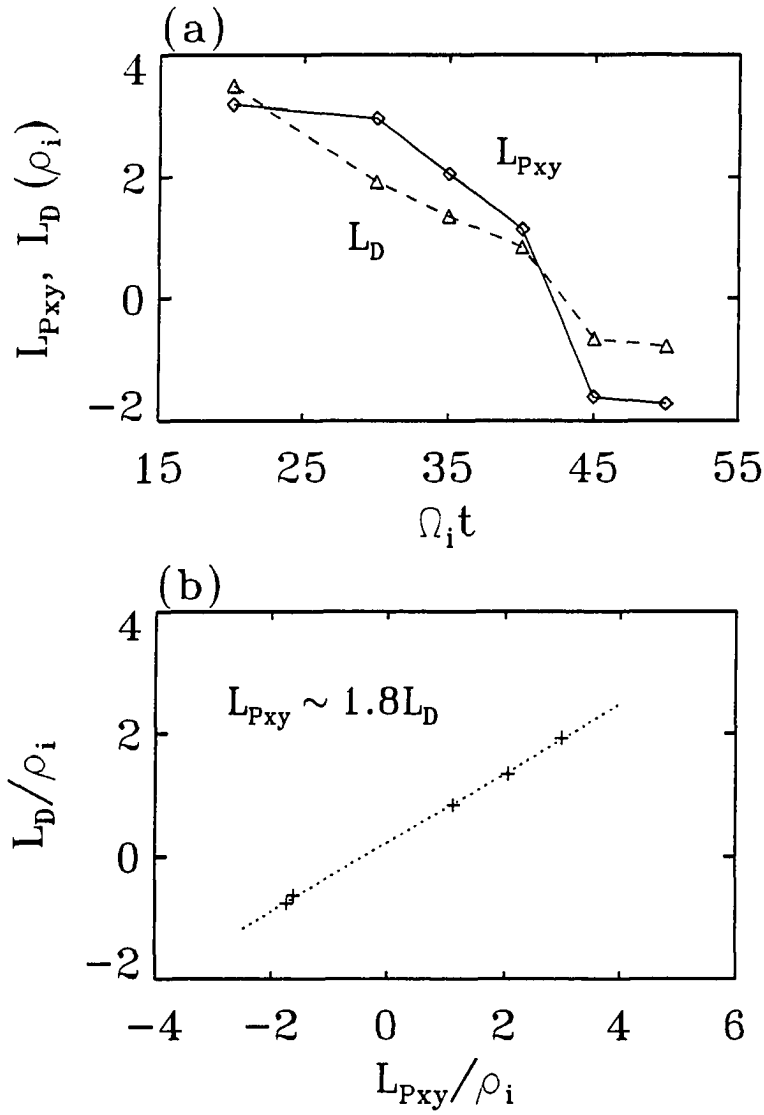

Figure 4.3 (a) L_{Pxy} and L_D as a function of time, and (b) L_D as a function of L_{Pxy} for the case shown in Chapter 2. Here L_{Pxy} is the distance from the X line to the maximum or minimum of P_{xy}, and L_D is the Dungey's scale length. The negative values of scale length are used for the period of reverse magnetic reconnection ($E_y < 0$).

the Dungey's scale length in (1.14a), which is rewritten for electrons as

$$L_D = (\frac{m_e E_y}{e\beta^2})^{\frac{1}{3}}. \tag{4.3}$$

We use values of E_y and β at the X line to evaluate the Dungey's scale length L_D at each time. The results are shown in Figure 4.4a with triangles which are connected with dashed line. It is seen that the magnitudes of L_{Pxy} are much larger than those of L_D . We plot L_D versus L_{Pxy} in Figure 4.4b with crosses. The dotted line is the regression of those points and can be expressed as

$$L_{Pxy} = 4.4L_D + 0.79\rho_e \tag{4.4}$$

The result shown in Figure 4.4 indicates that the Dungey's scale length is approximately proportional to the spatial scale of the off-diagonal pressure term $P_{xy}^{(e)}$ for the case in a full particle simulation. However, the large numerical factor 4.4 indicates that the interaction between electrons and ions through strong electrostatic fields, which is not included in the Dungey's simple model, may also be important in determining the scale length of a magnetic reconnection process.

4.3 $P_{xy}^{(e)}$ in linear tearing instability

In a kinetic treatment of linear tearing instability [e.g., Galeev, 1984; Swift, 1986], one can start from Harris' model in which

$$\mathbf{B}(z) = B_0 tanh(z/\lambda)\hat{\mathbf{e}}_x \tag{4.7}$$

and the particle distribution function

$$f_{0\alpha} = \frac{n(z)}{(\pi v_{th\alpha})^{3/2}} exp[-\frac{v_x^2 + (v_y - U_{\alpha y})^2 + v_z^2}{v_{th\alpha}^2}] \tag{4.8}$$

where $\alpha(= i, e)$ denotes ions or electrons, λ is the half thickness of the current sheet, $U_{\alpha y}$ is the constant drift velocity, $v_{th\alpha}$ is the thermal speed, and the density $n(z) =$

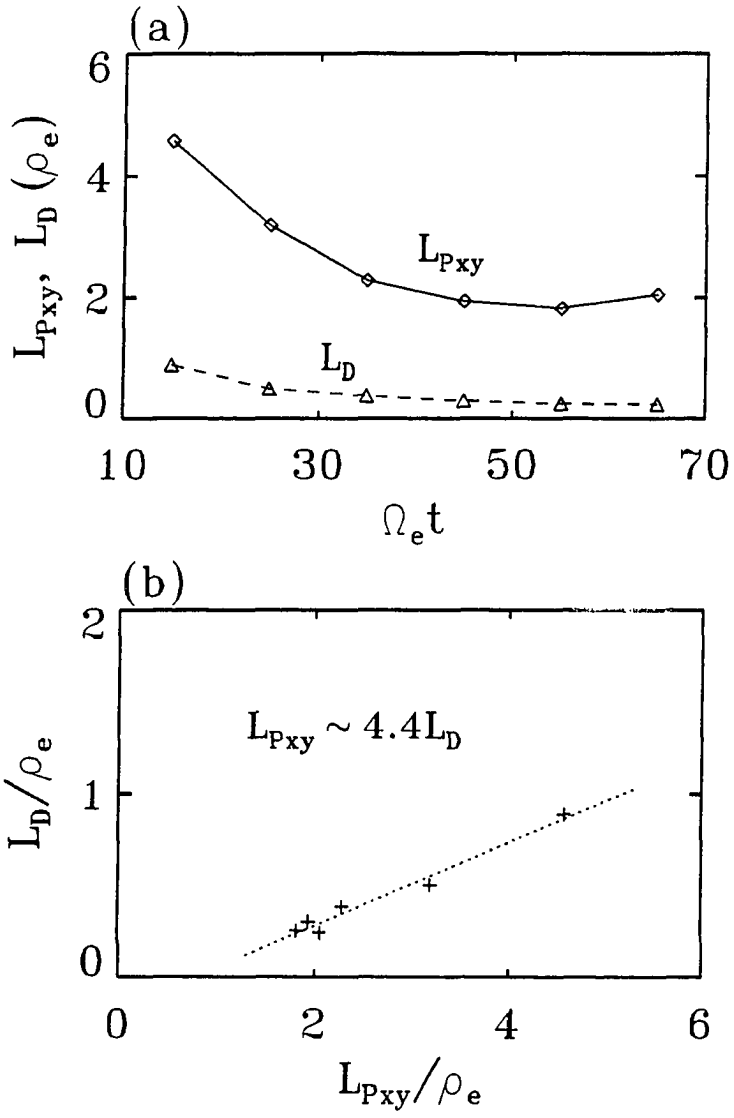

Figure 4.4 (a) L_{Pxy} and L_D as a function of time, and (b) L_D as a function of L_{Pxy} for the case shown in Chapter 3. Here L_{Pxy} is the distance from the X line to the maximum or minimum of $P_{xy}^{(e)}$, and L_D is the Dungey's scale length.

$n_0 sech^2(z/\lambda)$. A reference frame of coordinates is chosen such that $U_i/T_i = -U_e/T_e$, where T_i and T_e are thermal temperatures; hence there is no zero-order electric field in this reference frame.

Assume that the perturbed vector potential $\mathbf{A}_1 = A_{1y} e^{ik_x x + \gamma t} \hat{\mathbf{e}}_y$ and other perturbed quantities have similar forms. One obtains the first order distribution functions in the unmagnetized region, $|z| \leq d_\alpha$, by solving the linearized Vlasov equation [e.g., Swift, 1986],

$$f_{1\alpha} = \frac{q_\alpha}{T_\alpha} f_{0\alpha} \left[(U_{\alpha y} - v_y) A_{1y} + \left(\frac{k_x v_x}{k_x v_x - i\gamma}\right)(v_y A_{1y} - \phi_1) \right] \tag{4.9}$$

where $d_\alpha = (\lambda \rho_\alpha)^{1/2}$, q_α is the charge, and ρ_α is the gyroradius based on B_0. The electrostatic potential ϕ_1 is determined from the quasi-neutrality condition, $n_{1i} = n_{1e}$,

$$\phi_1 = \frac{Z'(\xi_i) - Z'(\xi_e)}{Z'(\xi_i) + (T_i/T_e) Z'(\xi_e)} U_{iy} A_{1y} \tag{4.10}$$

where $\xi_\alpha = i\gamma/(k_x v_{t\alpha})$, and $Z(\xi)$ is the plasma dispersion function. In the limit of $|\xi_{i,e}| \ll 1$, $Z'(\xi_\alpha) \simeq 1 + \xi_\alpha Z(\xi_\alpha)$ and $Z(\xi_\alpha) \simeq i\pi^{1/2}$, ϕ_1 is negligible and we have

$$J_{1y} = \frac{n(z) e^2}{m_e c} \xi_e Z(\xi_e) A_{1y} \tag{4.11}$$

In (4.11), only the non-adiabatic term from electrons is kept; this term is dominant in the region $|z| \leq d_e$.

The electron pressure tensor can be evaluated directly from the definition, $\mathbf{P}^{(e)} = m_e \int d\mathbf{v} (\mathbf{v} - \mathbf{U}_e)(\mathbf{v} - \mathbf{U}_e)(f_{0e} + f_{1e})$. From (4.8) and (4.9), we obtain the off-diagonal

elements of the pressure tensor,

$$P_{zy}^{(e)} = 0 \tag{4.12}$$

and

$$P_{xy}^{(e)} = -\frac{em_e}{T_e}(i\gamma A_{1y}) \int dv_x dv_y dv_z v_x (v_y - U_{ey}) g_1 \tag{4.13}$$

where

$$g_1(v_y, v_x) \equiv -(\frac{iv_x/\gamma}{v_x - i\gamma/k_x})(v_y - U_{ey}) f_{0e} \tag{4.14}$$

Carrying out the integration, we obtain [Cai and Lee, 1994]

$$P_{xy}^{(e)} = -en(z)(\frac{i\gamma}{k_x})[1 + \xi_e Z(\xi_e)] A_{1y} \tag{4.15}$$

From (4.15) and $E_{1y} = -\partial A_{1y}/\partial t = -\gamma A_{1y}$, we have

$$-(\frac{1}{ne})(\frac{\partial P_{xy}^{(e)}}{\partial x}) = -(\frac{ik_x}{ne}) P_{xy}^{(e)} = E_{1y} + \xi_e Z(\xi_e) E_{1y} \tag{4.16}$$

From (4.11) and (4.16), we obtain

$$E_{1y} = \frac{m_e}{ne^2}\frac{\partial J_{1y}}{\partial t} - \frac{1}{ne}(\frac{\partial P_{xy}^{(e)}}{\partial x}) \tag{4.17}$$

which is the y-component of the generalized Ohm's law in the central region ($|z| \leq d_e$) of the current sheet.

It is interesting to note that the reconnection electric field in (4.17) is mainly balanced by the gradient of $P_{xy}^{(e)}$.The inertial term, $\partial J_{1y}/\partial t$, contributes only a small part to the balance of E_{1y}.

The off-diagonal pressure term originates from the Landau resonance as indicated by the denominator in (4.14). Figure 4.5a shows the contour lines of the real part of the perturbed distribution function, $Re\ g_1$ in the $v_x - v_y$ plane. For demonstration

purpose, we choose $\gamma/(k_x v_{te}) = 0.01$ in (4.14) for this plot. The solid lines denote positive values, and the dotted lines denote negative values. The asymmetry feature of $Re\ g_1(v_y, v_x)$ leads to a non-zero $P_{xy}^{(e)}$. The distribution of $P_{xy}^{(e)}$ in the $x - z$ plane is plotted in Figure 4.5b. Note that outside the central region of the current sheet, $|z| > d_e$, electrons are strongly magnetized and $P_{xy}^{(e)}$ goes to zero. Therefore a factor of $sech^2(z/d_e)$ has been multiplied in the calculation of $P_{xy}^{(e)}$. The $P_{xy}^{(e)}$ pattern shown in Figure 4.5b is consistent with that obtained in particle simulations presented in Chapters 2 and 3.

The results in Figure 4.5 show that the off-diagonal pressure tensor term $P_{xy}^{(e)}$ can be obtained from the response of particle distribution function in the reconnection electric field near the X line.

4.4 Summary

We have examined the particle motions and the response of particle distribution function in the presence of a reconnection electric field and magnetic field near the neutral lines, which lead to the generation of the off-diagonal pressure terms. The scale length of P_{xy} is determined from our simulation data and the result is compared with Dungey's scale length. The main results are:

(1) The acceleration of particles due to E_y and the rotation of velocity due to B_z reinforce each other in the generation of P_{xy}.

(2) The rotation due to B_x tends to reduce the skewing of distribution function in the $v_y - v_z$ space generated by the acceleration due to E_y. Therefore, P_{zy} is usually smaller than P_{xy}.

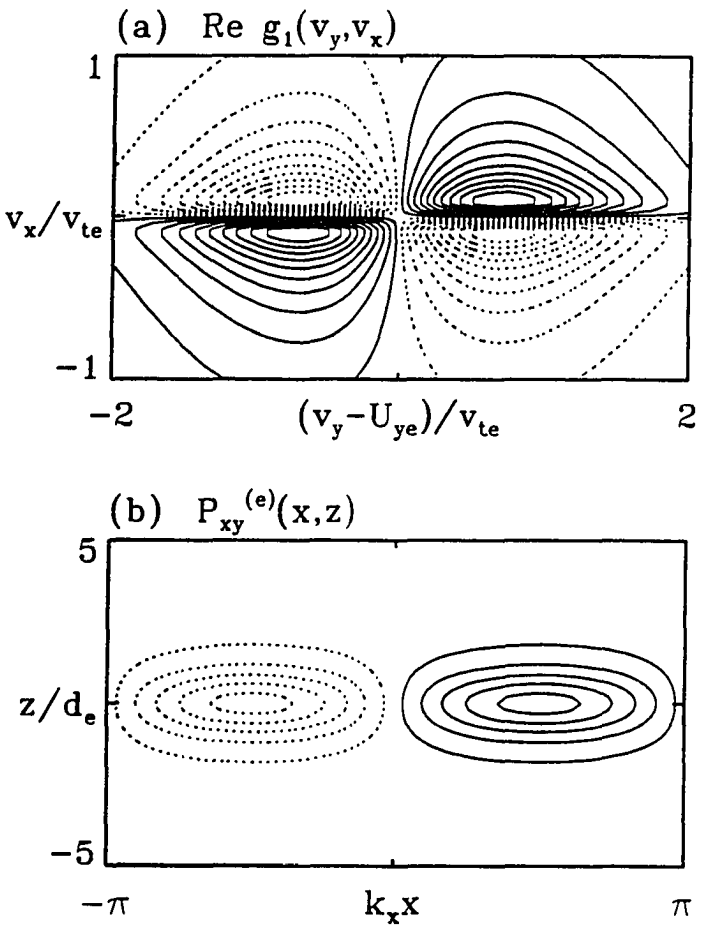

Figure 4.5 (a) Contour lines of the real part of the perturbed distribution function, $Re\ g_1$, in the $v_x - v_y$ plane. (b) The distribution of the off-diagonal pressure, $P_{xy}^{(e)}$, in the $x - z$ plane.

(3) The Dungey's scale length, $L_D = (mE_y/e\mathcal{B}^2)^{1/3}$, can be used to determine the scale length of the off-diagonal pressure term P_{xy} for the case with one active species.

(4) The modified Dungey's scale length, $L_D^* = (m_e^* E_y/e\mathcal{B}^2)^{1/3}$, with an effective electron mass $m_e^* = (\frac{m_i}{m_e})^{0.36} m_e$ due to a strong electrostatic interaction between electrons and ions, provides a good scaling for $P_{xy}^{(e)}$ in a full particle simulation.

(5) The response of particle distribution function in the reconnection electric field near the X line results in the off-diagonal pressure tensor term $P_{xy}^{(e)}$ in linear tearing instability, which is consistent with our simulation results.

CHAPTER 5

A new dynamo process near a magnetic O line

In this chapter, we report a new dynamo process, in which magnetic flux is generated near a magnetic O line inside the magnetic island formed by the tearing process. In other words, the total magnetic flux in the magnetic island is more than the reconnected magnetic flux. This dynamo process cannot exist in a resistive magnetofluid.

5.1 Generation of magnetic flux near an O line

We replot the magnetic field lines for the case studied in Chapter 3 for a longer time period in Figure 5.1. Again, the increment of A_y between two neighboring field lines is fixed so that the number of the field lines provides a measure of the magnetic flux.

Initially the value of A_y is $-3.8B_0\rho_e \leq A_y \leq 0$ ($A_y = 0$ along $z = 0$). The solid lines in these plots denote the newly generated magnetic flux. Figure 5.1a shows no solid line. A careful examination indicates that there is no magnetic flux generated in the initial stage of reconnection. Figures 5.1b – 5.1e show that more and more solid lines (up to 6) are present, which means that more and more magnetic flux is newly generated near the O line during the period from $t = 30\Omega_e^{-1}$ to $t = 110\Omega_e^{-1}$. Figures 5.1f – 5.1g show that there are 4 solid lines and Figure 5.1h shows that there are 5 solid lines, which means that the generation of magnetic flux has an oscillatory feature. The reconnected magnetic flux can be represented by the reconnected dotted lines inside the magnetic island in Figure 5.1. The variation of the number of dotted field lines is related to the

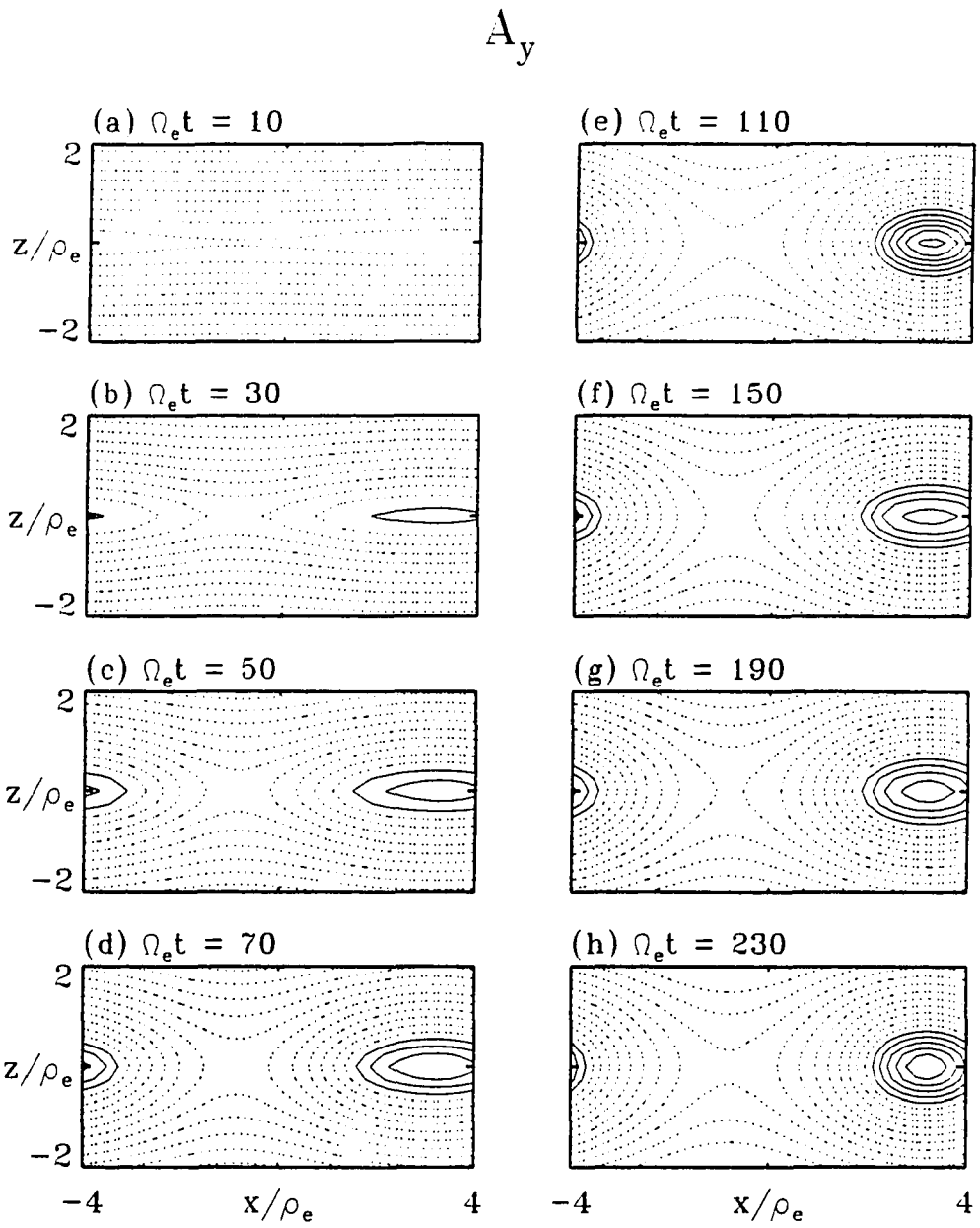

Figure 5.1 Magnetic field lines at various simulation times. A magnetic island is formed with the presence of a reconnection X line and O line. Our simulation domain is $-4\rho_e \leq x \leq 4\rho_e$ and $-4\rho_e \leq z \leq 4\rho_e$. Only the central portion ($|z| \leq 2\rho_e$) of the simulation domain is plotted.

time-integration of reconnection electric field at the X line. The newly generated flux, the reconnected flux, and the total flux within the formed magnetic island as a function of time will be plotted later.

Figures 5.2 and 5.3 show contours of the reconnection electric field E_y and the current density J_y in the $x - z$ plane, respectively. In Figure 5.2, the electric field is normalized by $E_0 = B_0 v_{the}$. The solid contours correspond to positive values, and the dotted lines correspond to negative values. The increment of E_y between two neighboring contour lines is 0.0025 E_0. Note that the electric field is zero at the simulation boundaries $z = \pm 4\rho_e$, because the value of the vector potential A_y at these boundaries is fixed. The contours in Figure 5.2 show that the electric field near the O line is negative and decreases from $t = 10\Omega_e^{-1}$ to $t = 70\Omega_e^{-1}$, and it becomes positive at $t = 110$ and $150\Omega_e^{-1}$. At $t = 190\Omega_e^{-1}$ the electric field is negative again. In Figure 5.3, the current density is normalized by $J_0 = N_e e v_{the}$. The increment of J_y between two neighboring contours is $2J_0$. The value corresponding to the outermost contour line in each plot is J_0 and the maximum value of J in Figure 5.3*e* is $J_{max} \simeq 11.5 J_0$. The contours in Figure 5.3 show that the current density near the O line increases during $t = 10 - 110\Omega_e^{-1}$ and slightly decreases during $t = 110 - 150\Omega_e^{-1}$. During the period $t = 150 - 230\Omega_e^{-1}$, the current density at the O line increases again. The enhancement of current density near the O line is mainly due to the increase of particle number density, or the compression of plasma near the O line. The plasma number density near the O line is enhanced to $\sim 3N_e$. The current density in the whole domain remains positive throughout the entire process in our simulation.

Figures 5.2*b* – 5.2*d* and 5.3*b* – 5.3*d* show that at $t = 30, 50, 70\Omega_e^{-1}$, there exists a large region around the magnetic O line where $E_y < 0$, $J_y > 0$ and hence $\mathbf{E} \cdot \mathbf{J} < 0$. In this dynamo region with $\mathbf{E} \cdot \mathbf{J} < 0$, the particle energy is converted to magnetic energy.

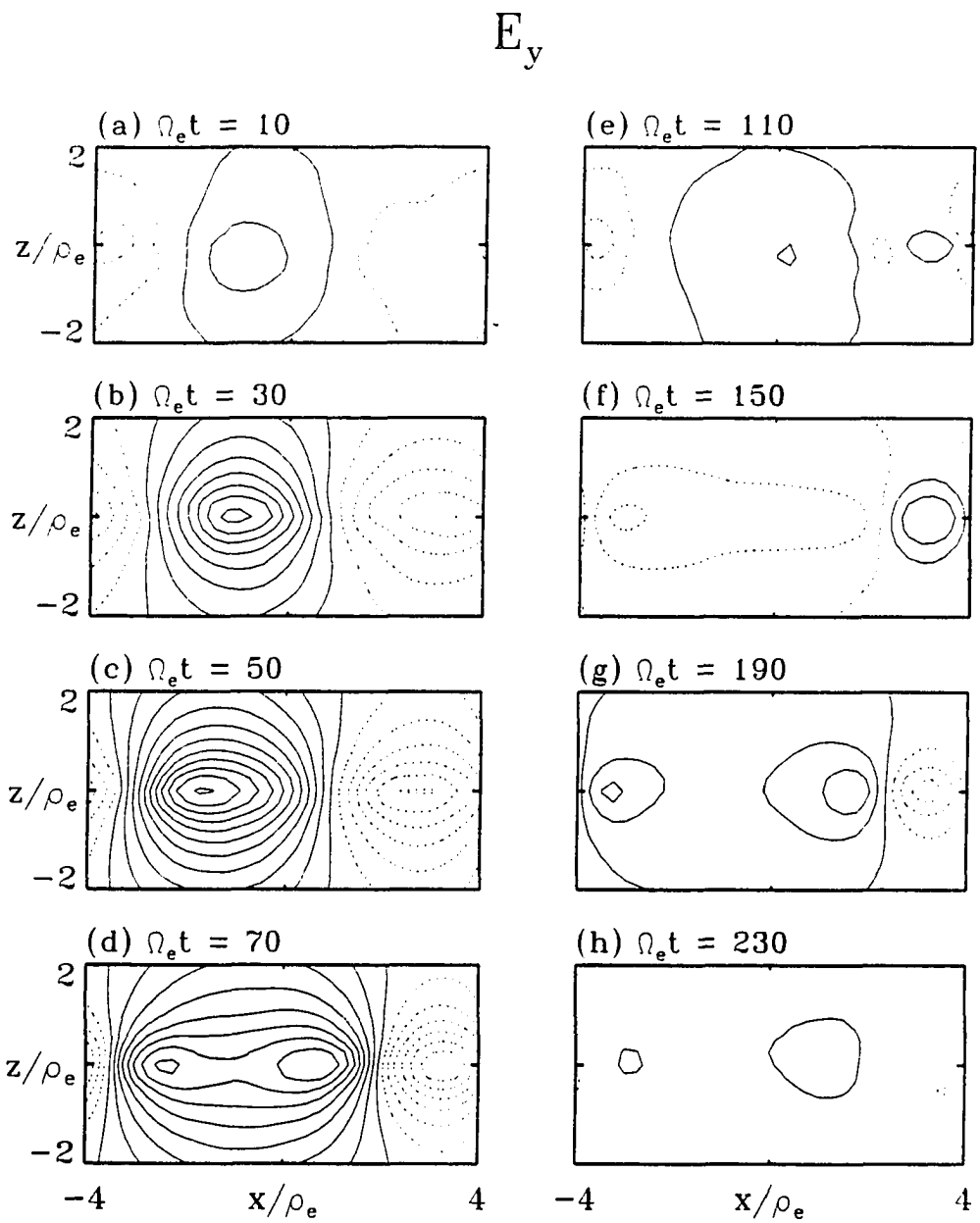

Figure 5.2 Contours of the reconnection electric field E_y in the $x - z$ plane for the case shown in Figure 5.1. The increment of E_y between two neighboring contour lines is 0.0025 E_0, where $E_0 = B_0 v_{the}$.

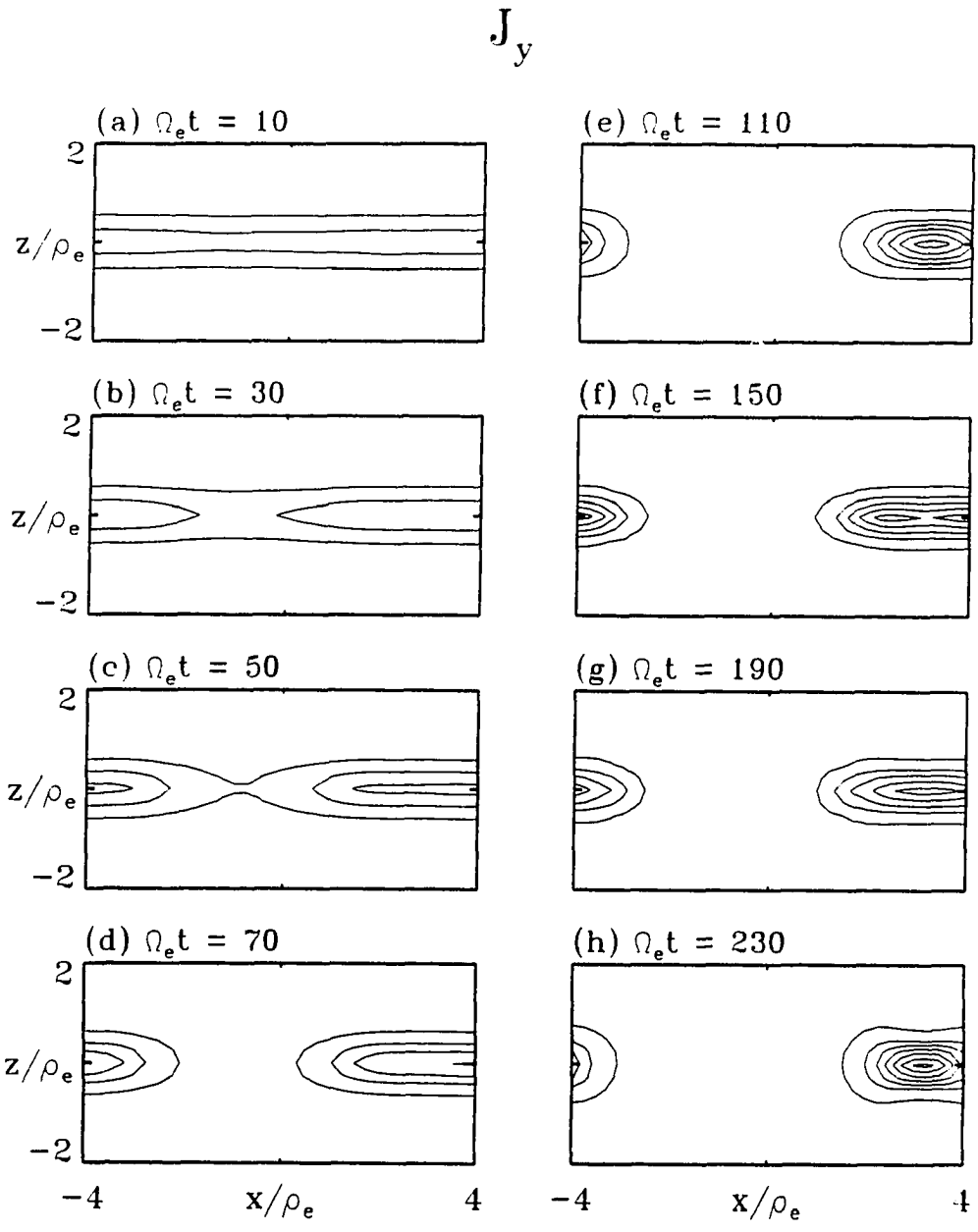

Figure 5.3 Contours of the current density J_y in the $x - z$ plane. The increment of J_y between two neighboring contours is $2J_0$, where $J_0 = N_c e v_{the}$. The outermost contour lines in each plot correspond to J_0.

In the region very close to the O line, $\mathbf{B} \simeq 0$, the term $\partial/\partial t(B^2/2\mu_0)$ is negligible and hence $\nabla \cdot \mathbf{S} \simeq -\mathbf{E} \cdot \mathbf{J} > 0$. The positive divergence of $\mathbf{S}$ indicates that the magnetic flux is emerging outward from the O line. In our opinion, the divergence of the Poynting flux is associated with the plasma reaction to the strong compression near O line. The dynamo process near the O line is not allowed in the resistive MHD model. We will discuss this point in Section 5.3.

5.2 Power-law for time scales

We run two other cases with ion-electron mass ratio $m_i/m_e = 10$ and 100, respectively. The other physical parameters are the same as in the case shown above: $L_x = L_z = 8\rho_e$ and $a = 0.25\rho_e$. The numerical set up is also the same except we run these two cases from $t = 0$ to $t = 120\Omega_e^{-1}$. Figure 5.4 shows the time evolution of the newly generated magnetic flux, the reconnected magnetic flux and the total magnetic flux in the magnetic island. The case with ion-electron mass ratio of 1836 is denoted by the solid lines. The cases with mass ratio of 10 and 100 are denoted, respectively, by dashed and dotted lines.

We obtain the generated flux by calculating the difference between the maximum value of A_y and the initial value of A_y on the x axis, which is equivalent to the time integral of $-E_y$ at the O line. The reconnected magnetic flux is obtained by calculating the difference between the minimum of A_y on the x axis and the initial value of A_y on the x axis, which is the time integral of $+E_y$ at the X line. The total trapped magnetic flux in the magnetic island is then the sum of the generated magnetic flux and reconnected magnetic flux. It is seen from Figure 5.4 that the newly generated magnetic flux can reach a value of $\sim B_0\rho_e$. The generated flux, the reconnected flux and the

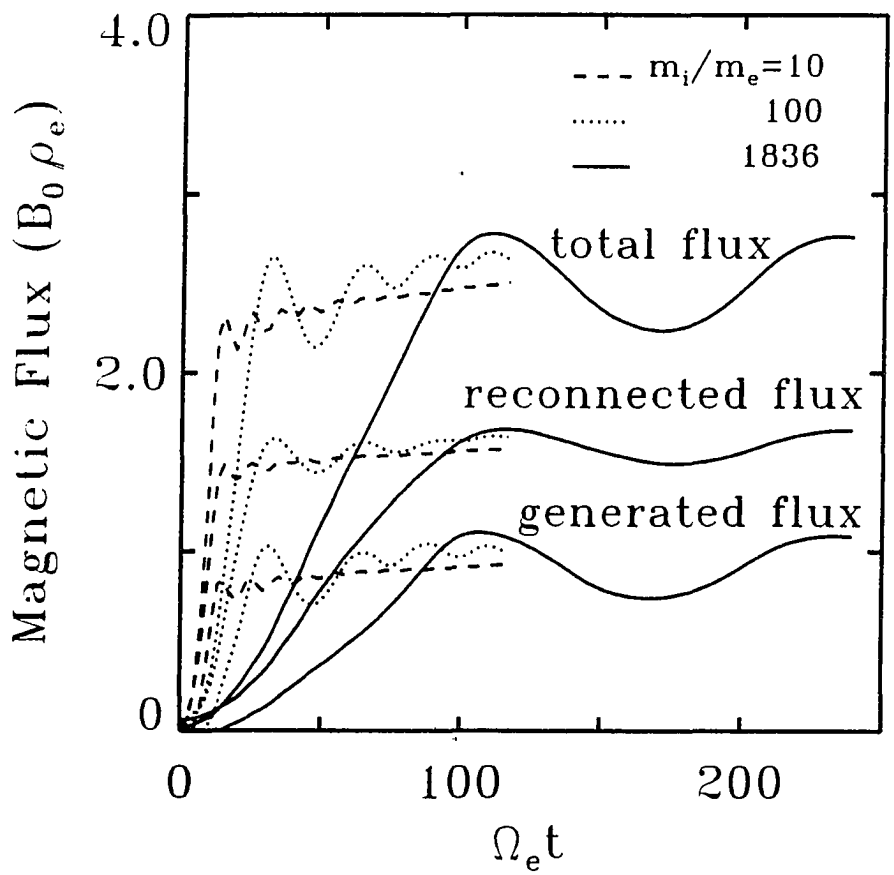

Figure 5.4 The evolution of the newly generated magnetic flux, the reconnected magnetic flux and the total magnetic flux in the magnetic island for the cases with ion-electron mass ratio $m_i/m_e = 10$, 100 and 1836, respectively.

total trapped flux grow rapidly to reach their first maxima and then oscillate. A slow secular growth is superposed on the oscillations. The cases with different mass ratio are qualitatively the same except that the case with a smaller mass ratio has a shorter evolution time scale.

We have simulated several cases by reducing L_x to $4\rho_e$ or enlarging L_x to $32\rho_e$. The generation of new magnetic flux is also observed during the formation of O lines in these cases. In the case with $L_x = 32\rho_e$, two magnetic islands are formed.

Plotted in Figure 5.5 are the various time scales as a function of the ion-electron mass ratio: (a) T_{max} is the time when the total magnetic flux reaches its first maximum; and (b) T_{osc} is the period of the first oscillation of the total flux corresponding to the time from its first maximum to the second maximum. In Figure 5.5, diamonds are used to denote T_{max} and the solid line is their linear regression. It is found that the slope of the solid line is 0.37, which means $T_{max}\Omega_e \propto (m_i/m_e)^{0.37}$. Crosses and the dotted line are for T_{osc}, and $T_{osc}\Omega_e \propto (m_i/m_e)^{0.48}$. The dependence of the time scales on the mass ratio indicates that the interaction between electrons and ions is very important in the reconnection process.

The mass ratio dependence shows that the process has a hybrid time scale even though the system size is of electron gyroradius scale. The power-law of the ion-electron mass ratio may be very useful in future particle simulation studies. For a system with a size larger than the ion gyroradius, particle simulation with a large mass ratio requires a large amount of computer time. In that case, we can simulate the system with small mass ratios, find the power index, and then rescale the results to the system with a realistic mass ratio.

Note that the oscillatory behavior is observed in the previous full particle simulation [Hewett et al., 1988], one-species particle simulation [Cai et al., 1994; and the result

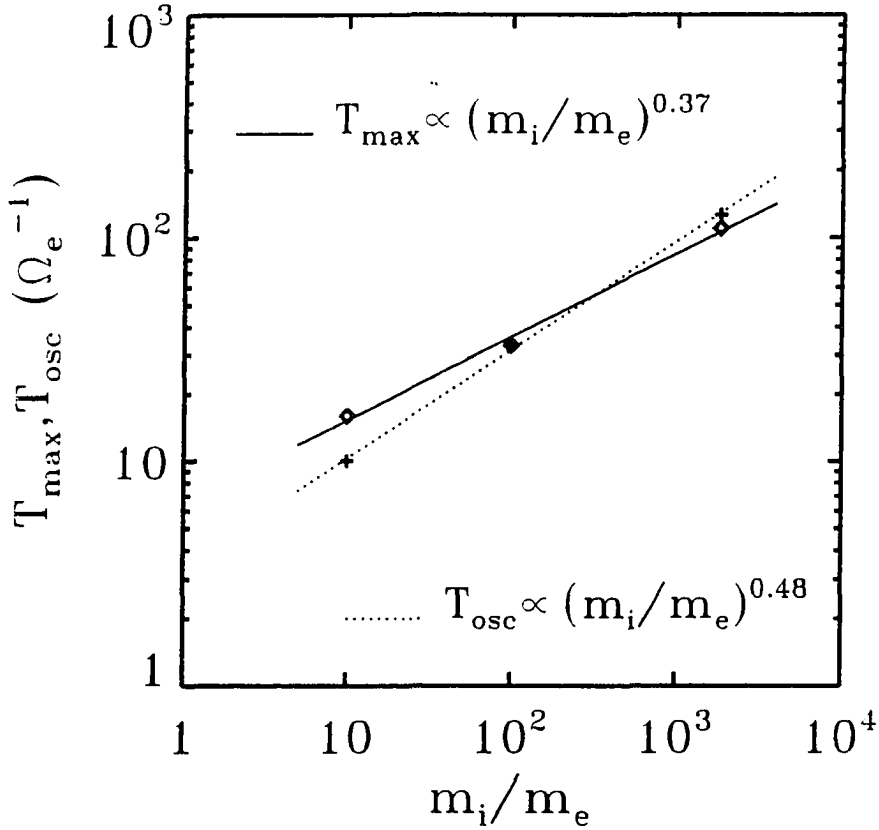

Figure 5.5 The ion-electron mass ratio dependence of (a) T_{max}, the time when the total magnetic flux reaches its first maximum, and (b) T_{osc}, the period of the first oscillation of the total flux.

presented in Chapter 2] and laboratory experiment [Yamada et al., 1991]. It appears that the overcompressed plasma near the O line in the early stage of reconnection causes the later damped oscillations. Hewett et al. [1988] emphasized that the oscillatory behavior does not exist in cases with a small ion-to-electron mass ratio (< 200) in which ions, pulled by an ambipolar electric field, can follow electron flow before the electron flow reverses. However, the oscillatory behavior is also observed in our simulations with a small mass ratio as shown in Figure 5.4 and in our one-species particle simulation presented in Chapter 2, in which electrons are considered as a neutralized background. A large reconnection rate may smear out the oscillations in the cases with $m_i/m_e < 200$ in Hewett et al. [1988] and in the cases with a counter-helicity in Yamada et al. [1991].

5.3 Discussion and summary

In the resistive MHD model, the Ohm's law is written as $\mathbf{E} + \mathbf{v} \times \mathbf{B} = \eta \mathbf{J}$. Near the O line, the Lorentz force $\mathbf{v} \times \mathbf{B}$ nearly vanishes, and the electric field $\mathbf{E}$ and $\mathbf{J}$ are in the same direction. The dynamo process, which requires $\mathbf{E} \cdot \mathbf{J} < 0$, is not allowed in the region near the O line.

However, it is not surprising to observe a dynamo process with $\mathbf{E} \cdot \mathbf{J} < 0$ near the O line in a collisionless plasma. As has been shown in the last chapter, the presence of the inertia term and the pressure tensor terms makes it possible to have $\mathbf{E} \cdot \mathbf{J} < 0$ along the O line or X line.

In a strictly two-dimensional system, the conservation of canonical momentum in the y-direction, $P_y = m_e v_y - eA_y$, however, will impose a limit of the generation of the magnetic flux near an O line, $\Delta A \sim m_e v_y/e \simeq B_0 \rho_e$, which is consistent with the result shown in Figure 5.4.

However, if electrons can be supplied from the third dimension and hence the electrons play a role as a neutralized background, the reconnection process is mainly determined by the ion dynamics. Therefore, the newly generated magnetic flux can be as large as $B_0\rho_i$, where ρ_i is the ion gyroradius. We have carried out simulations with only the ion species and found the generated flux near O line is indeed $\sim B_0\rho_i$.

In summary, we found a new dynamo process for magnetic reconnection in a current sheet with electron gyroradius scale. The main results are:

(1) a new magnetic flux of the order $\sim B_0\rho_e$ is generated near the magnetic O line.

(2) This process is associated with the compression of particles during magnetic reconnection.

(3) The presence of the inertia term $m_e\partial v_y^{(e)}/\partial t$ and the off-diagonal pressure terms make the dynamo process possible, in which $\mathbf{E}\cdot\mathbf{J} < 0$ along the O line. In classical MHD models, $\mathbf{E}\cdot\mathbf{J} < 0$ is not allowed in the region near the O line.

(4) The characteristic time to reach maximum flux in the magnetic island has a power-law dependence on the ion-electron mass ratio, $T_{max} \propto (m_i/m_e)^{0.37}\Omega_e^{-1}$.

CHAPTER 6

Summary and future studies

In this chapter, we first comment on the usefulness of particle simulation in the study of space plasmas. The main results of the present study are then presented. Possible topics for future studies in collisionless reconnection are suggested.

6.1 Importance of particle simulation in magnetic reconnection

In the magnetohydrodynamic (MHD) model, the governing equations are related to the basic conservation laws. MHD model is powerful in describing large scale phenomena. However, the coupling between different regions in space environments is critically dependent on the micro-processes that take place in their interfaces. The interfaces usually can be described as MHD shocks or discontinuities. The application of the same conservation laws leads to the Rankine-Hugoniot jump conditions for the shocks and discontinuities. However, the conservation laws in MHD model cannot answer fundamental questions on micro-processes in the interface regions, which include the diffusion region of magnetic reconnection.

One approach to study the micro-physics of critical structures and magnetic reconnection is to employ the set of Maxwell-Vlasov equations. The application of Maxwell-Vlasov equations to linearized problems has been very successful. However, it is very tedious to solve the Maxwell-Vlasov equations in general cases. Even for one-dimensional problems, there are three additional dimensions in velocity space.

On the other hand, particle simulation provides a powerful tool to study the micro-physics in collisionless plasmas. Particle simulations have been successful in the study of the structure and heating mechanisms of fast shocks [e.g., Leroy et al., 1982; Lee et al., 1988], rotational discontinuities [e.g., Swift and Lee, 1983] and slow shocks [e.g., Swift, 1983; Lin and Lee, 1991, 1994].

The evolution of shocks or discontinuities is basically a one-dimensional problem in real space and electrons can be treated as a fluid. However, magnetic reconnection is a two-dimensional problem and electrons cannot be treated as a fluid because the breakdown of frozen-in condition involves mainly the electron dynamics. Through particle simulations, we find in this thesis (1) the importance of both electron and ion presure tensor terms in the generalized Ohm's law, and (2) a new dynamo process which is not allowed in resistive magnetofluids.

6.2 Main results in this thesis

In this thesis, we use particle simulation to examine the generalized Ohm's law near neutral lines in collisionless magnetic reconnection. The main results are briefly described below.

6.2.1 Off-diagonal pressure terms and the breakdown of frozen-in condition

In a particle simulation with one active species, it is found that a weakly anisotropic and skewed velocity distribution is formed near the magnetic X line, leading to the presence of off-diagonal elements of plasma pressure tensor. The gradients of the off-diagonal pressure terms transport plasma momentum away from the X line to balance the reconnection electric field, leading to the breakdown of the frozen-in condition.

In a full particle simulation in which both ions and electrons are treated as particles, the electron off-diagonal pressure terms play a dominant role in balancing the electric field E_y for electrons at both the magnetic X line and O line. The deceleration or acceleration of ion bulk velocities in the direction of reconnection electric field (E_y) results mainly from the momentum transport due to the off-diagonal elements of ion pressure tensor; the reconnection electric field plays an insignificant role in the force balance for ions. Both the ion and electron off-diagonal pressure terms can be dominant terms in the generalized Ohm's law near neutral lines. The neglect of ion pressure terms in the conventional generalized Ohm's law (1.7) cannot be justified for cases with $T_i/T_e > 1$.

In a calculation based on a linear kinetic theory, we also found that the electron Landau resonance in the linear tearing instability can also be described in terms of the off-diagonal electron pressure tensor term $P_{xy}^{(e)}$.

6.2.2 Origin of the off-diagonal pressure terms

The generation of the off-diagonal pressure terms is associated with the thermal dispersion of particle motions and the response of particle distribution function in the electric and magnetic fields near the neutral lines. The acceleration of particles due to E_y and the rotation of velocity due to B_z reinforce each other in the generation of P_{xy}. On the other hand, the rotation due to B_x tends to reduce the skewing of distribution function in the $v_y - v_z$ space generated by the acceleration due to E_y. Therefore, P_{zy} is usually smaller than P_{xy}.

6.2.3 The spatial scaling for P_{xy}

The scale length of P_{xy} is determined from our simulation data and the result is compared with the Dungey scale length, $L_D = (m_i E_y / e\beta^2)^{1/3}$. For the case with one active species, the scale length L_{Pxy} of the off-diagonal pressure term P_{xy} is found to be $L_{Pxy} \simeq 1.8 L_D$. In a full particle simulation, the scale length L_{Pxy} for the electron pressure tensor term $P_{xy}^{(e)}$ is found to be $L_{Pxy} \simeq 4.4 L_D = 4.4(m_e E_y / e\beta^2)^{1/3}$.

6.2.4 A new dynamo process

A dynamo process is found to operate near the magnetic O line, leading to the generation of new magnetic flux. The generation of new flux is associated with plasma compression in the magnetic island. The generated new flux is estimated to be $\sim B_0 \rho_e$ for simulations with an initial current sheet of electron gyroradius scale. This dynamo process cannot exist in a resistive magnetofluid. The plasma inertia and momentum transport due to the off-diagonal elements of plasma pressure tensor can lead to $\mathbf{E} \cdot \mathbf{J} < 0$ near the magnetic O-line, which makes the dynamo process possible.

6.3 Future Studies

Possible topics for future studies are listed below. They include (a) the effect of an initial guide field, (b) magnetic reconnection in a thick current sheet, and (c) the existence of steady-state reconnection in a collisionless plasma.

6.3.1 Inclusion of an initial guide magnetic field

In the dayside magnetopause, usually there exists a finite guide magnetic field ($B_y \neq 0$). In order to address the magnetic reconnection in the dayside magnetopause, it is necessary to extend particle simulation by including an initial guide component of magnetic field. In the presence of a finite B_y, the electrons or ions are magnetized (in the traditional sense) in the diffusion region. Therefore, the origin of the off-diagonal pressure terms is different from that in the $B_y = 0$ case [Dungey, 1988; Cai et al., 1994]. It is worthwhile to study the generation of off-diagonal pressure terms in the presence of a finite B_y by using particle trajectory calculations and particle simulations. A preliminary particle simulation result indicates that plasma pressure is weakly non-gyrotropic, and hence the off-diagonal pressure terms play an important role in balancing reconnection electric field even if a strong guiding component is applied.

6.3.2 Magnetic reconnection in a current sheet with ion length scale

In full particle simulations presented in this thesis, the initial current sheet thickness is on the order of electron gyroradius. In real system, for example, in the dayside magnetopause, however, the current sheet thickness is on the order of ion gyroradius. It is unlikely to simulate a real system by using a real ion-electron mass ratio. The power-law dependence of the ion-electron mass ratio may be very useful in future particle simulation studies. For a system with a size of ion gyroradius, particle simulation with a large mass ratio requires a large amount of computer time. In that case, we can simulate the system with small mass ratios, find the power index, and then rescale the results to the system with a realistic mass ratio.

In addition, the ion-electron mass ratio scaling can also be used as a measure of the interaction between ions and electrons in collisionless plasmas. The mass-ratio dependence presented in Chapter 5 shows that the process has a hybrid time scale even though the system size is of electron gyroradius scale. This indicates that the interaction between electrons and ions plays a very important role in the reconnection process.

6.3.3 Steady-state magnetic reconnection

Most steady-state magnetic reconnection models are constructed in the framework of MHD formulation. MHD simulations indicate that a different resistivity model would result in a different type of reconnection. For example, in a simulation with locally enhanced resistivity, one can obtain a Petschek steady-state reconnection model [Yan et al., 1993]. However, in a simulation with a uniform resistivity, the Petschek fast reconnection evolves first to the Sweet-Parker reconnection, and then a time-dependent multiple X line reconnection [Lee and Fu, 1986; Yan et al., 1993].

It is very important to examine whether a steady-state magnetic reconnection can exist in collisionless plasmas. Magnetic reconnection in a collisionless plasma is different from that in a resistive magnetofluid at least in the following aspects.

(1) There are an ion diffusion region and an electron diffusion region in a collisionless plasma with the latter being embedded in the former. In the ion diffusion region, the electrostatic interaction may play a very important role. Our simulation result shown in Chapter 3 indicates that the electrostatic field can be two orders larger than the reconnection electric field. The generated B_y component may also be important in the ion diffusion region.

(2) In a resistive magnetofluid, the reconnection electric field is directly related to the current density in the diffusion region, $\mathbf{E} \simeq \eta \mathbf{J}$. In a collisionless plasma, however, the current density is not directly related to the reconnection electric field (see equation (1.12)) in the electron diffusion region. This difference is highlighted in the result presented in this thesis that $\mathbf{E} \cdot \mathbf{J}$ can be negative at neutral lines in collisionless reconnection.

6.4 Conclusion

Magnetic reconnection in space environments cannot be adequately described by the resistive MHD formulation. Particle simulations provide a powerful tool in examining the micro-processes in collisionless magnetic reconnection. The off-diagonal pressure tensor terms are found to be responsible for the breakdown of frozen-in condition in collisionless reconnection. In addition, a new dynamo process is found to operate in the magnetic O line region, leading to the generation of new magnetic flux.

REFERENCES

Allen, C., and D. W. Swift, A particle simulation of the tearing mode instability at the dayside magnetopause, *J. Geophys. Res., 94*, 6925, 1989.

Ambrosiano, J. J., L. C. Lee, and D. W. Swift, Simulation of ion tearing instability in the presence of a background plasma, *J. Geophys. Res., 88*, 7860, 1983.

Axford, W. I., Magnetic field reconnection, in *Magnetic reconnection in Space and Laboratory Plasmas*, ed. by E. W. Hones, Jr., p. 1, Geophysical Monograph 30, AGU, Washington, D.C., 1984.

Birdsall, C. K., and A. B. Langdon, *Plasma Physics via Computer Simulation*, MacGraw-Hill, New York, 1985.

Burkhart, G. R., J. F. Drake, and J. Chen, Structure of the dissipation region during magnetic reconnection in collisionless plasma, *J. Geophys. Res., 96*, 11,539, 1991.

Cai, H. J., and L. C. Lee, The role of off-diagonal elements of pressure tensor in collisionless magnetic reconnections, in *Physics of Space Plasmas (1993), SPI Conference Proceedings and Reprient Series*, Number 13, T. Chang, G. B. Crew and J. P. Jasperse, eds., Scientific Publishers Inc., Chambridge, Mass., 1994.

Cai, H. J., and L. C. Lee, Magnetic flux generation near an O-line in collisionless reconnection -- A new dynamo process, *Physics of Plasmas, 2(10)*, 3852, 1995.

Cai, H. J., D. Q. Ding, and L. C. Lee, Momentum Transport Near a Magnetic X Line in a Collisionless Reconnection, *J. Geophys. Res., 99*, 35, 1994.

Coroniti, F. V., and A. Eviatar, Magnetic field reconnection in collisionless plasma, *Astrophys. J., Suppl. Ser., 33*, 189, 1977.

de la Beaujardiere, O., L. R. Lyons, and E. Friis-Christensen, Sondrestrom radar measurements of the reconnection electric field, *J. Geophys. Res., 96*, 13,907, 1991.

Ding, D. Q., L. C. Lee, and Z. F. Fu, Multiple X line reconnection, 3, A particle simulation of flux transfer events, *J. Geophys. Res., 91*, 13,384, 1986.

Ding, D. Q., L. C. Lee, and D. W. Swift, Particle simulations of driven collisionless magnetic reconnection at the dayside magnetopause, *J. Geophys. Res., 97*, 8453, 1992.

Drake, J. F., and Y. C. Lee, Kinetic theory of tearing instabilities, *Phys. Fluids, 20,* 1341, 1977.

Dungey, J. W., Interplanetary magnetic field and the auroral zones, *Phys. Rev. Lett., 6,* 47, 1961.

Dungey, J. W., Noise-free neutral sheet, in Proceedings of an International Workshop in Space Plasma, vol. II, *Eur. Space Agency Spec. Publ., ESA SP-285,* 15, 1988.

Furth, H. P., J. Killeen, and M. N. Rosenbluth, Finite-resistivity instabilities of a sheet pinch, *Phys. Fluids, 6,* 459, 1963.

Galeev, A. A., Spontaneous reconnection of magnetic field lines in a collisionless plasma, in *Basic Plasma Physics,* edited. by A. A. Galeev and R. N. Sudan, p. 305, Elsevier Scientific, New York, 1984.

Giovanelli, R. G., Mangetic and electric phenomena in the Sun's atmosphere associated with sunspots, *Mon. Not. Roy. Ast. Soc., 107,* 338, 1947.

Hewett, D. W., G. E. Francis, and C. E. Max, New regimes of magnetic reconnection in collisionless plasmas, *Phys. Rev. Lett., 61,* 893, 1988.

Horton, W., and T. Tajima, Decay of correlations and the collisionless conductivity in the geomagnetic tail, *Geophys. Res. Lett., 17,* 123, 1990.

Huba, J. D., J. F. Drake, and N. T. Gladd, Lower hybrid drift instability in field reserved plasmas, *Phys. Fluids, 23,* 552, 1980.

Krall, N. A., and A. W. Trivelpiece, *Principles of Plasma Physics,* McGraw-Hill, New York, p. 88, 1973.

Lee, L. C., Ion two-stream and modified two-stream instabilities in the magnetic neutral sheet, *Geophys. Res. Lett., 9,* 1159, 1982.

Lee, L. C., The magnetopause: A tutorial review, in *SPI Conference Proceedings and Reprint Series,* vol. 10, edited by T. Chang, G. B. Crew, and J. P. Jasperse, Scientific, New York, 1990.

Lee, L. C., A review of magnetic reconnection: MHD models, *Physics of the Magnetopause,* Geophysical Monograph 90, 139, 1995.

Lee, L. C., and D. Q. Ding, Magnetic reconnection in a collisionless plasma: Evidence for the current sheet acceleration, *Geophys. Res. Lett., 14*, 1003, 1987.

Lee, L. C., and Z. F. Fu, Multiple X line reconnection, 1. A criterion for the transition from a single X line to a multiple X line reconnection, *J. Geophys. Res., 91*, 6807, 1986.

Lee, L. C., C. P. Price, and C. S. Wu, A study of mirror waves generated downstream of a quasi-perpendicular shock, *J. Geophys. Res., 93*, 247, 1988.

Leroy, M. M., D. Winske, C. C. Goodrich, C. S. Wu, and K. Papadopoulos, The structure of perpendicular bow shock, *J. Geophys. Res., 87*, 5081, 1982.

Lin, Y., and L. C. Lee, Chaos and ion heating in a slow shock, *Geophys. Res. Lett., 18*, 1615, 1991.

Lin, Y., and L. C. Lee, Structure of reconnection layers in the magnetosphere, *Space Science Reviews, 65*, 59, 1994.

Lyons, L. R., and D. C. Pridmore-Brown, Force balance near an X line in a collisionless plasma, *J. Geophys. Res., 95*, 20,903, 1990.

Lyons, L. R., and D. C. Pridmore-Brown, Force balance near an X line along which $\mathbf{E} \cdot \mathbf{J} < 0$, *J. Geophys. Res., 97*, 2955, 1992.

Lyons, L. R., M. Schulz, and J. F. Fennell, Trapped-particle evacuation: Source of magnetotail bursts and tailward flows? *Geophys. Res. Lett., 16*, 353, 1989.

Mandt, M. E., R. E. Denton and J. F. Drake, Transition to whistler mediated magnetic reconnection, *Geophys. Res. Lett., 21*, 73, 1994.

Martin, R. F., Jr., Chaotic particle dynamics near a two-dimensional magnetic neutral point with application to the geomagnetic tail, *J. Geophys. Res., 91*, 11,985, 1986.

Parker, E. N., Sweet's mechanism for merging magnetic fields in conducting fluids, *J. Geophys. Res., 62*, 509, 1957.

Petschek, H. G. Magnetic Annihilation, in *AAS-NASA Symposium on the Physics of Solar Flares*, ed. by W. N. Hess, p. 425, NASA Spec. Publ. SP-50, 1964.

Priest, E. R., and T. G. Forbes, New models for fast steady state magnetic reconnection, *J. Geophys. Res., 91*, 5579, 1986.

Priest, E. R., and L. C. Lee, Nonlinear magnetic reconnection models with separatrix jets, *J. Plasma Phys., 44*, 337, 1991.

Pritchett, P. L., F. V. Coroniti, R. Pellat, and H. Karimabadi, Collisionless reconnection in two-dimensional magnetotail equilibria, *J. Geophys. Res., 96*, 11,523, 1991.

Rossi, B., and S. Olbert, *Introduction to the Physics of Space*, MacGraw-Hill, New York, 1970.

Siscoe, G. L., Solar system magnetohydrodynamics, in *Solar-Terrestrial Physics, Principles and Theoretical Foundations*, edited by R. L. Carovillano and J. M. Forbes, p. 11, D. Reidel Publishing Company, 1983.

Sonnerup, B. U. O., Magnetic reconnection in a highly conducting incompressible fluid, *J. Plasma Phys., 4*, 161, 1970.

Sonnerup, B. U. O., Magnetic field reconnection, in *Solar System Plasma Physics*, vol. 3, edited by L. T. Lanzerotti, C. F. Kennel, and E. N. Parker, p. 45, North-Holland, New York, 1979.

Sonnerup, B. U. O., On the theory of steady state reconnection, *Comput. Phys. Commun., 49*, 143, 1988.

Stern, D. P., The motion of magnetic field lines, *Space Sci. Rev., 6*, 147, 1966.

Speiser, T. W., Particle trajectories in model current sheets, 1, analytical solutions, *J. Geophys. Res., 70*, 4219, 1965.

Speiser, T. W., Conductivity without collisions or noise, *Planet. Space Sci., 18*, 613, 1970.

Sweet, P. A., The neutral point theory of solar flares, in *Electromagnetic Phenomena in Cosmical Physics*, ed. by B. Lehnert, p. 123, Cambridge University Press, London, 1958.

Swift, D. W., On the structure of the magnetic slow switch-off shock, *J. Geophys. Res., 881*, 5685, 1983.

Swift, D. W., Numerical simulations of tearing mode instabilities, *J. Geophys. Res., 91*, 219, 1986.

Swift, D. W., and L. C. Lee, Rotational discontinuities and the structure of the magnetopause, *J. Geophys. Res., 88*, 111, 1983.

Terasawa, T., Numerical study of explosive tearing mode instability in one-component plasmas, *J. Geophys. Res., 86*, 9007, 1981.

Vasyliunas, V. M., Theoretical models of magnetic field line merging, 1, *Rev. Geophys., 13*, 303, 1975.

Hesse, M, and D. Winske, Hybrid simulation of collisionless ion tearing, *Geophys. Res. Lett., 20*, 1207, 1993.

Yamada, M., F. W. Perkins, A. K. MacAulay, Y. Ono, and M. Katsurai, Initial results from investigation of three-dimensional magnetic reconnection in a laboratory plasma, *Phys. Fluids B 3*, 2379, 1991.

Yan, M., L. C. Lee, and E. R. Priest, Magnetic reconnection with large separatrix angles, *J. Geophys. Res., 98*, 7593, 1993.

Yeh, T., and W. I. Axford, On the reconnection of magnetic field lines in conducting fluids, *J. Plasma Phys., 4*, 207, 1970.